NANOPARTICULATE FUEL ADDITIVES AND

COMBUSTION CATALYSTS

by

Brian Roy Van Devener

A dissertation submitted to the faculty of
The University of Utah
in partial fulfillment of the requirements for the degree of

Doctor of Philosophy

Department of Chemistry

The University of Utah

May 2010

UMI Number: 3401918

UMI®

Dissertation Publishing

ProQuest®

THE UNIVERSITY OF UTAH GRADUATE SCHOOL

SUPERVISORY COMMITTEE APPROVAL
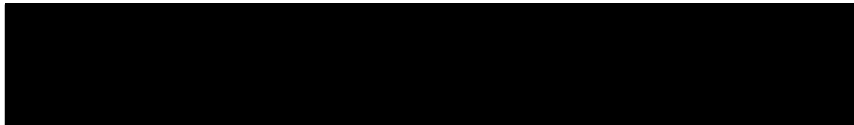
of a dissertation submitted by

Brian R. Van Devener

This dissertation has been read by each member of the following supervisory committee
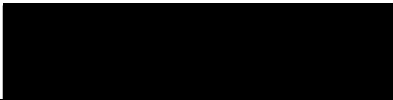and by majority vote has been found to be satisfactory.

7/1/2009

Chair: Scott L. Anderson

7/1/2008

Michael H. Bartl

7/1/2009

Charles A. Wight

7/1/2009

Jennifer S. Shumaker-Parry

7/1/2009
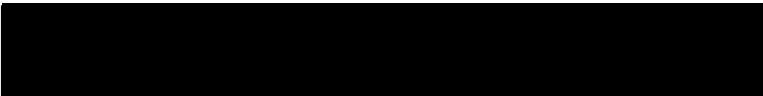
Eric G. Eddings

THE UNIVERSITY OF UTAH GRADUATE SCHOOL

FINAL READING APPROVAL

To the Graduate Council of the University of Utah:

I have read the dissertation of _____Brian Roy Van Devener_____ in its final form and have found that (1) its format, citations, and bibliographic style are consistent and acceptable; (2) its illustrative materials including figures, tables, and charts are in place; and (3) the final manuscript is satisfactory to the supervisory committee and is ready for submission to The Graduate School.

_____8/18/09_____
Date

Scott L. Anderson
Chair: Supervisory Committee

Approved for the Major Department

Henry S. White
Chair/Dean

Approved for the Graduate Council

Charles A. Wight
Dean of The Graduate School

ABSTRACT

JP-10 is a synthetic fuel with high volumetric energy content. One problem with JP-10, is that its combustion kinetics can be too slow for efficient combustion in hypersonic flight applications. Chapter 2 presents a study on the thermal breakdown and catalytic combustion of JP-10 fuel using CeO_2 (ceria) nanoparticles, in a flow tube reactor. In-situ mass spectrometry was used to analyze decomposition products. In the absence of O_2, CeO_2 efficiently oxidizes JP-10, reducing decomposition onset temperatures by 300 K over that in a clean flow tube. Under conditions with O_2 and CeO_2 present, oxidation of JP-10 was found to be catalytic; i.e., oxidation is initiated by reaction of JP-10 with CeO_2, which is then reoxidized by O_2.

Boron is of interest as a high energy density fuel as it has one of the highest volumetric heats of combustion known. A major difficulty in getting boron to burn efficiently is that boron surfaces are protected by a native oxide layer. Chapter 3 presents a simple, scalable, one-step, one-pot synthesis method for producing ~50 nm boron nanoparticles that are largely unoxidized, made soluble in hydrocarbons through oleic acid functionalization, and optionally coated with ceria. Scanning electron microscopy (SEM) and dynamic light scattering (DLS) were used to investigate size distributions, with X-ray photoelectron spectroscopy (XPS) to probe the surface chemistry.

Cryogenic methane has been proposed as a fuel for use in hypersonic engines, due to its relatively high energy content; however its poor ignition performance needs to be addressed through use of catalysts. Chapters 4 and 5 investigate the composition, structure, and surface chemistry of several types of Pd/PdO based nano-catalysts designed to be fuel soluble. A combination of high resolution transmission electron microscopy (HRTEM), electron diffraction, scanning transmission electron microscopy/energy dispersive x-ray spectroscopy (STEM/EDX), and XPS were used. In-situ generated particles were found to be primarily crystalline, metallic Pd, in a narrow size distribution around 8 nm. The ignition temperature was lowered ~150 K by the catalyst, and evidence is presented showing that ignition is correlated with formation of a subnanometer oxidized Pd surface layer at higher temperatures.

TABLE OF CONTENTS

ACKNOWLEDGMENTS

CHAPTER 1

INTRODUCTION

A major hurdle in finding ways to improve the performance of supersonic propulsion systems is obtaining a fuel with the necessary characteristics. Typically, fuels used in these applications must have very high energy densities, while simultaneously having very fast ignition and combustion kinetics. As an example, one particular type of supersonic engine, the pulse detonation engine, requires a very large spark to ignite the air fuel mixture that is not practical for most engine designs. JP-10 (exo-tetrahydrodicyclopentadiene, $C_{10}H_{16}$) is commonly referred to as a candidate fuel as it has very attractive energetic properties (its heat of combustion is 39.4 MJ/L), and has been studied fairly extensively since it is a single molecule rather than a distillate of several different hydrocarbons.[1-13] However, as with most fuels, it is difficult to initiate efficient combustion of JP-10 under the conditions typical of many hypersonic engines. One solution to this problem is the use of catalysts to enhance the combustion. In combustion applications, fixed bed catalysts are commonly used to increase low temperature combustion efficiency and consequently reduce harmful emission products such as NO_x. Such an approach is impossible for aircraft applications due to the high gas flow velocity, short contact time between the fuel molecules and the active material, as well as limitations on size and weight.

One way around the abovementioned issue is to introduce the catalyst directly into the combustor with the fuel/air mixture.[14,15] Several key criteria must be met for such an idea to be feasible. First, the catalyst must have a large surface area to maximize the number of active sites available to the fuel molecules. Second, if it is to be introduced directly into the fuel, the catalyst must be highly soluble to prevent settling and clogged fuel lines. In addition, for most applications it must be relatively

inexpensive as it will be passed through the exhaust during the combustion cycle. Finally, the catalyst must be highly active towards enhancing combustion rates in order to minimize the amount of loading required. Most catalysts would simply be dead weight to the fuel from an energy point of view, thus heavy loadings may offset any gains achieved through catalytic enhancement.

Nanoparticulate catalysts offer a promising solution to these difficulties. With large surface area to volume ratios, they offer many active sites for catalysis. Furthermore, if their surfaces could be functionalized with appropriate ligands they could be made soluble in hydrocarbon fuels. One might also envision tailor-made nano-structures that consist of a core of energy dense material, surrounded by a layer containing a catalyst. Such dual purpose structures could accelerate fuel combustion without degrading, and possibly enhancing the overall energy content of the fuel.

This study investigates nanoparticulate fuel additives and combustion catlalysts from three primary perspectives, which will be discussed below.

The viability of using nanoparticulate catalysts to enhance the combustion of fuels is investigated in Chapter 2. The thermal breakdown and catalytic oxidation of JP-10 in the presence of CeO_2 (ceria) and Fe_2O_3 nanoparticles was studied by using a mass spectrometer to analyze the breakdown products from a flow tube reactor. Ceria seemed a good first choice as it is inexpensive, and has many applications as a catalyst, including diesel pollution remediation.[16-18] In the hopes of finding an even less expensive additive, Fe_2O_3 nanoparticles were also tested for activity.

This work represented the first demonstration of ceria mediated JP-10 catalysis. Use of the ceria nanoparticles resulted in a substantial reduction in the initial

decomposition temperature of JP-10, over the noncatalytic case. The initiation of the fuel breakdown was demonstrated to be from CeO_2 oxidation, with O_2 serving mainly to complete the catalytic cycle by re-oxidizing the ceria. Fe_2O_3 was also found to be active towards JP-10 catalysis, but much less so as compared to the ceria. JP-10 was chosen as the fuel in this study due to the relative simplicity of analyzing its mass spectrum as compared to other fuels. However, similar results would be expected with other hydrocarbon fuels.

Chapter 3 presents a simple one-step, one-pot synthesis method for producing boron nanoparticles. These nanoparticles can be optionally functionalized with an oleic acid capping ligand, which renders them fuel soluble and largely unoxidized, and coated with catalytically active ceria.

As energy-dense fuel additives, boron and boron rich solids are unparalleled in that they are the only practical materials with both volumetric (135.8 MJ/liter) and gravimetric (58.5 MJ/kg) energy densities that are substantially greater than hydrocarbon fuels. Due to these attractive properties, many years of research have gone into developing boron or boron based fuels or fuel additives for use in liquid or solid fueled propulsion systems. Despite its great potential as a fuel, boron has not, to date, been widely utilized due to the difficulty in igniting and burning it efficiently.[19] Part of the problem lies in the fact that boron is refractory (T_{vap} = 2800 K), thus its combustion depends on heterogeneous reactions, which tend to be slow and diffusion limited. Several researchers have suggested that by using nanoparticulate boron, the heterogeneous chemistry can possibly be accelerated due to the large surface area to volume ratio.[20-22] Furthermore, boron naturally forms a native oxide layer when

exposed to oxygen; which tends to inhibit combustion. For nano-sized particles, this is an especially important consideration, since for smaller particles any oxide overlayer would comprise a greater share of the particle's mass as compared to larger particles. This oxidized overlayer would lead to reduced energy densities.

The boron nanoparticle production method developed and discussed in this work, is based on high energy ball milling; a procedure which is simple, inexpensive, and readily scalable. For any industrial application, this would offer great advantages over traditional methods to producing boron nanoparticles, such as gas phase pyrolysis of diborane or solution based synthesis methods, which would tend to be costly and time consuming on large scales. The nanoparticles have a narrow size distribution centered around 50 nm, are largely unoxidized when coated with oleic acid, and can be at least partially coated with catalytically active ceria. While there have been previous attempts to produce coated boron particles using materials such as glycidyl azide polymer (GAP),[23,24] these methods resulted in boron particles that were still significantly oxidized.

Our method results in particles that are largely unoxidized, and air stable. By including a catalytically active ceria coating the combustion of the carrier fuel would tend to be accelerated, and the combustion efficiency of the solid particles would also be improved. In addition, this method of soloublizing boron should be easily extendable to other areas outside of fuels chemistry by simply changing the capping ligand.

X-ray photoelectron spectroscopy (XPS) was used to characterize the surface of the particles; including, the interaction of the capping ligand with the boron surfaces, the ceria coating, and the nature of the oxide layer in unfunctionalized particles.

Electron microscopy and dynamic light scattering (DLS) were used to probe the particle size distributions and morphologies.

Chapters 4 and 5 present work on the characterization of several different types of Pd/PdO based, fuel soluble nanocatalysts.

Cryogenic methane is another fuel which has been proposed for use in hypersonic flight applications due to its high density and specific energy content in comparison to hydrogen and jet fuels, and low tendency toward coke formation.[25] Supported palladium is widely used as a catalyst for methane combustion, with the metal being supported in fixed-bed reactors. As was discussed earlier, such an arrangement is not feasible for aircraft applications, prompting the investigation of fuel soluble Pd/PdO based catalysts.

One approach to using fuel soluble nanoparticles is to generate them in situ from fuel soluble organometallic precursors. This method has been used before, for example in work by Nasibulin et al. who demonstrated nanoparticle synthesis using $Cu(acac)_2$ (copper (II) Acetylacetonate) entrained in a N_2/O_2 flow and passed through a flow tube reactor, whereupon the organic ligands were burned off leaving behind a vapor of Cu, which then condensed to form copper oxide nanoparticles.[26]

In Chapter 5, the fate of in situ generated, Pd based nanoparticles after passage through a flow reactor is studied. Palladium-2,2,6,6-tetramethyl-3,5-heptanedione $(Pd(THD)_2)$, is used as a fuel soluble precursor, and introduced into a flow tube reactor as an aerosol. Once inside the reactor, the aerosol droplets evaporate rapidly, releasing the $Pd(THD)_2$ vapor into the flow. $Pd(THD)_2$ is a weakly bound coordination complex, expected to decompose at relatively low temperatures, releasing Pd atoms. As

discussed in Chapter 5, the Pd atoms nucleate to form nanoparticles, initiating catalytic methane ignition at a gas temperature of 600° C. While the Pd rich particles generated in this manner are found to be active towards catalyzing methane combustion, our focus is on characterizing the particles properties in order to correlate them with ignition and reactor conditions. Of primary concern is the oxidation state of the Pd, which has been shown to strongly affect activity for methane combustion.[27-30] High resolution transmission electron microscopy (HRTEM) and scanning transmission electron microscopy/energy dispersive X-ray analysis (STEM/EDX) were used to probe particle sizes, morphologies and compositions with XPS analysis to probe the surfaces. Particles formed in this manner were found to be primarily crystalline metallic Pd with a narrow size distribution around 8 nm in diameter. The catalyst lowered the ignition temperature by ~150 K, and we present evidence that ignition is correlated with the formation of a subnanometer oxidized Pd surface layer at higher temperatures.

1.1   References

(1)   Burdette, G. W. Liquid hydrocarbon air breather fuel. In *U.S.*; (United States Dept. of the Navy, USA). US, 1983; pp 3 pp.

(2)   Antaki, P.; Williams, F. A. *Combust. Flame* **1987**, *67*, 1.

(3)   Cho, S. Y.; Takahashi, F.; Dryer, F. L. *Combust. Sci. Technol.* **1989**, *67*, 37.

(4)   Chung, H. S.; Chen, C. S. H.; Kremer, R. A.; Boulton, J. R.; Burdette, G. W. *Energy Fuels* **1999**, *13*, 641.

(5)   Clausen, L. C.; Li, T. X.; Law, C. K. *J. Propul. Power* **1988**, *4*, 217.

(6)   Guisinger, S. J.; Rippen, M. E. *Prepr. - Am. Chem. Soc., Div. Pet. Chem.* **1989**, *34*, 885.

(7)   Peters, J. E.; Mellor, A. M. *J. Energy* **1982**, *7*, 95.

(8) Smith, N. K.; Good, W. D. *Aiaa J.* **1979**, *17*, 905.

(9) Szekely, G. A., Jr.; Faeth, G. M. *Combust. Flame* **1983**, *49*, 255.

(10) Takahashi, F.; Heilweil, I. J.; Dryer, F. L. *Combust. Sci. Technol.* **1989**, *65*, 151.

(11) Wong, S. C.; Turns, S. R. *Chem. Phys. Processes Combust.* **1988**, 97/1.

(12) Wong, S. C.; Turns, S. R. *Combust. Sci. Technol.* **1989**, *66*, 75.

(13) Wong, S. C.; Lin, A. C. *Combust. Flame* **1992**, *89*, 64.

(14) Holcomb, R. R.; Holcomb, A. R. Composite metal inorganic and organic sols and colloids as combustion improvers for liquid fuels; Demeter Systems LLC, USA USA, 2006; pp 36.

(15) Valentine, J. M.; Sprague, B. N.; Peter-Hoblyn, J. D. Fuel-soluble platinum-cerium-iron catalysts for combustion of diesel fuel and jet fuel USA: USA, 2005; pp 12.

(16) Vincent, M. W.; Richards, P.; Novel-Cattin, F.; Marcelly, B.; Favre, C. *Society of Automotive Engineers, [Special Publication] SP* **2001**, *SP-1582*, 177.

(17) Wakefield, G. Cerium oxide nanoparticles; Oxonica Limited, UK: Great Britain, 2003; pp 14.

(18) Jung, H.; Kittelson, D. B.; Zachariah, M. R. *Combustion and Flame* **2005**, *142*, 276.

(19) Risha, G. A.; Evans, B. J.; Boyer, E.; Kuo, K. K. *Progress in Astronautics and Aeronautics* **2007**, *218*, 413.

(20) Slutsky, V. G.; Tsyganov, S. A.; Severin, E. S.; Polenov, L. A. *Propellants, Explosives, Pyrotechnics* **2005**, *30*, 303.

(21) Risha, G. A.; Boyer, E.; Evans, B.; Kuo, K. K.; Malek, R. *Materials Research Society Symposium Proceedings* **2003**, *800*, 243.

(22) Kuo, K. K.; Risha, G. A.; Evans, B. J.; Boyer, E. "Potential usage of energetic nano-sized powders for combustion and rocket propulsion." Materials Research Society Symposium Proceedings, 2003, The Pennsylvania State University.

(23) Chiu, Y. S.; Shaw, P. W.; Ho, S. Y. Bond analysis of coated boron powder In *Combust. Boron-Based Solid Propellants Solid Fuels*; Kuo, K. K., Ed.; CRC Boca Raton, Fla, 1993; pp 181.

(24) Shyu, I.-M.; Liu, T.-K. *Combustion and Flame* **1995**, *100*, 634.

(25) Lewis, M. J. *Journal of Propulsion and Power* **2001**, *17*, 1214.

(26) Nasibulin, A. G.; Richard, O.; Kauppinen, E. I.; Brown, D. P.; Jokiniemi, J. K.; Altman, I. S. *Aerosol Science and Technology* **2002**, *36*, 899.

(27) Ciuparu, D.; Lyubovsky, M. R.; Altman, E.; Pfefferle, L. D.; Datye, A. *Catalysis Reviews - Science and Engineering* **2002**, *44*, 593.

(28) Farrauto, R. J.; Hobson, M. C.; Kennelly, T.; Waterman, E. M. *Applied Catalysis, A: General* **1992**, *81*, 227.

(29) McCarty, J. G. *Catalysis Today* **1995**, *26*, 283.

(30) Lyubovsky, M.; Pfefferle, L. *Catalysis Today* **1999**, *47*, 29.

CHAPTER 2

BREAKDOWN AND COMBUSTION OF JP-10 FUEL CATALYZED

BY NANOPARTICULATE CeO$_2$ AND Fe$_2$O$_3$

2.1 Overview

Thermal breakdown and oxidation of JP-10 (exo-tetrahydrodicyclopentadiene - $C_{10}H_{16}$) in the presence of nanoparticulate CeO_2 and Fe_2O_3, was studied in a small alumina flow tube reactor on time scales around 1 ms. Decomposition products were analyzed by an in situ mass spectrometer. In the absence of any oxidizer, JP-10 pyrolyzes at temperatures above ~900 K to a variety of hydrocarbon products. In the absence of O_2, both CeO_2 and Fe_2O_3 oxidize JP-10 efficiently, with decomposition onset temperatures up to 300 K lower than in a clean alumina flow tube under identical flow conditions and substantial conversion to products such as water, CO_2, CO, and formaldehyde. Under such noncatalytic conditions, the CeO_2 or Fe_2O_3 is reduced and deactivated by the reaction with JP-10. Decomposition of JP-10 in the presence of stoichiometric O_2 was also studied, with and without CeO_2 present. In absence of CeO_2, some oxidation products are observed; however, the rate limiting step appears to be pyrolysis of JP-10, and pyrolysis products dominate for temperatures up to 1200 K. When both O_2 and CeO_2 are present, oxidation is clearly catalytic, i.e., oxidation is initiated by reaction of JP-10 with CeO_2, which is then reoxidized by O_2.

2.2 Introduction

JP-10 (exo-tetrahydrodicyclopentadiene, $C_{10}H_{16}$) is a synthetic fuel, currently used in applications where high volumetric energy density is critical. Its heat of combustion (39.4 MJ/L) is substantially higher than petroleum-based fuels such as JP-8 (34.5 MJ/L). JP-10 is commonly used in combustion research,[1-14] at least partly because it is a single component fuel, and therefore much simpler to study than a petroleum distillate. One problem with JP-10, also affecting other liquid hydrocarbon

fuels to varying extents, is that its ignition and combustion kinetics can be too slow for efficient combustion in applications such as pulse detonation engines or ramjets. Furthermore, while JP-10 has volumetric energy density near the limit for readily synthesized liquid hydrocarbons, immediate benefits would accrue from development of a fuel system with even higher energy density. We are interested in nanoparticle fuel additives for hydrocarbon fuels, designed to simultaneously enhance combustion rates and energy density. The idea is to have nanoparticles with a core of high energy density material, coated with a thin shell of a catalyst that accelerates ignition and combustion of the hydrocarbon (e.g., JP-10) carrier fuel. Palladium or other noble metal-based catalysts are commonly used in catalytic combustors to increase the efficiency of combustion at low temperatures, thereby reducing NO_x production. For such applications, the reactant gases typically flow through a bed containing the catalyst immobilized on a high surface area support. For aircraft propulsion, this approach is ruled out by gas flow velocity, contact time, size, and weight limitations. In the envisioned application, the catalyst-coated fuel particles will be injected into the combustor with the fuel and/or air, and be consumed in the combustion process. For this reason, the catalyst must be inexpensive and have low toxicity as well. Here we report the first studies of catalytic combustion of JP-10, using nanoparticulate CeO_2 as the catalyst. Substantial reduction in ignition temperature is observed, and it is demonstrated that initiation is by CeO_2 oxidation of JP-10, with O_2 serving primarily to close the catalytic cycle by re-oxidizing the CeO_2. Fe_2O_3 nanoparticles are also shown to be active for JP-10 oxidation. Such catalysts could have wider applications than our core/shell nanoparticle approach, in coatings on engine surfaces, for example. The

choice of JP-10 as the hydrocarbon fuel was largely to simplify mass spectrometric analysis. Qualitatively similar results are expected for other hydrocarbon fuels.

2.3 Experimental

The micro-flow tube reactor mass spectrometer instrument used in these experiments is described below. In essence, the instrument consists of a small flow tube reactor, where chemistry is carried out, coupled to a tandem mass spectrometer for product detection and identification. The main changes over earlier versions of the instrument,[15-18] were made to allow higher flow rates and pressures, and to enable feeding of nanoparticles into the gas flow. Because the gas density is too low to carry the nanoparticles through the flow tube, the tube is oriented vertically, as shown in Figure 2.1. A 15 cm section, located 1 cm from the outlet end of the 46 cm long, 1.6 mm inner radius alumina flow tube, is heated by external tantalum windings and can reach temperatures as high as 1800 K. A standard K-type thermocouple is embedded into the wall of the tube to monitor temperature, and is periodically calibrated against a thermocouple inserted into the flow tube bore. The nanoparticle-laden gas stream exiting the flow tube is mostly pumped away by a large (40 L/s) mechanical pump, equipped with a particle trap to prevent nanoparticle contamination of the pump oil. The central portion of the gas stream is allowed to enter the differentially pumped ionization chamber through a 1 mm aperture in a skimmer cone, forming a molecular beam. The gas beam passes through an electron-impact ionization source, and then into a 160 L/s diffusion pump located at the bottom of the ionization chamber. Ions are created by electron impact at an ionization energy of 75 eV, extracted along the horizontal axis, and analyzed by a tandem mass spectrometer instrument. Ionization
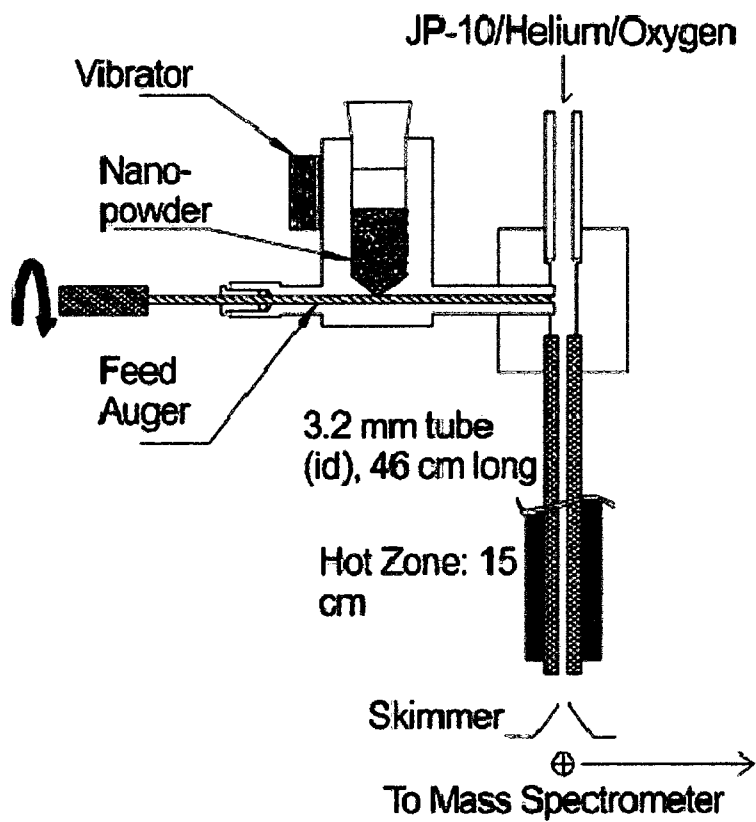
Figure 2.1 Nanoparticle feed mechanism.

chamber pressure is typically 5.5 x 10^{-5} Torr during operation.

For the measurements, either helium or O_2 is bubbled though a container of liquid JP-10 (Koch, ~95%) at room temperature (vapor pressure ~ 2.6 Torr), with the gas pressure adjusted to give a gas mixture of either ~3.9% JP-10 in helium, or 6.7% JP-10 in O_2, the latter being the stoichiometric ratio for combustion to CO_2 and H_2O. The gas mixture is then metered into the flow tube through a needle valve, to give a flow tube entrance pressure of 20.1 Torr, as measured by a Baratron capacitance manometer. At the top of the flow tube, nanoparticles are introduced via a feed mechanism, consisting of an evacuated hopper containing the nanoparticulate powder and a motorized 2.89 mm diameter auger that delivers powder at a controlled rate from the hopper to a delivery ramp positioned above the flow tube center line. To help feed particles smoothly, break up clumps, and disperse the powder across the flow tube cross section, the entire feed assembly is shaken by an electro-mechanical vibrator. The experiments used CeO_2 and Fe_2O_3 nanopowder from commercial sources. The CeO_2 (Nano-Scale Materials) had specified average particle diameter of 120 nm, and the Fe_2O_3 (Sigma Aldrich) had a specified average diameter of 20-25 nm. The average nanoparticle feed rate was typically ~1.4 mg/sec, determined by weight loss during the experiments. For reasons discussed below, the exact feed rate is not critical.

To understand the catalytic effects, it is important to review the properties of the flow tube reactor. Table 2.1 summarizes the most important flow properties, calculated assuming incompressible flow. The inlet pressure at the top of the tube is typically set to 20.1 Torr. Because the hot zone is preceded by a room temperature zone that is ~200 tube radii long, very little adjustment of the gas flow rate is needed to maintain constant

Table 2.1 Flow-tube properties.

	JP-10/He		
	300 K	900 K	1400 K
flow velocity	16.4	34.8	45.4
mach number	0.02	0.02	0.02
hot zone midpoint pressure (Torr)	8.1	11.6	13.8
residence time (ms)	9.1	4.3	3.3
JP-10 diffusion speed (m/s)	2.2	6.1	8.9
average number of hot zone JP-10-wall collisions	12.4	16.4	18.3
	JP-10/O_2		
	300 K	900 K	1400 K
flow velocity	15.4	32.5	42.4
mach number	0.05	0.06	0.06
hot zone midpoint pressure (Torr)	8.1	11.6	13.8
residence time (ms)	9.8	4.6	3.5
JP-10 diffusion speed (m/s)	1.2	3.4	5.0
average number of hot zone JP-10-wall collisions	7.5	9.9	11.0

inlet pressure, and fully laminar flow develops long before the hot zone. Assuming that the pressure at the outlet of the tube is equal to the vacuum chamber pressure (~0.1 Torr), we estimate that the pressures at the beginning, mid-point, and end of the hot zone are 11.5, 8.1, and 2.1 Torr, respectively, for a flow tube temperature of 298 K. The final 1 cm (~6 tube radii) of the tube is unheated, and clamped into a room temperature holder, so that the large pressure drop near the tube outlet is spatially separated from the hot zone. The mass-averaged flow velocity is such that the average residence time for JP-10/He in the hot zone is ~9.1 ms at 298 K, dropping to 3.3 ms at 1400 K. As indicated in the table, the residence time is slightly longer for the JP-10/O_2 mixture. The pressure at the hot zone midpoint is nearly identical for the two gas mixtures. Under these conditions the mean free path for JP-10 collisions with the He or O_2 carrier is on the order of 10 μm, i.e., ~200 times smaller than the tube radius. The corresponding JP-10 diffusion speed is such that the molecules diffuse across the flow tube on the order of ten times during the hot zone residence time. This diffusion averages out the laminar flow velocity gradient, allowing the flow to be treated as pseudo-plug flow, with uniform average residence times. Diffusion and wall collisions also insure that the gas temperature closely follows the wall temperature, with rapid heating upon entering the hot zone. Finally, wall collisions provide a reproducible and easily characterized method to study chemistry in JP-10 – nanoparticle collisions.

The latter point is important, because dry nano-particulate powder is typically aggregated. In our case, the average CeO_2 nanoparticle size is 120 nm, but electron microscopy shows that the dry powder is aggregated into ~5 μm grains. We have found that ultrasonication in liquid JP-10 breaks up the aggregates, providing means to

achieve high dispersion in combustion applications. For the present dry-feed experiments, however, aggregation is unavoidable. Furthermore, it is nontrivial to feed powder smoothly into a gas stream at the low pressures and flow rates possible in our instrument. As a consequence, it is difficult to achieve conditions where JP-10 makes a well-defined number of collisions with nanoparticles dispersed in the gas stream. Furthermore, at our low operating pressures, it is unclear if CeO_2 aggregates flowing in the gas stream would reach the wall temperature during the short hot zone residence time.

Fortunately, for our purposes it is sufficient to have a controllable rate of JP-10 – particle collisions at well defined temperatures, and it is immaterial whether the particles are entrained in the gas flow or immobilized on the flow tube walls. An obvious approach would be to simply coat the flow tube walls with CeO_2 or Fe_2O_3 powder prior to use, however, interpretation would be complicated by possible changes in catalyst activity with time and operating conditions (see below). Our approach is to feed nanoparticles into the gas flow continuously, with the idea that enough will stick to the walls to provide a coating that is continually renewed with fresh material. Post-use examination of several flow tubes shows that nanoparticles do stick, generating a continuous coating that extends all along the tube length. For the feed rate and average aggregated particle size in these experiments, we can estimate that a few percent of particles sticking to the walls is sufficient to re-coat the walls on a ~5 min time scale. Because catalyst deactivation occurs on a slower time scale even under strongly reducing conditions (see below), it is reasonable to assume that most of the wall surface is coated with active material. The catalyst coating builds up slowly during a series of

experiments, but is never allowed to grow to the point where it significantly changes the tube diameter, i.e., where it would affect the flow properties. Analysis of JP-10 encounter rates with free and immobilized particles is described below, but the result is that chemistry is dominated by the immobilized particles.

In our previous studies of pyrolysis of JP-10,[19,20] quadricyclane,[15] and cubanes,[21] we found that decomposition catalyzed by alumina and silica flow tube surfaces was negligible, with the probable exception of dehydrogenation reactions occurring at temperatures well above those examined here. The lack of significant wall-catalyzed chemistry reflects the relative inertness of both silica and alumina. Moreover, we found that the silica and alumina surfaces quickly became coated by a thin grey carbonaceous layer. Once formed, this layer is stable for hundreds of hours of operation, and we speculated that it passivates the surface, reducing the wall reactivity. In the results below, we compare JP-10 decomposition for CeO_2- or Fe_2O_3-coated flow tubes, with that observed under identical flow conditions for new (i.e., never exposed to catalyst) alumina flow tubes. Any differences in chemistry are clearly attributable to reactions on the CeO_2 or Fe_2O_3 particles.

Two types of mass spectral scans were used. To find the onset temperatures for JP-10 breakdown for different experimental conditions, the parent mass (136) was monitored continuously as the flow tube temperature was stepped in ~10 K increments. Once the onset temperature was found, the product distribution was examined by taking full mass spectra at several temperatures above and below the breakdown onset. These mass spectra were taken with ~5 data points per atomic mass unit. To simplify quantitative comparison of spectra, the intensities are plotted as "stick" spectra, where

height is proportional to the integrated intensity of each mass peak. The spectra were all normalized to constant total ion intensity for plotting. Fitting, described below, was then used to extract the composition of neutral species contributing to the mass spectrum at each temperature.

2.4 Results and discussion

2.4.1 JP-10 Pyrolysis

Because our current flow tube differs in several respects from that used in our previous pyrolysis study, simple pyrolysis was re-characterized. Figure 2.2 shows a series of mass spectra of 3.9% JP-10 in He, taken after passage through a clean alumina flow tube at several different temperatures. No CeO_2 or Fe_2O_3 was present in these experiments. The bottom spectrum, for 300 K flow tube temperature, corresponds to intact JP-10 entering the ion source. There is a peak at the molecular mass (136); however, the spectrum is dominated by electron-impact-induced fragmentation, yielding a characteristic "fingerprint" pattern for JP-10. The extensive fragmentation is consistent with photoionization experiments by Federova et al.[22] showing that a variety of C_5, C_6, C_7, C_8 and C_9 fragment ions have appearance energies within 1 eV of the JP-10 ionization threshold. The spectrum is also similar to what we previously reported,[19,20] and the differences in relative peak intensities are attributable to the rather different ion source used in those experiments.

As the flow tube temperature is increased, no mass spectral changes are observed for temperatures up to ~900 K, indicating that JP-10 remains intact on the millisecond time scale. The mass 136 intensity is observed to drop ~7% at 920 K, and examination of the corresponding mass spectrum also shows subtle changes in the relative intensities
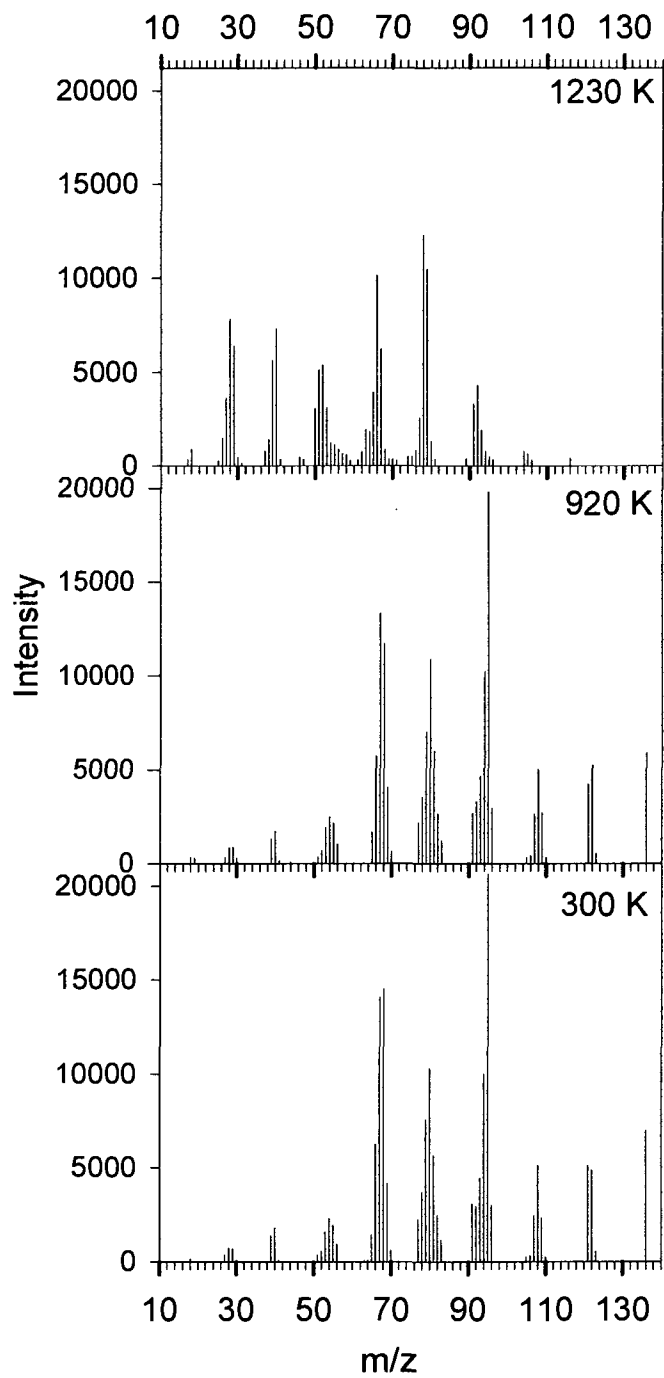
Figure 2.2 Pyrolytic breakdown of JP-10.

of some fragment peaks, indicating new contributions to these masses from ionization of JP-10 pyrolysis products. At higher temperatures, JP-10 is increasingly pyrolyzed, and by 1230 K, no JP-10 survives passage of the flow tube, as shown by absence of the parent peak (136). Evolution of the product distribution with temperature was explored in detail in our previous experiments,[19,20] and the similarity to the present results (see below) indicates that the pyrolysis chemistry is not significantly affected by our modest changes in flow tube operating conditions.

These pyrolysis results provide a baseline against which the effects of CeO_2 or Fe_2O_3 nanoparticles can be evaluated. Figure 2.3 shows analogous plots for breakdown of JP-10 in the presence of CeO_2 at 620 K (just above the onset temperature), 920, and 1150 K flow tube temperatures. The room temperature spectrum is not shown, because it is essentially identical to that shown in Figure 2.2, where no CeO_2 was present. The implication is that room temperature CeO_2 does not react with JP-10 nor catalyze its breakdown. A comparison of Figure 2.3 with Figure 2.2 shows that there is already more JP-10 breakdown at 620 K with CeO_2, than is observed at 920 K in absence of CeO_2. This breakdown is observed as intensity reductions for peaks characteristic of JP-10 (cf. masses above 100) and the appearance of product peaks, the most obvious being 18 (water) and 44 (CO_2). At 920 K, the JP-10-characteristic peaks continue to decrease, and peaks characteristic of products (18, 28-31, 44) continue to grow. Finally, JP-10 is completely decomposed at 1150 K, i.e., about 100 degrees lower than in the absence of CeO_2. Comparison of the topmost spectra in Figures 2.2 and 2.3 shows that the product distribution is quite different, as well. In absence of any oxidizer (Figure 2.2), the products are all hydrocarbon fragments from pyrolysis. When
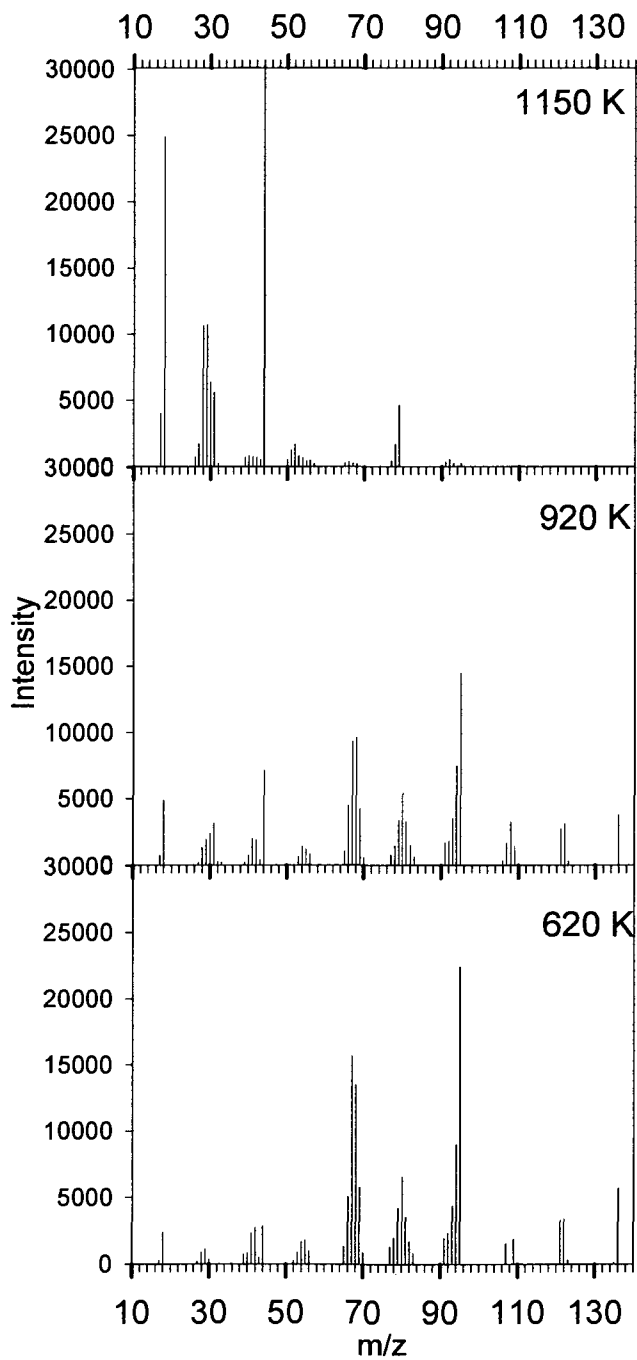
Figure 2.3 Breakdown of JP-10 with CeO_2.

CeO_2 is present, we might expect that the product distribution at 1150 K should contain both hydrocarbons from JP-10 pyrolysis, and oxidation products from reaction with CeO_2. As shown in Figure 2.3, however, oxidation is dominant, and there is relatively little signal for hydrocarbon products pyrolysis products (compare masses > 50 in Figures 2.2 and 2.3).

In order to obtain a more quantitative understanding of the chemical species present during the breakdown of JP-10, it is necessary to fit the raw spectra, accounting for EI-induced fragmentation of the various neutral species present in the flow tube exhaust stream. Fitting was done using a contracting grid, least squares fit program and procedures described previously.[19] In essence, the spectra at each flow tube temperature were fit to linear combinations of basis spectra for compounds known or suspected to be present. For the pyrolysis (i.e., CeO_2-free) spectra, the analysis assumed a product distribution similar to what was observed in our earlier study.[19,20] Basis spectra were included for C_2H_2 (acetylene), C_2H_4 (ethylene), C_3H_4 (propyne), C_5H_6 (cyclopentadiene), C_6H_6 (benzene), C_4H_x, C_7H_x, and the parent JP-10. For JP-10, the basis spectrum is simply the room temperature EI spectrum (Figure 2.2, bottom), and for the various product species, the basis spectra were taken to be standard mass spectra present in the NIST Standard Reference Database.[23] The C_4H_x and C_7H_x basis spectra are synthetic spectra generated to fit the residual intensity in the 50 - 56 and 90 - 95 mass ranges, respectively, where no single molecule in the NIST database is capable of fitting the observed mass pattern.[19] For spectra obtained with CeO_2, Fe_2O_3, and/or O_2 present, we simply added basis spectra for water, CO, CO_2 and H_2CO to the set of hydrocarbon pyrolysis products. The raw fits give the contribution of each basis

spectrum to the *ion* intensity distribution at each temperature. The results are given as the contribution of each *neutral* species to the product distribution at each temperature, correcting for the species dependence of EI detection efficiency, assuming linear scaling with the number of electrons in each molecule, as suggested by Flaim and Ownby,[24] and Nishimura and Tawara.[25] We also include a series labeled "unfit residuals," which accounts for no more than 10% of the observed intensity at any temperature. The dominant contribution to the unfit residuals is discussed below.

Figure 2.4 (bottom frame) shows the product mole fraction distribution for pyrolysis of JP-10 as a function of temperature, extracted from the fitting. For clarity, the JP-10 mole fraction is omitted from Figure 2.4, and plotted separately in Figure 2.5 to allow for a comparison of the breakdown under different experimental conditions. At 1150 K, i.e., the lowest temperature where there is enough decomposition to reasonably discuss the product distribution, the dominant products are benzene and cyclopentadiene (CPD), and benzene continues to be a major product at higher temperatures. CPD is, itself, unstable under our conditions at higher temperatures,[19] thus its contribution to the product distribution diminishes, to be replaced by a variety of C_2, C_3, and C_4 products. There is additional secondary breakdown at higher temperatures; here we restrict our attention to the temperature range below 1230 K, i.e., up to the point where no JP-10 survives.

Figure 2.4 (top frame) gives analogous fitting results for breakdown in the presence of CeO_2, with the JP-10 breakdown behavior plotted separately in Figure 2.5. Figure 2.5 shows that decomposition sets in at ~300 K lower temperature with CeO_2 than without, and also is complete at ~100K lower temperature. Figure 2.4 shows that
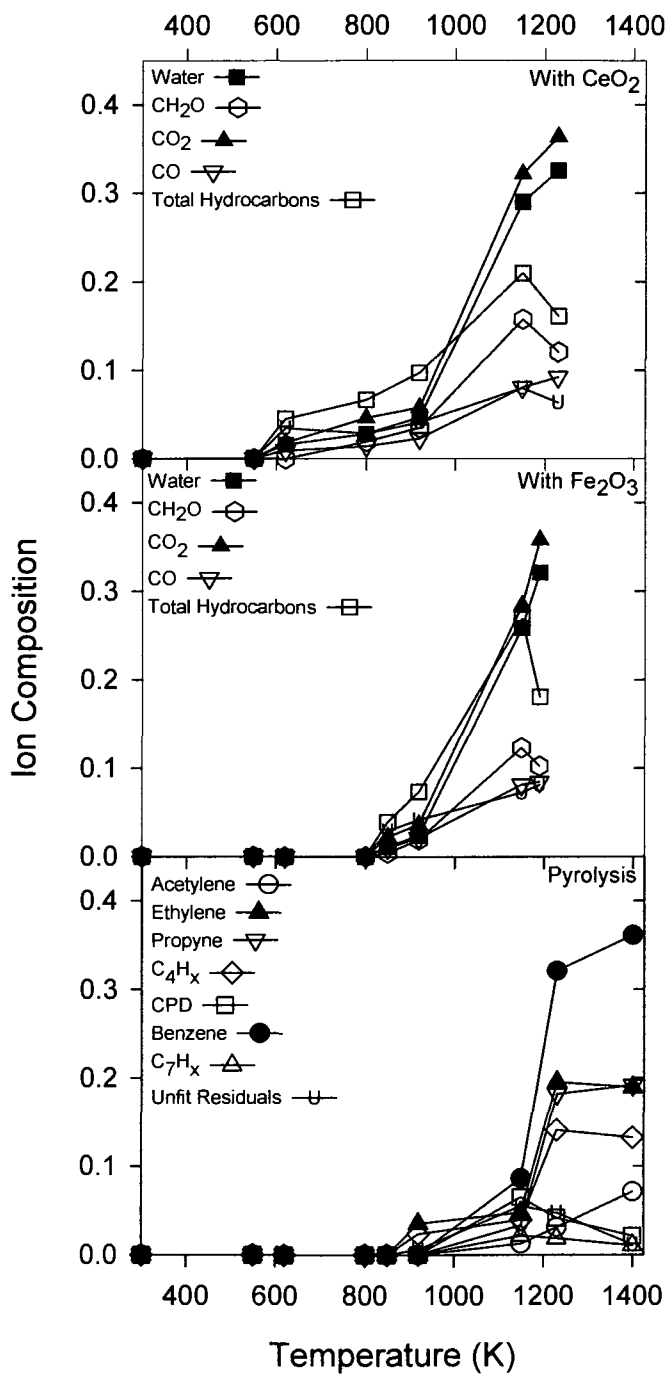
Figure 2.4 Breakdown products.
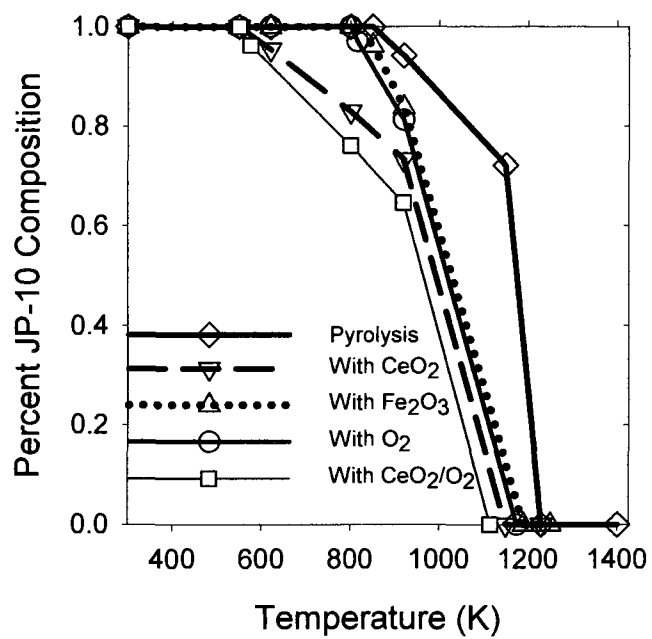
Figure 2.5 Percent JP-10 composition (various conditions).

water, CO, CO_2, and formaldehyde, i.e., oxidation products, account for ~85% of the product distribution at 1150 K. Within the considerable uncertainty that results from their small contribution to the spectra, it appears that the distribution of hydrocarbon products is consistent with simple pyrolysis. Note that there is ambiguity regarding identification of some products. For example, mass 30 could have contributions from both ethane and formaldehyde. Because the pyrolysis mass spectra (Figure 2.2) have negligible mass 30 intensity, we attribute the bulk of the mass 30 appearing upon CeO_2 addition to formaldehyde. Similarly, propane shares the same mass as CO_2, but we assume that mass 44 in Figure 2.3 is largely CO_2, because there is no evidence for propane in the pyrolysis product distribution (Figure 2.2). Mass 28 could be either C_2H_4 or CO, and comparison of the intensity pattern for mass 26 - 28 suggests that both are present, in a ~2:1 ratio ($CO:C_2H_4$).

The only major mass peak without a clear assignment is mass 31 (CH_3O^+). Given that the rest of the peaks can be accounted for by EI of various stable molecules, the obvious assignment would be to an EI fragment ion from some heavier neutral product. The obvious candidates can, however, be ruled out from the mass spectra. For example, methanol fragments in EI to give substantial intensity at mass 31, but it also gives substantial peaks at mass 32 (CH_3OH^+) and mass 15 (CH_3^+), neither of which is observed. Dimethyl peroxide and 1,2-ethanediol both give substantial mass 31 peaks under EI conditions; however, they can be ruled out by the observed absence of peaks at mass 62 and 33, respectively. Similar arguments apply to other candidate neutrals. Because mass 31 appears only when CeO_2 (or Fe_2O_3) is present, it is clear that the carrier of this signal must form by reaction of JP-10 (or a JP-10 breakdown product)

with the CeO_2 or Fe_2O_3 surface. In absence of any plausible alternatives, we tentatively attribute mass 31 to EI of a radical product, most likely CH_2OH ($\Delta_f H$ = -9 kJ/mol)[26] or possibly CH_3O ($\Delta_f H$ = +17 kJ/mol).[26] Because no standard mass spectrum exists for either radical,[23] the mass 31 signal is simply lumped into the unfit residuals, accounting for about half the residual intensity for all experiments where CeO_2 or Fe_2O_3 was present.

2.4.2 JP-10 with Fe_2O_3

It is clear from the above results that CeO_2 can serve as an oxygen source at relatively low temperatures, oxidizing JP-10 well below the temperatures required for pyrolysis. CeO_2 is inexpensive and has relatively low toxicity. Nonetheless, it would be desirable to find an even cheaper and nontoxic material. For comparison with CeO_2, Figure 2.6 presents analogous results for a (CeO_2 - free) flow tube with Fe_2O_3 nanopowder being fed continuously, at a feed rate similar to that for the CeO_2 experiments. As with CeO_2, no decomposition is observed at low temperatures, in this case, up to ~800 K. The lower spectrum is for the lowest temperature where significant JP-10 decomposition was observed (850 K). The decomposition is most obviously shown by the presence of peaks for water and CO_2; however, comparison with the bottom spectrum in Figure 2.2 shows some decrease in JP-10 intensity and other subtle changes as well. The top spectrum is for the first temperature (1190 K) where complete JP-10 decomposition was observed for Fe_2O_3. As in the CeO_2 case, the dominant products are water, CO_2, formaldehyde, and CO; however there are also somewhat higher levels of hydrocarbon products than for CeO_2 in the same temperature range.
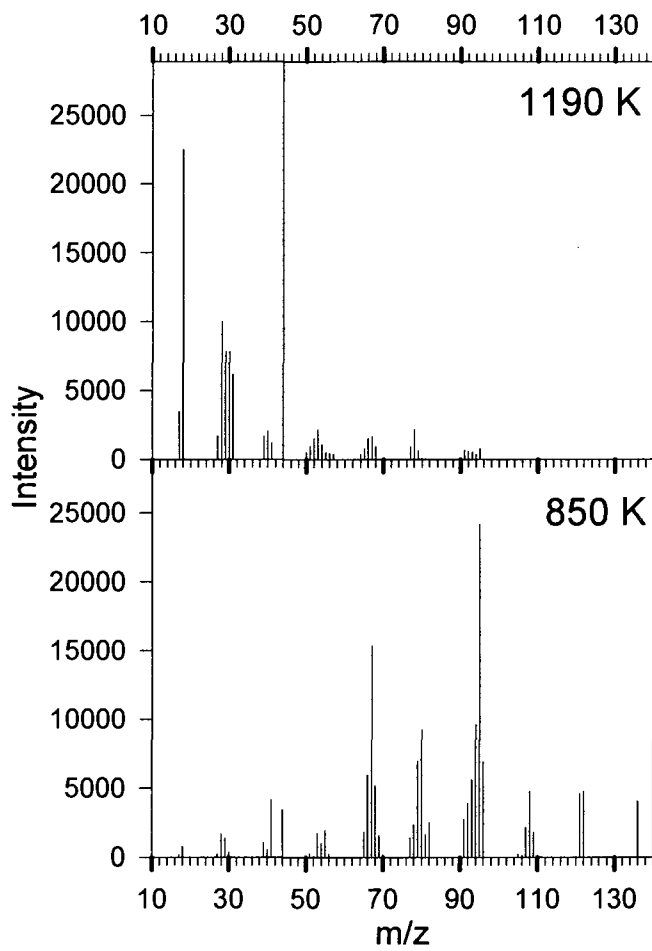
Figure 2.6 Breakdown of JP-10 with Fe_2O_3.

Figures 2.4 (middle frame) and 2.5 show the fitting results obtained for the Fe_2O_3 - coated flow tube. Figure 2.5 indicates that the JP-10 breakdown behavior is intermediate between that of the alumina tube, and the CeO_2-coated tube. The onset temperature for decomposition is only slightly lower than is observed for alumina tubes (i.e., for pyrolysis); however, the extent of decomposition increases more rapidly with temperature, and is rather similar to the CeO_2 case for temperatures above ~950 K. At the onset of decomposition, hydrocarbon pyrolysis products dominate, but oxidation products such as water, CO, CO_2, and formaldehyde dominate at high temperatures. At 1190 K (the temperature where full JP-10 decomposition was observed), oxidized products such as water, CO_2, CO, and formaldehyde constitute about 75 % of the product species, compared to ~85 % for CeO_2 at 1150 K. The pattern suggests that Fe_2O_3 is relatively unreactive with intact JP-10 at temperatures up to the point where JP-10 pyrolysis begins; however, Fe_2O_3 clearly accelerates oxidative destruction of JP-10 at higher temperatures, presumably by reacting with both JP-10 and its pyrolysis products. As discussed next, the effects of Fe_2O_3 are strikingly similar to those seen when JP-10/O_2 mixtures are reacted in absence of any active oxide coating of the reactor.

Although the effects of Fe_2O_3 and CeO_2 are similar for temperatures above 1150 K, Fe_2O_3 is considerably less active at initiating JP-10 breakdown at low temperatures, i.e., in the range expected to be most important for catalytic enhancement of hydrocarbon ignition and combustion. For this reason, catalytic JP-10 combustion and catalyst deactivation studies were only performed for CeO_2. Nonetheless, the activity

observed for Fe_2O_3, combined with its low cost and toxicity, suggests that activity studies for other first row transition metal oxides are warranted.

2.4.3 JP-10 combustion, with and without CeO_2

The above results show that CeO_2 will react with and oxidize JP-10, substantially reducing the onset temperature for decomposition. From a combustion perspective, the more important question is how effective CeO_2 is at catalyzing JP-10 ignition and combustion in JP-10/O_2 mixtures. To address this question, experiments similar to those above were carried out, but with the helium carrier gas replaced by O_2. To simplify the analysis, we used JP-10 in pure O_2 with the JP-10/O_2 mixing fraction set to the stoichiometric ratio for complete combustion to CO_2 and water:

$$14O_2 + C_{10}H_{16} \rightarrow 10CO_2 + 8H_2O.$$
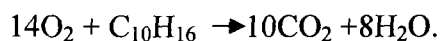
JP-10 is an energetic fuel; thus, we might anticipate significant energy release under combustion conditions, possibly raising the flow-tube temperature for JP-10/O_2 relative to that for JP-10/He under similar heater power. There are several ways to estimate the possible temperature rise as a result of combustion. For the mass flow rate used here, complete combustion of the JP-10/O_2 mixture to CO_2 and H_2O would release ~7.9 W. Simply on the basis of the heat capacity of the gas mixture, this would result in a substantial temperature rise; however, as discussed above, diffusion leads to tens of wall collisions during the residence time and we expect that the gas temperature remains near that of the tube walls; i.e., the combustion energy is rapidly transferred to the walls, which have a very large heat capacity compared to that of the gas. Because we control the wall temperature, the measurements largely take this additional heating power into account. Because the combustion power is small compared to the heater

power (~210 W in the middle of the experimental temperature range), the change in the heater power-temperature relation is small.

Figure 2.7 shows the mass spectra resulting from passing the stoichiometric JP-10/O_2 mixture through the flow tube at 815 K, 920 K and 1175 K, *with no CeO_2 catalyst present.* No reaction is observed at lower temperatures. These experiments were done with a new, CeO_2-free flow tube to ensure that any catalytic contribution comes only from the relatively inert alumina surface. It is useful to compare JP-10 breakdown for JP-10/He and JP-10/O_2, in each case without CeO_2 (Figures 2.2 and 2.7). When O_2 is present, the temperature where significant JP-10 breakdown is observed decreases from ~920 K to 815 K, and the temperature required for complete JP-10 disappearance decreases from 1230 K to ~1175 K. As shown in Figure 2.5, JP-10/O_2 is rather similar to JP-10/He with Fe_2O_3. Both have little effect on the initiation temperature for JP-10 decomposition, but enhance breakdown (relative to pyrolysis) at higher temperatures. The two oxidizers differ, however, in that the fraction of fully oxidized products (H_2O, CO, CO_2) at high temperatures is much smaller for O_2 than Fe_2O_3, i.e., the two oxidizers have similar efficiency for JP-10 decomposition, but Fe_2O_3 is more efficient at driving complete oxidation.

In pyrolysis (i.e., JP-10/He), JP-10 breakdown is obviously initiated by some isomerization or bond rupture event in JP-10. The slight decrease in onset temperature for JP-10 breakdown in O_2, relative to JP-10/He, might tend to suggest that some reaction involving O_2 becomes rate-limiting when O_2 is present. In fact, we believe that JP-10 pyrolysis remains rate-limiting, even when oxygen is present. This conclusion rests on previous comparisons of decomposition behavior for JP-10/He,
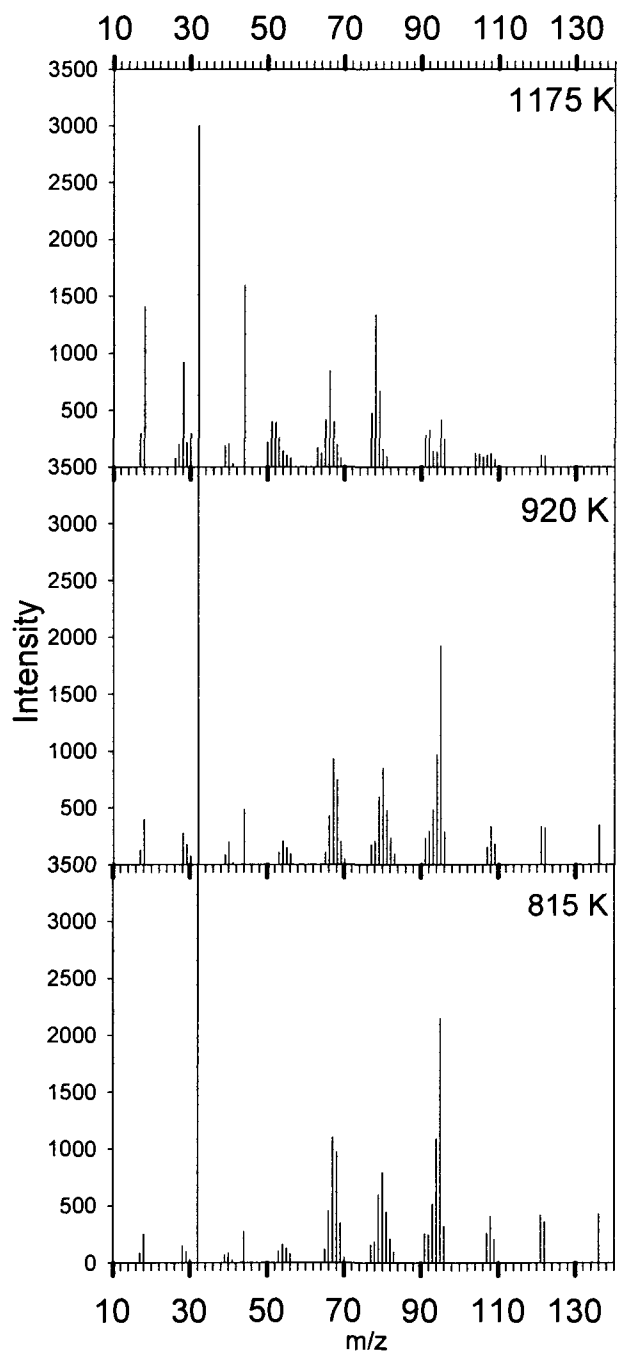
Figure 2.7 Breakdown of JP-10 with stoichiometric O_2 (no CeO_2).

with that for JP-10 in He with up to 10 % O_2 added.[20] These O_2 levels are high enough to insure that JP-10 collides frequently with O_2 in the hot zone, but low enough that the gas flow properties are not strongly modified. No changes in onset temperature were observed in those experiments, although the temperature for complete JP-10 disappearance was reduced, as is observed in the present experiments. This observation suggests that JP-10 pyrolysis is the rate-limiting step, but that additional reactions with O_2 accelerate JP-10 destruction once pyrolysis has begun.

The question is why the onset temperature observed here for JP-10 in stoichiometric O_2 is shifted to a lower temperature. One contributing factor is simply that the hot zone residence times for JP-10/O_2 are ~10% longer than those for JP-10/He, which would tend to allow observable pyrolysis to occur at somewhat lower temperatures. A possible additional factor is that the presence of stoichiometric O_2 may increase the activity of the alumina flow tube surface, by suppressing the formation of the carbonaceous layer observed for JP-10/He. The absence of an onset temperature shift in the experiments with O_2 diluted in helium is not surprising, because those mixtures were fuel rich (equivalence ratio < 0.1), so that suppression of carbon deposition would not be expected. Regardless of the cause, the temperature shift is small compared to what is seen for JP-10/O_2 when CeO_2 is added.

Figure 2.8 shows mass spectra recorded for the case of JP-10/stoichiometric O_2, in the presence of CeO_2. In this case, JP-10 breakdown is significant already at 575 K, compared to 815 K with O_2 but without CeO_2, 620 K with CeO_2 but no O_2, and 920 K for simple JP-10 pyrolysis without either oxygen source. Furthermore, the JP-10 is completely gone at 1115 K, and at this temperature the product distribution is almost
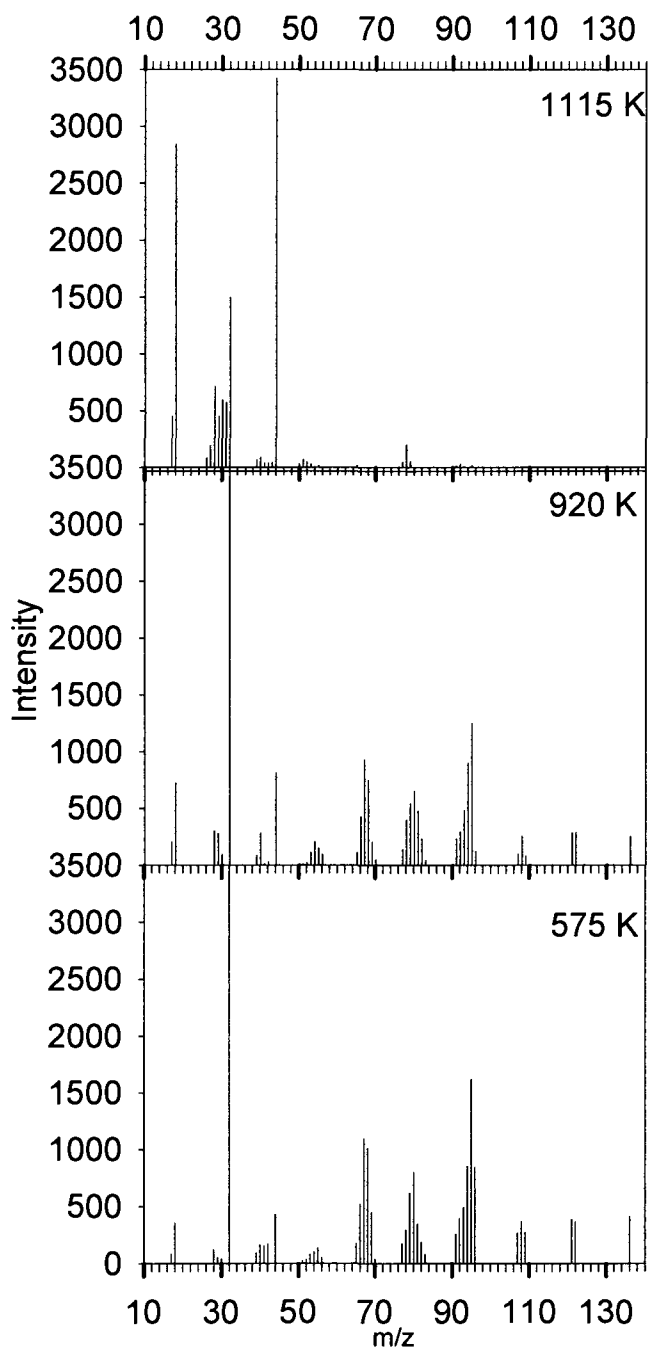
Figure 2.8 Breakdown of JP-10 with stoichiometric O_2 (with CeO_2).

entirely oxidation products, with only a few percent of residual hydrocarbons. A comparison of the CeO_2 results in Figure 2.5 for JP-10/O_2 and JP-10/He suggests that the onset temperature is not strongly affected by the presence of stoichiometric O_2. The small shift is probably attributable to longer residence time for JP-10/O_2, as discussed above. This result indicates that JP-10 reaction with CeO_2 is the rate-limiting step in both cases.

The above results show that both CeO_2 and O_2 can, by themselves, oxidize JP-10, with CeO_2 being the more active oxidizer. The key question is whether the enhanced oxidation chemistry observed when both O_2 and CeO_2 are present simply represents the additive effects of oxidation by CeO_2 and O_2, or if real catalytic oxidation is occurring. This point is important, because in any catalytic propulsion application, the goal would be to add the minimum amount of catalyst, because oxide catalysts would simply be dead weight, reducing the energy density of the fuel system. Two observations clearly show that real catalysis is occuring.

Compare the highest temperature spectra for JP-10/O_2 (Figure 2.7) and JP-10/O_2 with CeO_2 (Figure 2.8). If the much greater extent of oxidation in Figure 2.8 (compare residual hydrocarbon signal) were simply the effect of additional oxygen supplied by CeO_2, we should see a similar or smaller fraction of the initial O_2 consumed when CeO_2 is present. Instead, it can be seen that consumption of O_2 is more complete when CeO_2 is present, i.e., CeO_2 has catalyzed O_2 consumption, and by inference, JP-10 oxidation.

The catalytic effect can be seen more directly in experiments such as that summarized in Figure 2.9. Here, a JP-10/He flow was passed through the flow tube, with continual CeO_2 feed at 920 K, i.e, at a temperature where substantial JP-10
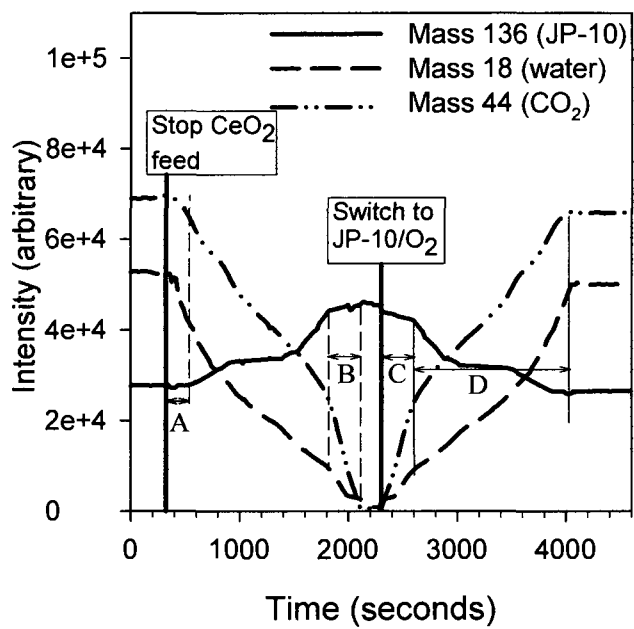
Figure 2.9 Catalyst reactivation.

decomposition occurs only in the presence of active CeO_2. The intensities of the JP-10 parent (mass 136) and the major decomposition products (water and CO_2) were monitored to establish a baseline for the amount of decomposition. The CeO_2 feed was then stopped while maintaining the JP-10/He gas flow, and changes in the parent and product intensities were continuously monitored. Note that the decomposition chemistry gradually stops, i.e., water and CO_2 disappear and the mass 136 signal increases. Eventually the signals reach a new steady state at ~2000 s, with no water or CO_2 production, and JP-10 intensity close to what would be observed for JP-10/He in a alumina tube at this temperature. Clearly, the reaction with JP-10 in the absence of O_2 completely deactivates the ceria coating on the tube walls on a ~2000 s time scale. The final step in the experiment was to switch the gas mixture to stoichiometric JP-10/O_2, leaving the CeO_2 feed turned off. Note that the mass 136 intensity decreases, and the water and CO_2 intensities increase, with the system eventually reaching a new steady state after ~30 min. At steady state, the (CO_2+H_2O)/JP-10 intensity ratio is almost identical to that seen when CeO_2 is being fed continuously. More importantly, the ratio is~50% greater than that seen at this temperature for JP-10/O_2 in absence of CeO_2 (Figure 2.7). The implication is that at steady state, the CeO_2 coating remains catalytically active under stoichiometric conditions, i.e., it supplies oxygen to the JP-10, and the catalytic cycle is closed by O_2 re-oxidizing the surface.

A close examination of Figure 2.9 provides additional insight into the deactivation and reactivation mechanisms. Note that the time dependence of the signals is more complex than might be expected if only a single deactivation/reactivation process were occurring. Instead, it is clear that both deactivation and reactivation occur

in at least two steps, and even within the steps, the time dependence is not simple. For example, note that when the CeO_2 flow is stopped, there is a ~250 s induction period before the JP-10 intensity begins to increase (time period A), whereas the CO_2 and H_2O signals both begin to decrease immediately. This behavior indicates that the CeO_2 layer continues to decompose JP-10 efficiently, but is increasingly unable to supply enough oxygen to generated fully oxidized products. Given that the CeO_2 is reduced by reaction with JP-10, such a loss of oxidizing capacity is not surprising. Note also that in the final period of deactivation (time period B), the JP-10 intensity has nearly reached the steady state value indicating that no decomposition is occurring, while CO_2 and H_2O continue to be produced, albeit with rapidly declining intensities. This pattern indicates that the tube walls are inactive for decomposition of JP-10 during this period, but that they continue to evolve CO_2 and H_2O, presumably by oxidation of hydrocarbons deposited on the walls earlier in the experimental sequence.

We conclude that CeO_2 deactivation results from two effects. The initial stage is gradual reduction of the ceria oxidation state, such that the surface becomes progressively less active. Initially JP-10 still decomposes on the walls, but not to fully oxidized products (time period A). As the ceria becomes less active, JP-10 decomposition and CO_2 and H_2O production continue to decrease (period around 1000 seconds). In the final stages of deactivation, we speculate that a carbonaceous film grows on the CeO_x surfaces, passivating them with respect to further JP-10 decomposition (period B). This film, in intimate contact with the CeO_x, continues to evolve CO_2 and H_2O to a diminishing extent, until the CeO_x is completely deactivated.

The reactivation phase of the experiment also supports the idea of a passivating carbonaceous layer. If the only source of CO_2 and H_2O were oxidation of JP-10, then the increase in CO_2 and H_2O intensities immediately after switching to the JP-10/O_2 mixture (time period C), should mirror the decrease in JP-10 intensity. Instead, the initial increase in CO_2 and H_2O signals is much more rapid than can be explained by JP-10 combustion. This pattern suggests that O_2 initially reacts primarily with the carbonaceous layer, generating CO_2 and to a lesser extent, H_2O. Only after the carbonaceous layer is burned off, does O_2 begin to reactivate the underlying ceria, at which point the rate of JP-10 decomposition increases, and the CO_2 and H_2O intensities come back in line with the JP-10 combustion stoichiometry (time period D). In considering stoichiometry, it is important to note that the intensities in Figure 2.9 are not corrected for relative ionization efficiency, which is roughly in the ratio 7.6 : 2.2 : 1 for JP-10, CO_2, and H_2O.

In evaluating the potential for catalytic combustion, a useful measure of activity is the JP-10 decomposition probability per encounter with a CeO_2 particle. To extract this number from the breakdown versus temperature data (Figure 2.5), we need to estimate the number of encounters during passage through the hot zone, both with particles immobilized on the walls, and particles flowing in the gas stream. Experiments where the particle feed is interrupted, such as that shown in Figure 2.9, provide a direct measure of the relative importance of free vs. immobilized particles. While the CeO_2 is being fed, reactions can occur on both free and immobilized particles. Immediately after the particle feed is stopped, the reactivity of the immobilized particles is unchanged, but flowing particles are no longer present.

Therefore, the instantaneous change in the oxidation/total products ratio provides a direct measure of the relative importance of free and immobilized particles under our conditions.

Consider an interrupted feed experiment at 1150 K for JP-10 in helium, i.e., under conditions where the product distribution is exclusively hydrocarbons in absence of CeO_2, and predominantly oxidized species (CO_2, H_2O, H_2CO, etc.) when active CeO_2 is present (Figure 2.3, top frame). In this experiment, there was an immediate ~13 % drop in signal for oxidized products when particle feeding was interrupted, implying that reaction with CeO_2 immobilized on the walls generates ~8 times more products than reaction with free-flowing CeO_2.

The measured CeO_2 feed rate can also be used to crudely estimate the relative importance of immobilized and free-flowing particles, and this estimate is a useful check on our interpretation of the interrupted feed experiments. Recall that both the free and immobilized particles are micron scale aggregates of individual nanoparticles. The JP-10 mean free path between collisions is 10 - 50 microns under our conditions – larger than the average aggregate size (~5 microns), and much larger than the nanoscale structure of the aggregates. It is, therefore, not unreasonable to treat the aggregates as 5 micron spheres for the purpose of estimating JP-10 – aggregate encounter rates. The nanostructure undoubtedly affects the reaction efficiency/JP-10-aggregate encounter, however, this effect should be similar for free and immobilized aggregates. If we assume that the tube walls are completely CeO_2 coated, as suggested by visual examination, the encounter rate is simply controlled by the area of the tube inner surface, ~100 mm^2/cm length of tube. On the basis of our measured particle feed rate

(1.43 mg/sec) and the electron microscopy estimate of the average aggregate diameter of ~5 microns, we can estimate that the surface area of free aggregates (neglecting nanoscale structure) is about 17 mm^2 per centimeter of flow tube length. Crudely, therefore, the ratio of encounters with immobilized and free particles can be estimated to be ~6:1 − in fair agreement with the 8:1 estimate from the interrupted feed experiments. Because the estimate derived from those experiments is more direct, we will use it in all further analysis.

Figure 2.5 shows that for temperatures below 1000 K, there is substantially more JP-10 decomposition for flow tubes with CeO$_2$ or Fe$_2$O$_3$ coatings, than for identical gas mixtures without the active oxide (cf. JP-10/He with and without CeO$_2$). By subtracting the amounts of decomposition occurring with, and without active oxide present, we can derive the corrected fraction ($\Delta F_{survive}$) of JP-10 that survives N$_{col}$ collisions with active oxide in the flow tube hot zone. The decomposition probability per encounter with a CeO$_2$ or Fe$_2$O$_3$ surface (P$_{decomp}$) is related to $\Delta F_{survive}$ as follows:

$$\Delta F_{survive}(T) = (1 - P_{decomp}(T))^{N_{col}(T)}$$, where N$_{col}$ can be estimated from the JP-10 diffusion and flow properties (Table 2.1). This expression can be inverted to extract P$_{decomp}$(T), and the results are given in Table 2.2. Note that the N$_{col}$ numbers used in Table 2.2 are higher than those in Table 2.1, because they include a 15% correction for the effects of collisions with particles entrained in the gas stream.

Note that the P$_{decomp}$ values are all in a relatively narrow range, however, this simply reflects the fact that P$_{decomp}$ can be extracted for temperatures only where a significant fraction of the JP-10 survives.

Table 2.2 Probability of decomposition/JP-10 surface encounter.

JP-10/He on CeO_2

	620 K	800 K	920 K
JP-10-wall collisions	17.0	18.3	18.8
$\Delta F_{survive}$	0.954	0.823	0.792
P_{decomp} (%)	0.3	1.0	1.2

JP-10/He on Fe_2O_3

	620 K	800 K	920 K
JP-10-wall collisions	17.0	18.3	18.8
$\Delta F_{survive}$	1.00	1.00	0.896
P_{decomp} (%)	0.0	0.0	0.6

JP-10/O_2 on CeO_2

	620 K	800 K	920 K
JP-10-wall collisions	10.2	11.0	11.3
$\Delta F_{survive}$	0.912	0.761	0.833
P_{decomp} (%)	0.9	2.5	1.6

From our sensitivity limit for detecting JP-10 survival (~0.1%), we can only say that P_{decomp} is greater than ~30% by 1150 K for both Fe_2O_3 and CeO_2, with or without O_2. The more interesting point is that significant P_{decomp} values occur at substantially lower temperatures for CeO_2, with or without O_2, than for Fe_2O_3. As expected, the values of P_{decomp} increase with increasing temperature, with one exception. For the case of JP-10/O_2 with CeO_2, P_{decomp} apparently decreases between 800 and 920 K, however, this effect is attributed to an artifact of the method used to correct for background from pyrolysis. For JP-10/He, there is little decomposition in the temperature range up to 920 K, thus the correction is small. As discussed above, the lack of decomposition in this temperature range is attributed to formation of a passivating carbonaceous on the alumina walls. For JP-10/O_2, however, there is evidence that this passivating layer does not form (see above), thus the P_{decomp} values in for JP-10/O_2 with CeO_2 should be interpreted as the difference in decomposition between CeO_2 and unpassivated alumina. At 920 K, the results suggest that unpassivated alumina has significant activity for catalyzing JP-10 decomposition.

2.5   Conclusions

The mechanism for JP-10 decomposition, even in absence of catalyst, is poorly understood. Williams et al.[27] have developed a reduced JP-10 mechanism that is reasonably successful at modeling JP-10 combustion behavior. On the other hand, attempts to model the product speciation in JP-10 pyrolysis using the reduced mechanism were unsuccessful[19] even when the mechanism is augmented with additional reactions taken from a mechanism developed for a JP-8 surrogate fuel by Violi et al.[28] In particular, the mechanism predicts a strong bias towards C_2 products,

and is unable to replicate the C_5 and C_6 products observed in pyrolysis. Because the combustion mechanism is so complex, and is not completely understood even in absence of catalyst, we will focus this discussion on the effects of O_2, CeO_2 and/or Fe_2O_3 on the gross mechanism.

As discussed above, comparison of results for JP-10/He and JP-10/O_2 without catalyst, suggest that initiation is controlled by JP-10 pyrolysis even when O_2 is present, but that O_2 clearly accelerates decomposition once the temperature is high enough to initiate JP-10 breakdown. This result is not surprising. O_2 is a rather stable molecule, thus both energy and entropic factors favor initial rupture of JP-10 bonds. In contrast, from comparison of JP-10/He and JP-10/O_2 results with and without CeO_2, it is clear that in the presence of CeO_2, the initiation step does change, significantly lowering the onset temperature. In contrast, Fe_2O_3 results in little reduction of the onset temperature for JP-10 breakdown, although it is an efficient oxidizer at higher temperatures.

In the absence of O_2, CeO_2 clearly functions as an oxidizer, but when O_2 is also present the combustion reaction is clearly catalytic. Reaction with CeO_2 initiates the JP-10 breakdown process, and subsequent reaction with O_2 restores the CeO_2 oxidation state. It is also clear that CeO_2 not only initiates JP-10 decomposition, but also efficiently oxidizes the initial breakdown products, generating final products such as CO, CO_2, H_2O, and H_2CO. CeO_2 was chosen for this initial study based on low cost and ready availability of nanoparticles, however; the results suggest that other reducible oxides may also be active JP-10 combustion catalysts.

2.6   References

(1)   Burdette, G. W. Liquid hydrocarbon air breather fuel. In *U.S.*; (United States Dept. of the Navy, USA). US, 1983; pp 3 pp.

(2)   Antaki, P.; Williams, F. A. *Combust. Flame* 1987, *67*, 1.

(3)   Cho, S. Y.; Takahashi, F.; Dryer, F. L. *Combust. Sci. Technol.* 1989, *67*, 37.

(4)   Chung, H. S.; Chen, C. S. H.; Kremer, R. A.; Boulton, J. R.; Burdette, G. W. *Energy Fuels* 1999, *13*, 641.

(5)   Clausen, L. C.; Li, T. X.; Law, C. K. *J. Propul. Power* 1988, *4*, 217.

(6)   Guisinger, S. J.; Rippen, M. E. *Prepr. - Am. Chem. Soc., Div. Pet. Chem.* 1989, *34*, 885.

(7)   Peters, J. E.; Mellor, A. M. *J. Energy* 1982, *7*, 95.

(8)   Smith, N. K.; Good, W. D. *Aiaa J.* 1979, *17*, 905.

(9)   Szekely, G. A., Jr.; Faeth, G. M. *Combust. Flame* 1983, *49*, 255.

(10)   Takahashi, F.; Dryer, F. L.; Williams, F. A. *Symp. (Int.) Combust. [Proc.]* 1988, *21st.*, 1983.

(11)   Takahashi, F.; Heilweil, I. J.; Dryer, F. L. *Combust. Sci. Technol.* 1989, *65*, 151.

(12)   Wong, S. C.; Turns, S. R. *Chem. Phys. Processes Combust.* 1988, 97/1.

(13)   Wong, S. C.; Turns, S. R. *Combust. Sci. Technol.* 1989, *66*, 75.

(14)   Wong, S. C.; Lin, A. C. *Combust. Flame* 1992, *89*, 64.

(15)   Li, Z.; Anderson, S. L. *J. Phys. Chem. A* 1998, *102*, 9202.

(16)   Li, Z.; Eckwert, J.; Lapicki, A.; Anderson, S. L. *Int. J. Mass Spectrom. Ion Processes* 1997, *167/168*, 269.

(17)   Nakra, S.; Green, R. J.; Anderson, S. L. "Chemistry of JP-10 Relating to PDE Combustion and Diagnostics"; 15th ONR Propulsion Meeting, 2002, Washington, DC.

(18)   Li, Z.; Anderson, S. L. In *Adv. Chem. Propul.*, 2002; pp 61.

(19)   Nakra, S.; Green, R. J.; Anderson, S. L. *Combust. Flame* 2006, *144*, 662.

(20) Green, R. J.; Nakra, S.; Anderson, S. L. Thermal decomposition of JP-10 studied by microflow tube pyrolysis mass spectrometry. In *Combustion Processes in Propulsion*; Roy, G. D., Ed.; Butterworth Heinemann: London, 2005; pp 480.

(21) Li, Z.; Anderson, S. L. *J. Phys. Chem. A* 2003, *107*, 1162.

(22) Fedorova, M. S.; Denisov, Y. V.; Potapov, V. K. *Russ. J. Phys. Chem.* 1973, *47*, 1498.

(23) Stein, S. E., director. IR and Mass Spectra. In *NIST Chemistry WebBook, NIST Standard Reference Database Number 69*; Mallard, W. G., Linstrom, P. J., Eds.; NIST Mass Spec Data Center, National Institute of Standards and Technology: Gaithersburg MD 20899 (http://webbook.nist.gov). 2000.

(24) Flaim, T. A.; Ownby, P. D. *Journal of Vacuum Science and Technology* 1971, *8*, 661.

(25) Nishimura, H.; Tawara, H. *Journal of Physics B: Atomic, Molecular and Optical Physics* 1994, *27*, 4401.

(26) Lias, S. G.; Bartmess, J. E.; Liebman, J. F.; Holmes, J. L.; Levin, R. D.; Mallard, W. G. Ion Energetics Data. In *NIST Chemistry WebBook, NIST Standard Reference Database Number 69*; Mallard, W. G., Linstrom, P. J., Eds.; National Institute of Standards and Technology: Gaithersburg MD 20899 (http://webbook.nist.gov). 2000.

(27) Williams, S.; Bench, P. M.; Midey, A. J.; Arnold, S. T.; Viggiano, A. A.; Morris, R. A.; Maurice, L. Q.; Carter, C. D. "Detailed Ion Kinetic Mechanisms for Hydrocarbon/Air Combustion Chemistry"; Proceedings of the JANNAF 37th Combustion, 25th Airbreathing Propulsion,19th
Propulsion Systems Hazards, 1st Modeling and Simulation Subcommittees Joint Meeting, 2000, Naval Postgraduate School, Monterey, CA.

(28) Violi, A.; Yan, S.; Eddings, E. G.; Sarofim, A. F.; Granata, S.; Faravelli, T.; Ranzi, E. *Combustion Science & Technology* 2002, *174*, 399.

CHAPTER 3

OXIDE-FREE, CATALYST-COATED, FUEL-SOLUBLE, AIR-STABLE BORON NANOPOWDER AS COMBINED COMBUSTION CATALYST AND HIGH ENERGY DENSITY FUEL.

This chapter primarily consists of work that appeared previously in an article in the journal Energy & Fuels. Reproduced, in part, with permission from Brian Van Devener, Jesus Paulo L. Perez, Joseph Jankovich and Scott L. Anderson, Energy & Fuels, 23, 6111-6120, 2009. Copyright 2009, the American Chemical Society.

3.1 Overview

Elemental boron has one of the highest volumetric heats of combustion known, and is therefore of interest as a high energy density fuel. The fact that boron combustion is inherently a heterogeneous process makes rapid efficient combustion difficult. An obvious strategy is to increase the surface area/volume ratio by decreasing the particle size. This approach is limited by the fact that boron forms a ~0.5 nm thick native oxide layer, which not only inhibits combustion, but also consumes an increasing fraction of the particle mass as the size is decreased. Another strategy might be to coat the boron particles with a material (e.g., catalyst) to enhance combustion of either the boron itself, or of a hydrocarbon carrier fuel. We present a simple, scalable, one-step process for generating air-stable boron nanoparticles that are unoxidized, soluble in hydrocarbons, and coated with a combustion catalyst. Ball milling is used to produce ~50 nm particles, protected against room temperature oxidation by oleic acid functionalization, and optionally coated with catalyst. Scanning and transmission electron microscopy and dynamic light scattering (DLS) were used to investigate size distributions, with X-ray photoelectron spectroscopy (XPS) to probe the boron surface chemistry.

3.2 Introduction

The volumetric energy density of available fuels is a significant limitation on current liquid propulsion systems. JP-10, which has one of the highest energy densities of synthetic hydrocarbon fuels (just under 40 MJ/liter), has an energy content only about 15% higher than those of petroleum-based fuels such as JP-8 or JP-5 (34.2 MJ/liter). One approach to achieving higher volumetric energy density is

to load a liquid hydrocarbon fuel with particles of a high energy density solid, as a slurry or gel. Similarly, solid propellants are typically composed of a high energy density solid fuel and a solid oxidizer, held together with an organic binder material.

Boron and boron rich solids are interesting as high energy density materials, as they are the only practical materials with both volumetric (135.8 MJ/liter) and gravimetric (58.5 MJ/liter) energy densities that are substantially greater than those of hydrocarbons. Boron's potential as a fuel or fuel additive has not, to date, been realized, partly due to the difficulty in igniting and burning it efficiently.[1] One problem is that boron is quite refractory (T_{vap} = 2800 K), thus combustion is inherently a heterogeneous process, which tends to be slow and diffusion limited. The heterogeneous chemistry can, in principle, be accelerated by using nanoparticulate boron, leading to large surface-area-to-volume ratios, as suggested by a number of researchers.[2-5] The native oxide layer that forms on air-exposed boron surfaces limits this strategy, both by inhibiting combustion, and by reducing the energy density for small particles, due to the increasing fraction of the particle mass made up by the oxide layer. For example, Young et al.[5] recently reported that elemental boron made up only ~72 wt% of the boron nanoparticles (SB99 from SB Boron Corp) used in their combustion studies.

For many applications, efficient engine performance requires rapid fuel ignition and combustion that can be difficult to achieve for a complex hydrocarbon fuel. One approach to speeding up the kinetics is to add a fuel-soluble catalyst to the fuel.[6-8] For fuels loaded with high energy density particles, such a catalyst would tend to accelerate combustion of the hydrocarbon carrier fuel, thereby improving the

combustion efficiency of the solid particles. Using boron nanoparticles as a carrier for a combustion catalyst is, therefore, a possible strategy for simultaneously enhancing ignition of the hydrocarbon carrier fuel (or the binder in a solid propellant or explosive), and the total energy density. It is also possible that particles might be coated with a material that directly enhances boron ignition (via a thermite reaction, for example), or controls product speciation. In the case of boron combustion, it would be desirable to favor B_2O_3 rather than HOBO products.

Recently, we presented a brief description of a method to produce unoxidized, air-stable boron nanoparticles, protected by an organic ligand layer.[9] Here, we show that the same process can be used to generate particles partly coated with a functional solid material, which for this paper is a combustion catalyst. The preparation method is described in detail, including particle size distributions and a simple method to narrow them, detailed analyses of chemical compositions, and methodology to remove contaminants. In addition, we present data on the thickness and formation kinetics of boron's native oxide layer, which does not appear to have been reported previously.

Previous methods for boron nanoparticle production reported in the literature used methods such as gas-phase pyrolysis of diborane or multistep solution-phase synthesis routes.[2,10,11] Any practical preparation method for propulsion fuels must generate materials on large scales, and at low cost. Previous studies of coated boron, using materials such as glycidyl azide polymer (GAP)[12,13] have worked with particles that were already oxidized to some extent prior to coating. Another approach used prolonged exposure of boron particles to hydrocarbons at high

temperatures to create a boron carbide surface layer, however, XPS results showed that the surface layer was still substantially oxidized - with higher oxygen surface concentrations than in the boron feedstock.[14] The method we describe is based on high energy ball milling, and is simple, inexpensive, and easily scalable to large batches as needed. In a few hours, micron scale boron can be crushed to nano-scale powder, partially coated with a catalyst or other functional material, and rendered air-stable and hydrocarbon-soluble by an organic ligand coating. For this study, a CeO_2 (ceria) coating was applied, based on previous work showing it to be an effective catalyst for JP-10 ignition.[15] Ceria is also inexpensive and widely used for applications such as diesel pollution remediation.[16-18] By changing ligand and solid coating materials, the method should be applicable to a wide variety of materials and applications.

3.3 Experimental

3.3.1 Overview of milling process

Commercial boron powder (Sigma-Aldrich, nominal diameter 800 nm) was used as the feedstock for milling. In large scale production, coarser and less expensive boron powder could be used, with the result that longer milling times, or possibly a two-step milling process would be required. A Spex-CertiPrep® 8000M mixer mill was used, with either stainless steel or tungsten carbide milling jar and 1/8'' diameter balls of the same material as the jar. As expected, the tungsten carbide milling balls and jar resulted in faster size reduction than stainless steel equivalents, which were used in a few studies, primarily to determine the source of some contaminants. Higher efficiency for denser media has been discussed

previously,[19] and for hard materials such as boron, the high hardness of WC presumably helps with both milling speed and in resisting abrasion.

The milling jars have ~37 cm^3 internal volume, and the charge ratio (ratio of ball to powder mass) was kept high (~80:1) to minimize the time required for milling to the nanoscale. The milling jars were modified from the stock geometry to eliminate corners and cracks at the seals where powder might be inaccessible to the milling balls. The boron powder and other constituents were sealed into the milling jars in a nitrogen atmosphere, and the jars were also opened after milling and the contents removed and stored in nitrogen. No evidence of boron nitride formation was observed (see below).

Several milling approaches were examined. Dry-milled samples were produced with only boron powder and milling balls loaded into the jar. Wet-milled samples were milled with addition of a wetting agent (hexanes or JP-5 jet fuel) to help disperse the powder and prevent caking. In most experiments, a small amount of oleic acid or other ligand was added to the wetting agent, resulting in ligand-protected particles. Table 3.1 lists the composition of the milling loads and total milling times for typical runs.

Since we are interested in preparing air-stable materials, in most experiments the nanopowder, milled in N_2, was brought into contact with air prior to analysis. It should be emphasized that caution must be exercised when exposing freshly milled, unpassivated boron nanoparticles to air - small particles can be pyrophoric, i.e., air oxidation can lead to thermal runaway and particle ignition. We have observed auto-ignition of dry, sub-50 nm particles in air. Ligand-protected particles are air-stable,

Table 3.1 Summary of milling conditions.

	milling conditions				
	dry	wet	wet w/ oleic	w/ceria	w/ceria and oleic
milling time (hrs)	6	3	3	6	3
boron loading (g)	2	2	2	2	2
oleic loading (ml)	-	-	1	-	1
ceria loading (g)	-	-	-	0.1	0.1

as shown below, but for safety we treat *all* milling products as potentially pyrophoric when first exposed to air. Our procedure is to expose the particles to slowly increasing oxygen concentrations, and eventually pure oxygen, to guarantee that they are air-stable. For wet-milled samples, this is done by bubbling a variable N_2/O_2 mixture through a suspension of the particles in hexanes. Some dry-milled particles were treated this way as well, and some were exposed dry. It should also be noted that the toxicity of such nanoparticles is unknown, therefore, particles and particle suspensions are handled with gloves and other protective gear, and dry particles are handled in an exhaust hood.

3.3.2 Dry milling

A few experiments were done using dry milling. Two g of boron powder were loaded along with 160 g of milling balls. Under the conditions of our mill, severe caking of the boron powder was observed, and dry milling required ~6 h milling in order to reach the 50 - 100 nm size range. The one advantage of dry milling seemed to be that the contaminant level was low (see below), probably because the powder tended to coat the milling surfaces, reducing wear.[20] Certainly we observed that after dry-milling, it was quite difficult to remove all the boron caked onto surfaces of the jar and balls.

3.3.3 Wet milling

Most particle production was carried out wet, with ~15 ml of either hexanes or JP-5 jet fuel added to the milling jar, along with 2 g of boron and 160 g of milling balls. Wet milling prevents caking of the milled powder, makes sample recovery

and clean-up easier, and reduces the milling time for a given particle size by about ~50 %. The drawback to wet milling is that it increases the contaminant level (see below) in the milled products, apparently because of enhanced wear of the milling surfaces by the relatively abrasive boron powder.

To generate ligand-protected, hydrocarbon-soluble nanoparticles, 1 mL of oleic acid ($CH_3(CH_2)_7CH=CH(CH_2)_7COOH$ - Sigma-Aldrich) was added to the wet-milling mixture prior to milling. The idea is that as fresh boron surfaces are generated by milling, they react with the carboxylic acid end of the ligand forming B-O-C bonds, resulting in particles with C_{18} hydrocarbon tails extending out from the surface. Some initial experiments were carried out using sodium dodecyl sulfate (SDS) as the coating ligand, with similar results. Oleic acid was chosen for most experiments because sulfur in fuels is a pollution source, and because excess detergent surfactant might interfere with demulsifying ship-board fuels.

To insure complete coating of the boron surfaces, the amount of oleic acid added was in excess of what we estimate would be required to form a monolayer coating on the surfaces of the nanoparticles. For fuel uses, this small excess of oleic acid is probably not significant; however, it is easily removed by a simple washing procedure.[9] Briefly, after allowing the hexane wetting agent to evaporate, the nanoparticle/oleic acid paste was dispersed in reagent grade methanol (Mallinckrodt, 99.9%), then centrifuged to separate the boron particles from excess oleic acid which is quite soluble in methanol. The covalently bonded ligand layer remains attached to the boron particles, which can be re-suspended/dissolved in hydrocarbon solvent or JP fuel if desired.

3.3.4 CeO₂ Coated Particles

To generate ceria-coated particles, a two-step process was used. In the first step, 2 g boron and 0.1 g CeO₂ (Nano-Scale Materials Inc., 120 nm diameter) were dry milled with 160 g of WC balls for 30 min, to allow the two solids to interact without intervening ligand or wetting agent. As shown below, this results in bonding of the ceria to the boron surfaces. After this initial dry phase, the jar was opened in a N₂ atmosphere, and 15 ml of hexanes and 1 ml of oleic acid were added. The sample was then wet milled for an additional 2.5 h, followed by the same work-up as in the wet milling process as described above.

3.3.5 X-ray Photoelectron Spectroscopy (XPS)

Characterization of particle surfaces was carried out using XPS, in ultra-high vacuum. For wet-milled samples, a few drops of hydrocarbon solution/suspension of the milled particles were pipetted onto a stainless steel shim and allowed to evaporate, leaving behind dry boron powder. The process was repeated until a continuous coating was obtained. A continuous coating is important so as not to detect any photoelectrons from elements present in the underlying stainless steel. Visual inspection under a light microscope was used to examine the coverage, and complete coverage was verified by the absence of photoelectron peaks from Fe, Cr, and Ni. (Samples milled with stainless steel jars and/or balls showed some contamination from abraded steel, as discussed below) The coated shims were dried in a vacuum oven at 70° C at a few Torr pressure for 2 h to evaporate any remaining volatile hydrocarbons. For samples that were milled with oleic acid, the drying time was increased to 12 or more h, to drive off any excess oleic acid that remained after

the methanol washing process. Aside from a few experiments where samples were transferred in inert atmosphere, all samples were exposed to the ambient atmosphere at temperatures up to 70° C prior to XPS analysis.

X-ray photoelectron spectra were collected using the monochromatic Al Kα source (1486.7 eV) on a Kratos Axis Ultra DLD instrument, using a 300 x 700 micron spot size. Both low resolution survey scans, and high resolution scans of energy ranges of interest were done. Significant charging was seen for all samples, resulting in peak shifts and broadening. The peak widths were minimized by flooding the sample with low-energy electrons and ions from the charge neutralizer system, however, there is still ambiguity regarding the absolute peak positions. A common approach to determining the absolute energy shift is to reference the spectra to the C 1s peak from adventitious carbon. For these samples, some of which have sp^2, sp^3 and carboxylic carbon from oleic acid, this approach is also ambiguous. To provide an absolute energy reference, a small concentration of argon atoms was implanted into the sample using 1 keV Ar^+. The positions of the XPS peaks of interest were then corrected using the shift observed (typically around 0.7 eV) for the Ar 2p peak, relative to its literature value (241.8 eV).[21] The energy corrections estimated by reference to implanted Ar and adventitious carbon differed by no more than 0.4 eV, and were nearly constant for all samples. This discrepancy is not large enough to introduce any ambiguity in peak identification.

3.3.6 Size characterization

Particle size and morphology information was obtained using a combination of dynamic light scattering (DLS), scanning electron microscopy (SEM),

transmission electron microscopy (TEM), and scanning transmission electron microscopy (STEM) with energy dispersive X-ray analysis (EDX). For DLS, a Particle Sizing Systems NICOMP 380 was used, and the particles were suspended in hexane solvent (viscosity = 0.294 CP, index of refraction 1.375 at 25° C). SEM images were obtained on a FEI Nova Nano 600 operated at 20 kV beam energy. Samples for SEM were washed in methanol and centrifuged as described above, re-dispersed in hexanes by ultra-sonication, pipetted onto aluminum stubs, and dried for analysis. TEM was performed on an FEI Technai F30 operated at 300 keV beam energy, with particles dispersed on ultrathin holey carbon film 400 mesh copper TEM grids. STEM/EDX analysis was carried out using a FEI Technai F20 operated at 200 keV and equipped with a high angle annular dark field detector (HAADF) and an EDAX® spectrometer.

3.4 Results and Discussion

3.4.1 Size distributions of boron powders

Figure 3.1 shows four representative SEM images of boron: unmilled, dry-milled, wet-milled in hexanes, and wet-milled in hexanes with oleic acid surfactant, in each case using WC jar and balls. The dry-milled powder was milled for 6 h, while the wet-milled samples were run for only 3 h due to more efficient milling. All images were collected under the same conditions at 50,000 times magnification. It can be seen that the large sharp edged particles in the unmilled sample are reduced in size and have more rounded shapes. The primary particles in the unmilled sample appear to be mostly in the 500 – 2000 nm range. For all milled samples, the size distributions are dominated by primary particles in the sub-150 nm
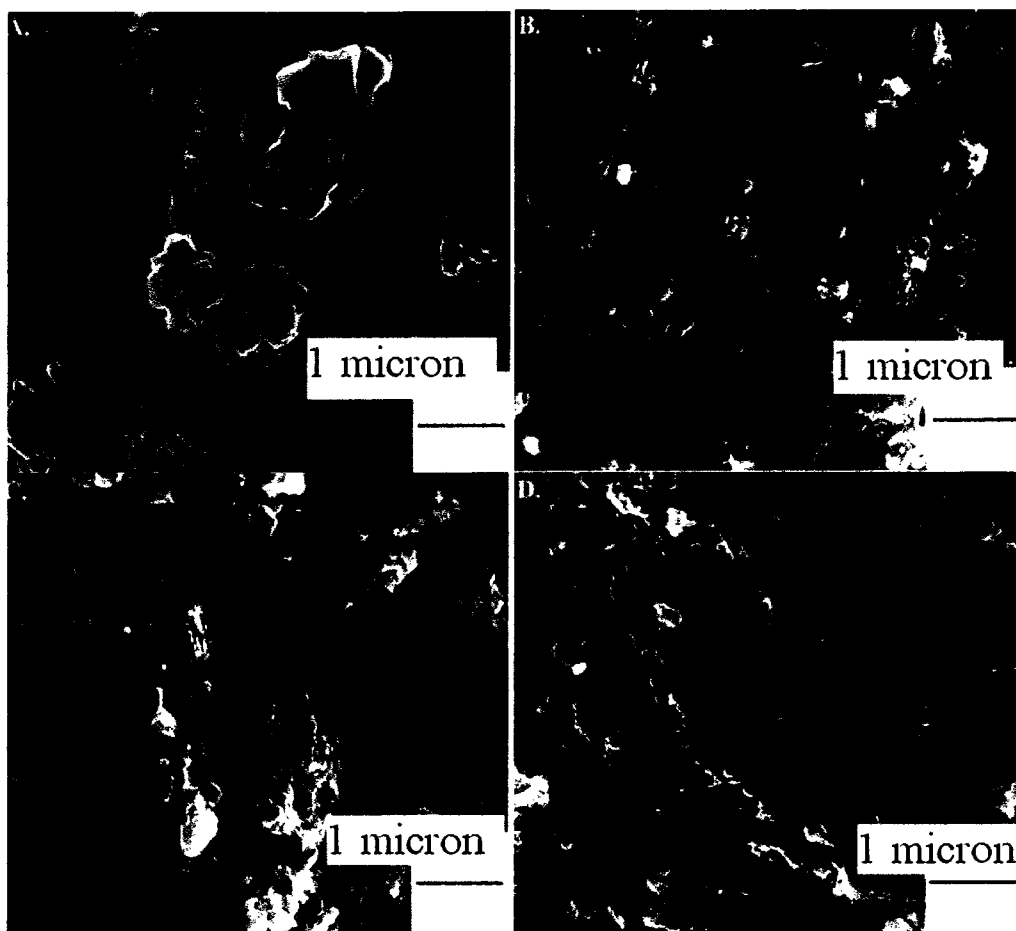
Figure 3.1 SEM images at 50 k times magnification, 1 μm scale bar. (a) Unmilled

boron feedstock; (b) dry milled boron; (c) wet milled boron in hexanes; (d) wet

milled boron with oleic acid surfactant.

size range, but the appearance of the samples is quite different. The sample milled in hexanes with oleic acid appears to have a narrower distribution of primary particle sizes, and the aggregates look smoother. Because of extensive aggregation during drying for SEM analysis, it is difficult to estimate the primary particle size distributions, or to distinguish between aggregates that might have been present in the sample and those that form upon drying.

For the oleic acid-functionalized samples, the particles are readily suspended in hydrocarbons, thus the size distributions could also be probed by DLS. We were unable to produce suspensions of un-functionalized particles that were stable enough to allow DLS analysis. For DLS, the methanol-washed, centrifuged samples were re-suspended in hexane by ultra-sonication prior to analysis. Figure 3.2 shows normalized histogram plots of the number- and mass-weighted size distributions. The number-weighed distribution (top frame) is dominated by sub-100 nm particles, however, there is a peak around 600 nm that is visible if the scale is magnified. Because mass scales with d^3, these large particles make up nearly half the mass-weighted distribution (bottom frame). The question is whether these large particles are simply boron feedstock that somehow missed getting broken down in milling, or if they are aggregates of smaller particles that simply did not get completely dispersed during the ultrasonic re-suspension used to prepare the DLS samples.

The latter interpretation is suggested by experiments where the milling time was increased from the 3 h used for most wet milling experiments. Longer milling times were found to slightly increase the fraction of the mass distribution in the sub-100 nm range, but at the same time, the size distribution of the large particles
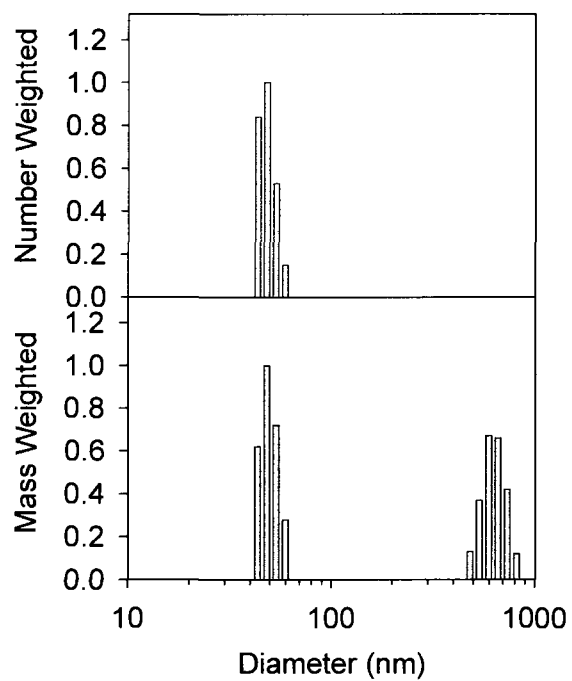
Figure 3.2 DLS results oleic acid capped boron. (Top) Number weighted, (bottom) mass weighted.

increased to 1 μm or more. This result suggests that milling can build stable aggregates by cold-welding small particles together, as suggested by Suryanarayana et al. for a variety of milled materials, including: iron, aluminum and silicon.[20]

Regardless of the nature of the large particles, they can be removed easily by sedimentation, either by centrifuging the suspension for 15 min, or by simply allowing it to stand undisturbed for a week or two. Figure 3.3 shows the size distribution obtained after centrifuging the suspension, then analyzing the supernatant fluid. Note that the large particles are all gone, but the size distribution of sub-100 nm particles is similar to that in the original suspension. Once the large particles have sedimented out, the supernatant is stable (for > 6 mo. at the time of writing). When we refer to particle "solutions," we are referring to these stable suspensions of these sub-100 nm particles. When the small particles are dried and re-suspended in JP-5, the resulting solutions are also stable on at least a 6 mo. time scale. For large scale production of boron particles, one would presumably mill using fuel as the wetting agent, and then sediment out the large particles for further milling, to avoid waste of the boron feedstock.

We also carried out SEM of the small particles remaining in the supernatant after centrifugation. The primary particles still aggregate extensively when dried for SEM analysis, but the size distribution is consistent with the DLS results - only sub-100 nm primary particles are observed, and most of the particles are in the 40 - 60 nm size range.[9]

In summary, milling with subsequent sedimentation to remove large aggregates, produces a narrow distribution of boron particle sizes between 40 and 60
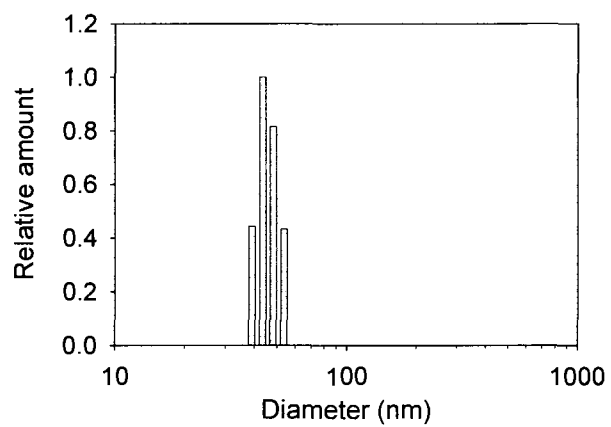
Figure 3.3 DLS results from oleic acid capped boron following separation.

nm in diameter. The particle shapes are irregular, but with rounded edges. The oleic acid functionalized particles are soluble, i.e., form stable suspensions, in hydrocarbon solvents such as hexane, and in hydrocarbon fuels such as JP-5, which are complex mixtures, but contain substantial fractions of alkanes and alkenes that presumably interact with the hydrocarbon tails of the oleic acid coating.

3.4.2 Surface analysis of boron powders

The surface composition and chemical state was probed by XPS, and the composition results are summarized in Table 3.2. It is important to note that XPS is sensitive only to the top ~8-10 nm of the sample surface, and thus probes surface, rather than bulk composition. All samples were deposited on the XPS sample holder from hexane suspension, then dried. The samples were analyzed as prepared, and after 1 and 6 min of sputtering by a 4 keV Ar^+ beam rastered across a 2x2mm region of the surface, centered about the much smaller analysis area. The photoelectron peak used in quantitation is listed in the left hand column, with atomic composition data shown before and after Ar^+ sputter treatment. Sputtering removes material from the top surface of the sample, and thus provides some insight into how composition varies with depth.

The atomic concentrations listed were determined from the standard equation:

$$C_x = \frac{I_x/S_x}{\sum I_i/S_i}$$

where C_x is the atomic fraction of a given elemental constituent in a particular sample, I_x is the intensity of the corresponding photoelectron peak, and S_x is the atomic sensitivity factor for that peak in the Kratos instrument. This analysis

Table 3.2 Summary of surface atomic compositions, boron powders.

PE pk	surface atomic composition (%)											
	unmilled boron sputter time (s)			dry milled sputter time (s)			wet milled sputter time (s)			milled w/oleic sputter time (s)		
	0	60	360	0	60	360	0	60	360	0	60	360
B 1s	70.8	78.4	81.2	74.4	78.6	80.2	52.6	60.4	64.0	31.2	35.1	49.7
O 1s	11.7	9.5	8.7	12.6	10.1	8.8	29.3	23.4	20.0	13.4	9.0	5.6
C 1s	11.9	8.0	6.5	9.7	7.2	7.0	15.3	12.4	11.6	53.1	53.2	41.0
W4f	-	-	-	0.4	0.4	0.7	0.7	1.1	1.9	0.5	0.8	1.2
Co2p	-	-	-	0.4	0.5	0.6	0.7	0.8	1.2	0.2	0.1	0.1
Fe2p	-	-	-	0.1	0.2	0.2	0.2	0.3	0.3	0.2	0.2	0.2
N 1s	2.0	1.2	0.8	2.1	1.9	1.7	0.7	0.7	-	0.4	0.4	0.4
F 1s	2.2	1.4	0.9	0.2	0.1	-	0.5	-	-	0.2	-	-
K 2s	1.2	0.8	0.6	-	-	-	-	-	-	-	-	-
Ar2p	-	0.6	1.1	-	0.9	0.9	-	0.9	1.1	-	0.3	1.0
Si2s	-	-	-	-	-	-	-	-	-	0.3	0.8	0.7
Na1s	-	-	-	-	-	-	-	-	-	0.3	0.1	0.1

assumes that the samples are flat and homogeneous over the depth range sampled by XPS (~10 nm), which is obviously not true for our samples, consisting of aggregates of boron nanoparticles coated with boron oxide, oleic acid, or other materials. A more detailed quantitation model aimed at estimating the oxide layer thickness is described below, however, the simple homogeneous model provides a useful starting point for comparing the different samples.

The unmilled boron spectrum (particle size ~ 800 nm) is dominated by signal from boron, with oxygen, carbon, and various minor contaminants that decrease as the surface is sputtered (the exception is Ar, which increases as more Ar is implanted). The implication is that the unmilled particles have a boron core, coated by a thin layer consisting of boron oxide and adventitious carbonaceous contaminant, as expected for a sample exposed to the ambient environment. For a flat boron surface, the contaminants would sputter away completely, leaving essentially pure boron. For a powdered sample, however, the oxide and other contaminants are interspersed between particles throughout the sample. There is an initial decrease as the top surface is sputtered clean, but the contaminant level remains high because additional contaminants are exposed as the top layer particles erode away.

Dry milled particles (particle size ~50 nm) are expected to be similar to the unmilled boron, because the particle size (~40 - 200 nm (Figure 3.1)) is considerably larger than the XPS sampling depth. This is essentially what we observe, with the exception of the appearance of low levels of W, Co, and Fe. The W and Co clearly come from the Co-cemented tungsten carbide milling jar and balls, and the Fe

appears to result from iron impurities in the WC. To verify that the WC jar and balls were the source of the Fe contaminant, rather than the hexanes, we performed XPS on two sets of dry milled powders; those that were washed with hexanes and those that were not. The level of Fe contamination was identical.

Such metal contaminants could be undesirable in a fuel system because they might catalyze undesired reactions. The distribution of these metals in the sample was probed by SEM/EDX (energy-dispersive x-ray fluorescence), and it turns out that nearly all the contamination is in the form of a small number of rather large (~200-800 nm) WC particles that were apparently spalled off the WC balls or jar. Because Co-cemented WC is strongly magnetic, it is simple to remove. The particles were suspended in hydrocarbon (hexane or JP-5), then "cleaned" by simply stirring the liquid using a magnetic stir bar. The magnet was periodically removed, wiped clean with a lint free cloth, and the process was repeated until the magnet appeared clean under visual inspection. XPS analysis of magnetically cleaned samples showed that total W/Co/Fe contamination was reduced to undetectable levels in most samples, and to <1% even for the most heavily contaminated materials.

For the boron wet milled in hexanes, the initial fraction of boron is considerably reduced, and the C and O concentrations are significantly enhanced, compared to dry milled boron. With sputtering, the C and O concentrations decrease and B increases, but even after sputtering to steady state, the C and O concentrations are higher than in the dry-milled material. This might be taken as evidence that wet milling leads to additional oxidation, or possibly formation of a boron carbide on the

particle surfaces, but as shown below, high resolution B XPS shows no boron carbide. We believe that the additional carbon and some of the oxygen originates in contaminants in the hexanes, which are left behind as a non-volatile residue when the solvent is evaporated to generate the XPS samples. The hexanes have a stated purity of 99.9% with 0.1% of nonvolatiles; however, because XPS is surface-sensitive, it is highly sensitive to contaminants that deposit on the surface as the samples dry. We verified that evaporating hexanes does leave a carbonaceous residue by comparing XPS of clean stainless steel surfaces with and without hexanes evaporated on them, and there clearly is a significant increase in nonvolatile carbon for the spot with evaporated hexanes. The important point is that in a fuels application, this carbonaceous contaminant would be insignificant – it is seen in XPS only because the impurities concentrate on the surface, and XPS is surface-sensitive. Some fraction of the "extra" oxygen concentration for the wet-milled boron sample may also originate from oxygenated compounds in the nonvolatile residue, however, the high resolution boron XPS, discussed below, shows that the boron is more highly oxidized in the wet-milled samples.

For boron milled in hexanes with oleic acid (methanol washed to remove excess oleic acid), the C concentration in the near-surface region is over 50%. This is expected because a self-assembled monolayer of oleic acid (18 carbon chain) would be ~2 nm thick, producing a high signal for C 1s photoelectrons. In addition, the oleic acid overlayer attenuates signal from the underlying boron by about 40%: $I = I_0 exp(-t/EAL)$, where I is the detected boron photoelectron signal, I_0 is the boron photoelectron signal that would be detected with no overlayer, t is the ~2nm

overlayer thickness, EAL is the effective attenuation length for B 1s photoelectrons in a hydrocarbon film (~3.7 nm[22]). Note that there are small concentrations of Si and Na, attributed to contaminants in either the oleic acid or the methanol used to wash out the excess acid (both reagent grade), again demonstrating the high sensitivity of XPS to contaminants that deposit on the sample surface during evaporation.

Figure 3.4 shows the boron 1s region of the photoelectron spectra for each sample, after background subtraction using the Shirley algorithm.[23] There are clearly several components present in the spectra, corresponding to different chemical states of boron. To determine intensity ratios, the spectra were fit to Gaussian/Lorentzian type functions using the program XPSPEAK, and the results are shown as smooth curves for each fit component, and for the total fit. Peak parameters were constrained to values found from fitting spectra obtained for planar solid boron surfaces (see below). The small fitting errors on the high binding energy side of the primary peaks (~188-190 eV) are attributed to differential charging of the powder samples. Most of the intensity in all four samples can be fit by the same two components. The most intense peak for all samples (188.0 eV) is assigned to elemental boron (zero oxidation state – B^0) in the core of the particles. The first three samples also show a clear peak at ~193 eV in good agreement with the literature value for B_2O_3 (193 eV[24]), thus this peak is identified as fully oxidized boron (B^{3+}), in an oxide layer on the boron particle surface.

For the final sample, wet-milled with oleic acid, this oxide peak is absent, at least at the sensitivity level of XPS. From the fuels perspective, this is the critical point - wet-milling with oleic acid produces boron nanoparticles that are air-stable
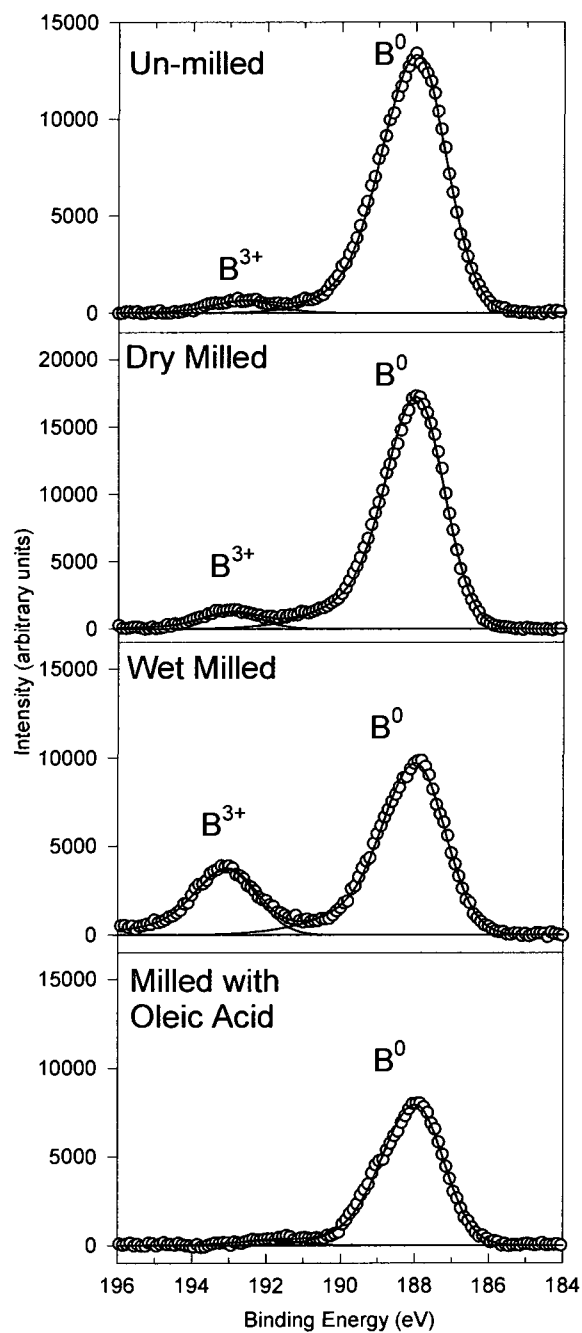
Figure 3.4 B 1s XPS regional spectra for unmilled, dry milled, wet milled, and

milled with oleic acid.

and free of the normal B_2O_3 layer, at least within the sensitivity of XPS (~2 - 3 % of a monolayer). There is a small component around 192 eV, however, suggesting the presence of a small fraction of boron with oxidation state intermediate between B^0 and B^{3+}. This intensity is taken as evidence that the oleic acid is anchored by covalent B-O-C bonds between the boron surface and the carboxylic acid head group. Such bonding would leave boron only partially oxidized. Note also that the overall intensity for this sample is ~50% lower than that for the dry-milled boron. This attenuation is in reasonable agreement with that estimated above (40%) for a single monolayer of oleic acid on the boron surface, providing additional confirmation that the oleic acid is coating the boron surface.

3.4.3 Ceria Coated Boron Particles

The size distributions for boron milled with ceria, as determined by DLS, are essentially identical to those obtained without ceria, under the same milling conditions (see Appendix A). Here, we focus on the coating morphology and chemical state of the ceria and boron in these samples, as these are the catalytically important properties.

3.4.4 XPS Results for Boron Milled with Ceria

Figure 3.5 shows the B 1s spectrum taken from boron powder that was milled dry with ceria. We also obtained data for wet-milled B/ceria samples that were functionalized with oleic acid (see Appendix A), however, the oleic acid coating attenuates the signal significantly, and it is easier to see the smaller features in the dry-milled sample. If we constrain the fit component peak shapes, as
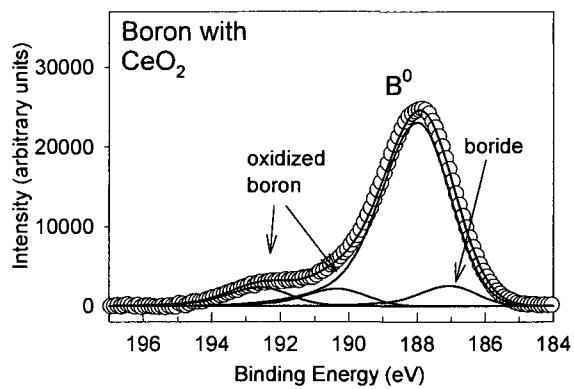
Figure 3.5 B 1s XPS spectrum for boron milled with ceria.

above, it is necessary to use four components peaking at 187.2, 188.0, 190.3, and 192.6 eV to obtain a reasonable fit. The main component (188.0) is clearly B^0 from the particle core. The peak at 192.6 is assigned to B^{3+} in the oxide layer. The component at 190.3 eV may represent some slightly oxidized boron formed at the ceria-boron interface, but it might also be an artifact of differential charging of the ceria-coated particles. The most interesting feature is the asymmetric broadening to low binding energy of the main peak, compared to that in boron dry milled without ceria. This feature was fit well by adding a small peak at 187.2 eV. It is possible that this component also results from differential charging, which can induce peak asymmetry;[25] however this effect was only seen for samples milled with CeO_2, despite significant charging for all samples. The other possibility is formation of a cerium-boride, i.e., chemical interaction at the ceria-boron interface. Cerium forms stable borides, with the most common stoichiometries being CeB_4 and CeB_6.[26] Such borides result in XPS peaks that are typically shifted between about 1.8 and 0.1 eV to lower binding energy, compared to B^0.[27] The only other boron compounds with B XPS peaks shifted to lower binding energies are species such as boranes and $NaBH_4$ which would not be expected to form under our milling conditions. Considering that the low binding energy feature is only seen for samples where where boron was milled with ceria, we tentatively assign it to formation of some $B_xCe_yO_z$ compound at the boron-ceria interface. The important point here is that the XPS provides evidence that the ceria is chemically bonded to the boron particle surfaces.

3.4.5 STEM/EDX anaylsis of ceria-coated boron nanoparticles

Further morphology information was obtained through small spot EDX analysis coupled with STEM/HAADF images. Figure 3.6 shows a STEM image of a typical ~50 nm primary (i.e., nonaggregated) particle produced by dry-milling of boron with as-received ceria for 6 h, as discussed above. To avoid sample bias, several particles were analyzed with similar results. An example of one such particle is presented in Appendix A. Superimposed on the image are a rectangle and two circles that indicate areas probed for the EDX atomic composition analysis summarized in Table 3.3. The particles in this sample typically have brighter and darker patches randomly distributed over their surfaces. With the HAADF detector, brighter areas in the images correspond to regions that are either thicker, or that contain higher concentrations of high Z elements (Ce). The first column ("area A") shows analysis over the large rectangular area, covering much of the particle surface, and taking in a cluster of large bright spots near the center. Boron, oxygen, and cerium are present, along with copper and a large amount of carbon. All of the copper, and most of the carbon, results from the Cu-supported carbon TEM grid that the particles are deposited on. Analysis of "area B," which is centered on a bright patch on the particle, shows somewhat higher Ce concentration than in the large area, but "area C", which focuses on a dim area in the image, is almost free of Ce. These results show that the bright areas covering the surface are Ce-rich, and dim areas are essentially Ce-free boron, with roughly 20% of the particle surface coated (a transmission image shows a projection of bright areas on both the top and bottom surfaces of the particles).
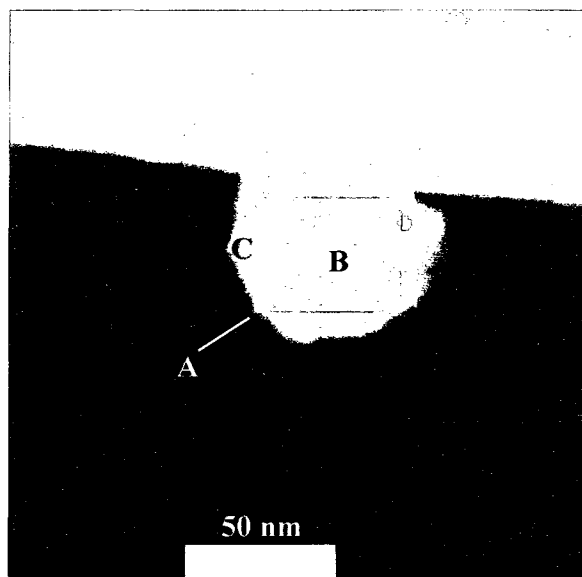
Figure 3.6 STEM/HAADF image of ceria coated boron particle.

Table 3.3 EDX results boron milled with ceria.

	EDX atomic composition							
	area A			area B			area C	
element	at %	wt %	element	at %	wt %	element	at %	wt %
B	27.8	23.0	B	30.4	26.1	B	37.4	33.0
Ce	0.2	1.8	Ce	0.2	2.1	Ce	0.0	0.3
O	4.8	5.8	O	2.5	3.2	O	1.1	1.5
C	65.4	60.3	C	65.7	62.7	C	60.2	59.0
Cu	1.9	9.0	Cu	1.2	5.9	Cu	1.2	6.2

An uneven coating of ceria on the boron particle surfaces is expected. The boron particles are rough, and the milling process would not be expected to generate a uniform coating. In fact, for a fuel application, such a partial coating is probably desirable, because a complete coating of ceria on the boron surface would tend to inhibit ignition/combustion of the boron.

3.4.6 Formation and thickness of the boron native oxide layer

The native oxide layer that coats and passivates boron exposed to air is critical in boron combustion, but the properties and formation of this oxide layer under ambient conditions have apparently not been reported previously. Trenary and co-workers reported a detailed study of the reactivity of clean, crystalline boron (β rhombohedral boron (111)) with oxygen under ultra-high vacuum conditions, however the oxygen exposures were too small to allow development of the self-limiting native oxide layer.[28] The same group also studied oxidation of boron films grown on a TaB_2, surface, and observed growth of a B_2O_3-like oxide, but the maximum O_2 exposure studied (equivalent to ~0.05 Torr-seconds) was still not sufficient to saturate the oxidation process.[29] Therefore, we also studied formation of the oxide both on nanoparticles and on a flat surface of bulk boron.

3.4.7 Planar boron surfaces

Two small pieces of boron (~3 x 2 x 1 mm) were prepared for surface analysis. One sample had been exposed to ambient air for years, and we prepared a "clean" surface on the other sample by cleaving the sample just prior to introduction into the load lock chamber of the XPS instrument. The time that the "freshly

cleaved" surface was exposed to atmospheric pressure was on the order of a few minutes as this was the minimum amount of time needed to mount the sample for analysis after cleavage.

Figure 3.7 shows the B 1s spectra of the two samples. The dominant peak in both samples is assigned to B^0 with the smaller peak identified as B^{3+} in B_2O_3. As with the earlier spectra, a Shirley type background was subtracted, then the peaks were fit using Gaussian/Lorentzian type functions. For these fits, the widths of the B^0 and B^{3+} peaks were allowed to vary, and those widths were used in fitting the powder samples, discussed above. Clearly the extent of oxidation for both samples is similar. The B^0/B^{3+} ratio for the sample exposed to ambient conditions for years (uncleaved) was 21.6, compared to 28.8 for the cleaved sample. The fact that the ratio is slightly larger for the cleaved sample suggests that the initial oxide layer growth is rapid, but that formation of the fully self-limited native oxide layer takes more than a few minutes.

To determine the thickness of the oxide layer from the B^0/B^{3+} intensity ratios, we modeled the XPS process, assuming that the samples consist of a uniform B_2O_3 coating on top of a thick piece of flat elemental boron solid. The "flat layered" model described in Appendix A, along with EAL data from the NIST database,[22] was used to determine the oxide layer thickness that best fits the B^0/B^{3+} intensity ratios. The result is that the oxide layer on the sample exposed for years is 0.5 nm, while the sample exposed for only a few minutes has an oxide thickness of 0.4 nm. Clearly, oxidation is quite fast, with the oxide layer thickening to ~80% of the limiting native oxide thickness in just a few minutes. The obvious implication is that
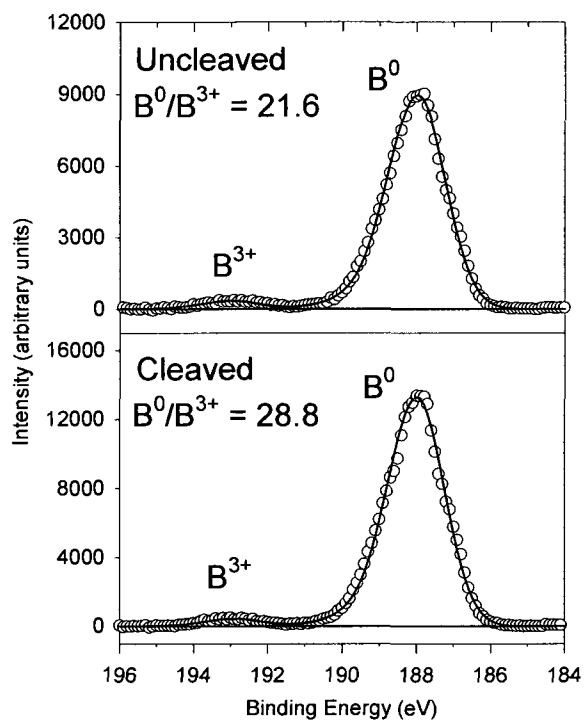
Figure 3.7 B 1s XPS spectra from planar boron surfaces.

any strategy to avoid oxide formation must passivate the surfaces before any significant oxygen exposure occurs.

3.4.8 Oxide formation on nanoparticles

As shown in Figure 3.4, the oleic-acid functionalized nanoparticles are essentially free of any B_2O_3 layer, within the sensitivity of XPS. The unmilled boron has a B^0/B^{3+} intensity ratio similar to that for flat, bulk boron (Figure 3.7), and use of the "flat layered" model results in a 0.5 nm oxide layer. This similarity to flat bulk boron is expected because the unmilled boron particles are ~100 times larger than the 8-10 nm probe depth of XPS, and therefore should look flat to XPS.

Clearly, however, the dry-milled, and especially the wet-milled boron has substantially more XPS-visible oxide. A likely cause of the greater apparent degree of oxidation is the morphology of the nanopowder, and there are two major effects expected.

For smooth particles with a thin oxide overlayer, the curvature of the particle surface results in an increase in the XPS signal from the overlayer, because of the variation in take-off angle, i.e., the angle between the *local* surface normal and the XPS detection direction ("take-off" angle). As noted above, photoelectron intensity from the underlying boron particle core is attenuated by passage through the oxide overlayer: $I = I_0 \exp(-t/EAL)$. For flat surfaces oriented with zero take-off angle, i.e., with the surface normal along the XPS detection direction, t is simply the overlayer thickness. For a surface with take-off angle θ, the photoelectrons from the boron core must penetrate through oxide for a distance $t/\cos\theta$, resulting in additional attenuation of the B^0 signal. Because the oxide layer has a greater effective

thickness along the detection direction, there is also additional B^{3+} signal, resulting in a significant drop in B^0/B^{3+} intensity ratio that gives the appearance of a thicker oxide coating. For example, if the dry-milled sample is modeled assuming a flat surface (flat layered model, Appendix A), the best fit oxide layer thickness is 0.7 nm, compared to 0.4 nm for the cleaved, flat boron sample.

This geometric effect has been simulated using a "random packed spheres" model described in Appendix A. In essence, the sample (a thick layer of nanoparticles) was modeled by a collection of randomly packed spheres with variable diameter (set to 50 nm), each coated with a uniform oxide layer of adjustable thickness. Of course the actual particles are not spherical; however, a collection of randomly oriented angular nanoparticles should give a distribution of take-off angles similar to that of spherical particles. The oxide layer thickness that best fits the dry-milled data with this model is 0.4 nm -- identical to that seen for the cleaved, flat boron sample. Therefore, we attribute the greater B^{3+} intensity seen in XPS of dry-milled boron largely to this surface curvature effect.

The wet-milled (without oleic acid) sample has far more B^{3+} signal than can be reasonably rationalized by sample curvature. For example, if we model this sample with 50 nm randomly packed spheres, the resulting oxide layer thickness is 1.7 nm - over four times the native oxide layer thickness for flat or dry-milled boron. Either something about the wet-milling process substantially enhances the tendency of the particles to oxidize upon air exposure, or the morphology is not adequately represented by uniform spherical particles.

We considered the possibility that the hexanes used as milling solvent could potentially contain enough dissolved oxygen to oxidize the particles during milling. For 50 nm spherical particles (surface area of 51 m^2/g), forming a 1 nm coating of B_2O_3 would require ~0.12 g of oxygen, for a typical milling batch of 2 g boron. Based on the reported solubility (0.2 mole %)[30] of O_2 in n-hexane at room temperature, it is clear that no more than a few percent of the "extra" oxide could conceivably be attributed to O_2 in the hexanes. This conclusion was confirmed by the observation of similar levels of oxide formation for boron milled using pentane distilled under N_2 as the wetting agent. Similarly, other potential oxygen sources such as an oxide layer on the milling jar/ball surfaces can be discounted because they simply cannot contain nearly as much oxygen as we observe in the wet-milled samples. Another difference between our wet- and dry-milling procedures was that the wet-milled particles were initially exposed to oxygen by bubbling a variable N_2/O_2 mixture through a suspension in hexanes, while dry-milled powder was usually exposed to the variable N_2/O_2 mixture dry. We tested to see if the bubbling process somehow increased the extent of oxidation, by suspending dry-milled powder in hexanes and using the same bubbling procedure that was used for wet-milled powder. The oxide concentration seen in XPS was identical to that for dry-milled material never exposed to hexanes.

Therefore, we conclude that wet-milled boron really does form more XPS-visible oxide than dry-milled boron, when exposed to air. It seems unlikely that milling in hexanes would actually change the surface chemistry to enhance air oxidation - if anything we might expect that the non-volatile residue on the wet-

milled surfaces (see Table 3.2 and discussion) would tend to inhibit oxidation. The likely explanation for the greater oxide concentration is morphology on the few nanometers scale. Suppose, for example, that the wet-milled samples contain a fraction of ultrafine particles only a few nanometers in diameter, or that the 50 - 100 nm particles have asperities or surface roughness on this scale, which is below the resolution limit of our SEM. Such particles or asperities are small enough that for a ~0.5 nm oxide layer, the fraction of oxide visible in the XPS sampling depth (~8-10 nm) would be substantially higher than for large particles with relatively smooth surfaces. For example, a 2 nm particle with the outer 0.5 nm oxidized would be >80% oxide by volume, and the entire particle would be within the XPS-sensitive region. Therefore, even a relatively small increase in the volume fraction of ultrafine particles or of the nano-scale surface roughness, could significantly increase the XPS-visible oxidation level in the samples. It may seem unlikely that wet and dry milling could result in significantly different particle morphologies on the few nanometer scale; however, we note the rate of particle size reduction in wet milling is roughly double that for dry milling, suggesting a significant change in milling mechanism.

We looked for morphology differences on the few nanometer scale using high resolution transmission electron microscopy (HRTEM) on the dry and wet milled samples. Both samples were dispersed in hexanes, ultrasonicated and pipetted onto thin film, holey carbon TEM grids for analysis. Thorough searching revealed no ultrafine particles in either case, so our attention focused on surface roughness. Figure 3.8 shows two HRTEM images taken from the edges of large aggregates from
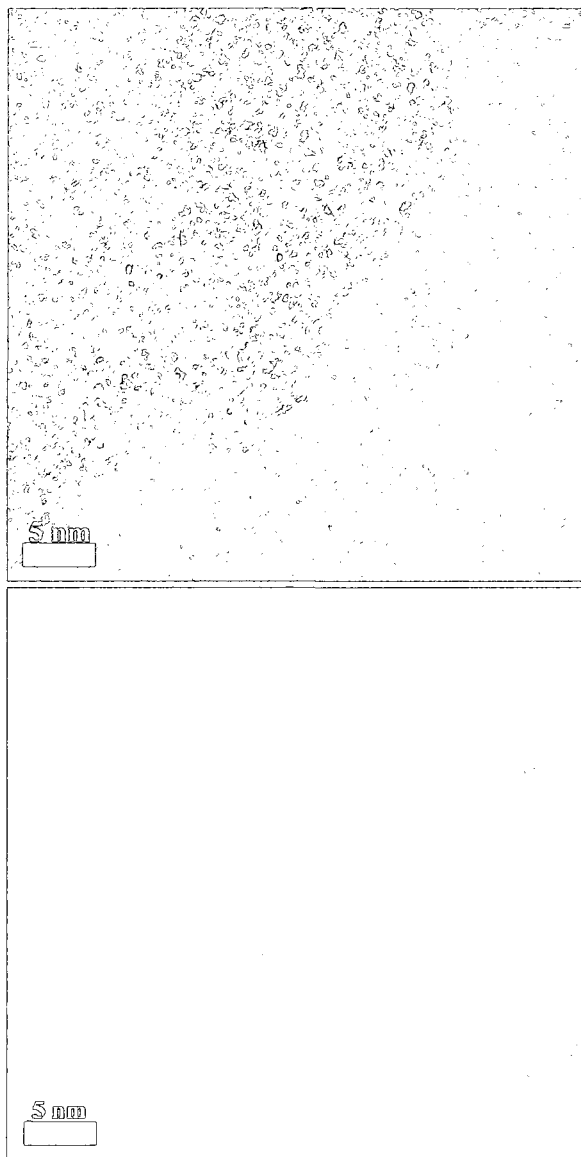
Figure 3.8 TEM images of wet milled (top) and dry milled (bottom) boron samples.

the wet (top) and dry (bottom) milled samples respectively. Because boron is a low Z element, contrast is poor. In each case, the darker regions in the upper left quadrants correspond to aggregates of boron particles; the focus was adjusted for best contrast at the edge. It appears that the edge delineating the boron mass from the underlying support is rougher in the case of the wet milled sample (top) than the dry milled sample (bottom). In order to minimize sampling bias, several particles in each sample were looked at, and the trend seems to be that the wet-milled boron is somewhat rougher than the dry-milled boron.

The important point from our perspective is that boron that was wet milled with oleic acid shows essentially no signal for boron oxide, indicating that the surfaces are completely protected from oxidation, aside from the oxygen in the B-O-C bonds that anchor the ligand to the surface. These particles were milled under identical conditions, and otherwise treated identically to the wet-milled samples, and as far as can be told by SEM the particle size distributions are similar for wet milling with, and without oleic acid. We conclude that oleic acid binds efficiently to fresh unoxidized boron surfaces as they are produced by crushing larger particles, and provides an effective barrier to air-oxidation at temperatures up to at least ~70° C (the drying oven temperature).

3.5   Conclusions

Fuel soluble, oleic acid-functionalized boron nanoparticles, with and without CeO_2, were successfully produced using a simple one step synthesis method. Ball milled powders were produced with a bi-modal size distribution with components peaked at ~50 and 600 nm, respectively, as shown by DLS and SEM measurements.

The components were easily separable; leaving behind only a narrow size distribution peaked at 50 nm, which forms stable colloidal solutions in hydrocarbon solvents and jet fuels. In addition to being fuel soluble, XPS data revealed that the ligand protected nanoparticles were unoxidized; a major step in the development of the use of boron as a potential fuel additive. To our knowledge, this study presents the first demonstration of unoxidized, soluble boron nanoparticles.

Future work will continue to explore new ways of functionalizing and coating boron nanoparticles, as well as looking into ways of modifying milling parameters to produce different size distributions. This method has already been shown to be effective in producing nanosized B_4C, another potentially attractive fuel additive.

3.6   References

(1)   Risha, G. A.; Evans, B. J.; Boyer, E.; Kuo, K. K. *Progress in Astronautics and Aeronautics* 2007, *218*, 413.

(2)   Slutsky, V. G.; Tsyganov, S. A.; Severin, E. S.; Polenov, L. A. *Propellants, Explosives, Pyrotechnics* 2005, *30*, 303.

(3)   Risha, G. A.; Boyer, E.; Evans, B.; Kuo, K. K.; Malek, R. *Materials Research Society Symposium Proceedings* 2003, *800*, 243.

(4)   Kuo, K. K.; Risha, G. A.; Evans, B. J.; Boyer, E. "Potential usage of energetic nano-sized powders for combustion and rocket propulsion." Materials Research Society Symposium Proceedings, 2003, The Pennsylvania State University.

(5)   Young, G.; Sullivan, K.; Zachariah, M. R.; Yu, K. *Combust. Flame* 2009, *156*, 322.

(6)   Wang, J.; Liu, Y.; Zhang, X.; Mi, Z.; Wang, L. *Catalysis Communications* 2009, *10*, 1518.

(7)   Holcomb, R. R.; Holcomb, A. R. Composite metal inorganic and organic sols and colloids as combustion improvers for liquid fuels; Demeter Systems LLC, USA USA, 2006; pp 36.

(8)   Valentine, J. M.; Sprague, B. N.; Peter-Hoblyn, J. D. Fuel-soluble platinum-cerium-iron catalysts for combustion of diesel fuel and jet fuel USA: USA, 2005; pp 12.

(9)   Van Devener, B., Perez, J. P. L., Anderson, S. L. *Journal of Materials Research* 2009, *24,* 3462.

(10)   Pickering, A. L.; Mitterbauer, C.; Browning, N. D.; Kauzlarich, S. M.; Power, P. P. *Chemical Communications* 2006.

(11)   Xu, T. T.; Zheng, J.-G.; Wu, N.; Nicholls, A. W.; Roth, J. R. *Nano Letters* 2004, *4,* 963.

(12)   Chiu, Y. S.; Shaw, P. W.; Ho, S. Y. Bond analysis of coated boron powder In *Combust. Boron-Based Solid Propellants Solid Fuels*; Kuo, K. K., Ed.; CRC Boca Raton, Fla, 1993; pp 181.

(13)   Shyu, I.-M.; Liu, T.-K. *Combustion and Flame* 1995, *100,* 634.

(14)   Trowbridge, J. C.; Breazeale, J. D. Coated boron particles for use in propellent fuels United Technologies Corp., USA USA, 1989; Vol. US 4877649.

(15)   Van Devener, B.; Anderson, S. L. *Energy and Fuels* 2006, *20,* 1886.

(16)   Vincent, M. W.; Richards, P.; Novel-Cattin, F.; Marcelly, B.; Favre, C. *Society of Automotive Engineers, [Special Publication] SP* 2001, *SP-1582,* 177.

(17)   Wakefield, G. Cerium oxide nanoparticles; Oxonica Limited, UK: Great Britain, 2003; pp 14.

(18)   Jung, H.; Kittelson, D. B.; Zachariah, M. R. *Combustion and Flame* 2005, *142,* 276.

(19)   Schaffer, G. B.; Forrester, J. S. *J. Mat. Sci.* 1997, *32,* 3157.

(20)   Suryanarayana, C. *Progress in Materials Science* 2000, *46,* 1.

(21)   Powell, C. J. *Applied Surface Science* 1995, *89,* 141.

(22)   Powell, C. J.; Jablonski, A. *NIST Electron Effective Attenuation Length Database Version 1.1* Gaithersburg, MD, 2003.

(23)   Briggs, D.; Seah, M. P. *Practical Surface Analysis*, second ed.; John Willey & Sons, 1993; Vol. 1.

(24) Charles D. Wagner, A. V. N., Anna Kraut-Vass, ; Juanita W. Allison, C. J. P., and John R. Rumble Jr. NIST X-ray Photoelectron Spectroscopy Database; NIST Standard Reference Database 20, Version 3.4 (Web Version) ed., 2003.

(25) Tielsch, B. J.; Fulghum, J. E.; Surman, D. J. *Surface and Interface Analysis* 1996, *24*, 459.

(26) Meschel, S. V.; Kleppa, O. J. *Journal of Alloys and Compounds* 1995, *226*, 243.

(27) Moulder, J. F.; Stickle, W. F.; Sobol, P. E.; Bomben, K. D.; J. Chastain & R. C. King, J., eds. *Handbook of X-ray Photoelectron Spectroscopy*; Physical Electronics: Eden Prarie, MN, 1995.

(28) Foo, W. C.; Ozcomert, J. S.; Trenary, M. *Surf. Sci.* 1991, *255*, 245.

(29) Wang, Y.; Fan, J.; Trenary, M. *Chem. Mater.* 1993, *5*, 192.

(30) Dias, A. M. A.; Bonifacio, R. P.; Marrucho, I. M.; Padua, A. A. H.; Gomes, M. F. C. *Phys Chem Chem Phys* 2003, *5*, 543.

CHAPTER 4

FUEL SOLUBLE, PALLADIUM BASED, NANOPARTICULATE

COMBUSTION CATALYSTS

While I was responsible for the majority of the work contained within this chapter, nanoparticle generation, FTIR characterization and combustion experiments were performed by Professor Hai Wang, University of Southern California, Department of Aerospace and Mechanical Engineering, and by TDA Inc., Wheat Ridge, CO. A discussion of these topics is included for clarity.

4.1 Overview

Three fuel soluble, palladium based catalysts were tested for activity, using a JP-7 surrogate fuel in a flow tube reactor, and characterized using transmission electron microscopy (TEM), scanning transmission electron microscopy/energy dispersive X-ray analysis (STEM/EDX) and X-ray photoelectron spectroscopy (XPS). Two of the catalysts were prepared in the hopes of preparing fuel soluble bohemite (Al(O(OH)) nanoparticles studded with smaller palladium particles as the active metal. The other was commercially obtained palladium acetyl acetonate (Pd(acac)$_2$). The results showed Pd(acac)$_2$ to be more effective at catalyzing combustion, at least at lower temperatures. The impregnated method of catalyst preparation resulted in particles with the desired structure, and good activity. The exchanged method gave an unexpected material, that still showed some activity, but less so than the other two.

4.2 Introduction

Currently, there is interest in developing new combined cycle propulsion systems for use in space launch applications. For such applications, a substantial reduction in typical fuel ignition delays is required as the fuel and air mixture remain in the combustor for very short periods of time (milliseconds), during the scramjet portion of the flight. Catalysts are needed not only to enhance fuel ignition and combustion rates, but also to control endothermic cracking reactions in the fuel which is used as a heat sink in these applications.[1]

The usual solution to catalytically enhancing combustion, fixed bed reactors coated with a catalyst, cannot be used in these applications as the flow velocities are too high. One way around this problem, is to introduce the catalysts directly into the fuel

by solubilizing them. For soluble catalysts, there are key conditions that need to be met in order to be useful. They must have large surface areas in order to maximize the number of fuel/catalyst encounters, and they also must be highly soluble in the fuel to prevent settling and clogged fuel lines.

Supported palladium is well known as a methane combustion catalyst.[2] Recently, it has also recently been shown to be effective towards catalyzing JP-10 combustion.[3] In this chapter, two different methods of preparing fuel-soluble, nanoparticulate, palladium on supported bohemite catalysts are presented.

These catalysts were tested for activity, characterized as prepared and after passage through a reactor, and the results were compared with a commercially obtained catalyst, Pd(acac)$_2$ (palladium acetyl acetonate). X-ray photoelectron spectroscopy (XPS), high resolution transmission electron microscopy (HRTEM) and scanning transmission electron microscopy/energy dispersive x-ray analysis (STEM/EDX) were used to study particle surfaces, sizes, morphologies and compositions. Catalytic activity testing was carried out using a JP-7 fuel surrogate (described later) in a Mellen type tube furnace reactor. A brief discussion of these results is included for completeness, with full details found elsewhere.[4] The focus of this chapter is on the properties of the particles, and how they correlate with reactor conditions.

4.3 Experimental

4.3.1 Catalyst preparation

The prepared oxidation catalysts consist of an active catalytic site incorporated into boehmite nano particles. Two different procedures were used to prepare the catalysts. In both procedures, the preparation consists of two basic steps: solublizing

the bohemite particles via a reaction with organic acids, followed by the addition of the catalytic metal, in this case palladium. The primary difference between the two methods is in the way in which the palladium is added. In one method, henceforth called the exchanged method, the soluble bohemite particles are reacted with a solution of palladium acetylacetonate (Pd(acac)$_2$). One problem with this step is that it didn't always go to completion, leaving behind Pd(acac)$_2$ which is also fuel soluble. As a consequence, this prompted the use of another way of adding the metal, from here on called the impregnated method. Here, the soluble bohemite particles are simply impregnated with a metal salt, Pd(NH$_3$)$_4$(NO$_3$)$_2$. This salt is not soluble in hydrocarbons, ensuring that any palladium in the organic matrix is impregnated on the fuel soluble catalyst.

Solubilized bohemite was prepared by mixing Catapal A (Sasol, Inc.) with water and propionic acid (CH$_3$CH$_2$COOH). In a typical batch, 20 g of Catapal A is added to 20 g water. A separate mixture of 1.75 g propionic acid and 3.5 g water is also prepared. The acid solution is mixed with the Catapal A solution for approximately 30 minutes. The resulting solution was then mixed with 130 g water, and heated at 75° C for ~24 h After this point, the mixture is in the form of a gel which we refer to as an alumoxane. Due to the polar propionic acid, this alumoxane is soluble in water. To produce a hydrocarbon soluble alumoxane, these bohemite particles must be functionalized with longer chain paraffinic acids. A solution of oleic acid in ethanol was prepared by dissolving 7.4 g oleic acid in 160 g ethanol and heating the mixture to 75° C. This mixture is then added to the alumoxane gel to produce the oleic acid functionalized bohemite particles.

As mentioned before, two different methods were used to introduce the catalytic metal, palladium, into the bohemite. In the exchanged method, palladium acetylacetonate is exchanged into the boehmite matrix forming an aluminum acetylacetonate molecule. To carry out this reaction, the alumoxane is dissolved in toluene and then the amount of acetylacetonate that results in an alumina to metal ratio of 12:1 is added. The solution is then refluxed at about 120° C for 24 h. The resulting solution has a dark color indicating a reaction has taken place. To measure the progress of the reaction, FTIR was used to monitor peaks that correspond to palladium acetylacetonate. In addition, one of the driving forces behind the exchange reaction is the formation of aluminum acetylacetonate.[5] Therefore, the formation of this compound was monitored with FTIR as well.

An example of a preparation method for the impregnated catalyst follows. 62.5 g of propionate-oleate alumoxane solution (molar ratio of aluminum to propionic acid and oleic acid of 12:1) was mixed with 6.274 g $Pd(NH_3)_4(NO_3)_2$ solution [1.4 g $Pd(NH_3)_4(NO_3)_2$ or 0.5 g Pd in 10 g solution]. In this case this resulted in a molar ratio of aluminum to palladium of 12:1 in the solid catalyst. The material was then dried, resulting in about 4.1 g of Pd impregnated alumoxane catalyst. After drying the material, the impregnated catalyst can be separated from any residual $Pd(NH_3)_4(NO_3)_2$ compound by dissolving the material in toluene. Since the tetraamine salt is not soluble in toluene, any $Pd(NH_3)_4(NO_3)_2$ detected that is dissolved in the toluene phase can be attributed to the impregnation of the material on the soluble boehmite particles. About 3 g of impregnated catalyst was mixed with 600 g of toluene, and the mixture was

ultrasonicated for 20 h. The mixture was then allowed to settle, and then the dissolved phase was separated from the material that was insoluble.

The solubility of the catalyst can be measured by driving off the solvent in a portion of the dissolved phase and weighing the residual material left. Using this method, we obtained a solubility of 3730 ppm in one case. The ceramic yield of this material (the amount of material left after heating the catalyst to 600°C to burn the organic ligands off) is 55% and therefore the solubility of the inorganic palladium/alumina is 2060 ppm. Although this is much higher than will be needed to increase combustion rate, it allows us to add catalyst to the fuel using a concentrated solution.

4.3.2 Flow reactor

Figure 4.1 shows a diagram of the instrument used to measure catalytic activity. A high performance liquid chromatography pump (HPLC) was used to inject the fuel/catalyst solution. To generate a well atomized spray, the fuel is metered into an injector where it mixes with a 300 sccm oxygen/nitrogen flow. The resulting small droplets are entrained in the primary flow, minimizing contact with the reactor walls. Our goal was that this configuration promoted the vaporization of the entrained fuel droplets in the air stream, leaving well dispersed catalyst particles evenly distributed throughout the mixture to provide consistent, meaningful data.

The reactor itself consists of a 3/4-in OD, 36 in long quartz tube that is heated by a 1000 W Mellen tube furnace. The furnace is capable of reaching temperature of over 1000° C as measured midway through the enclosed flow path. An online CO_2 nondispersive infra-red (NDIR) analyzer (California Analytical) was used to monitor
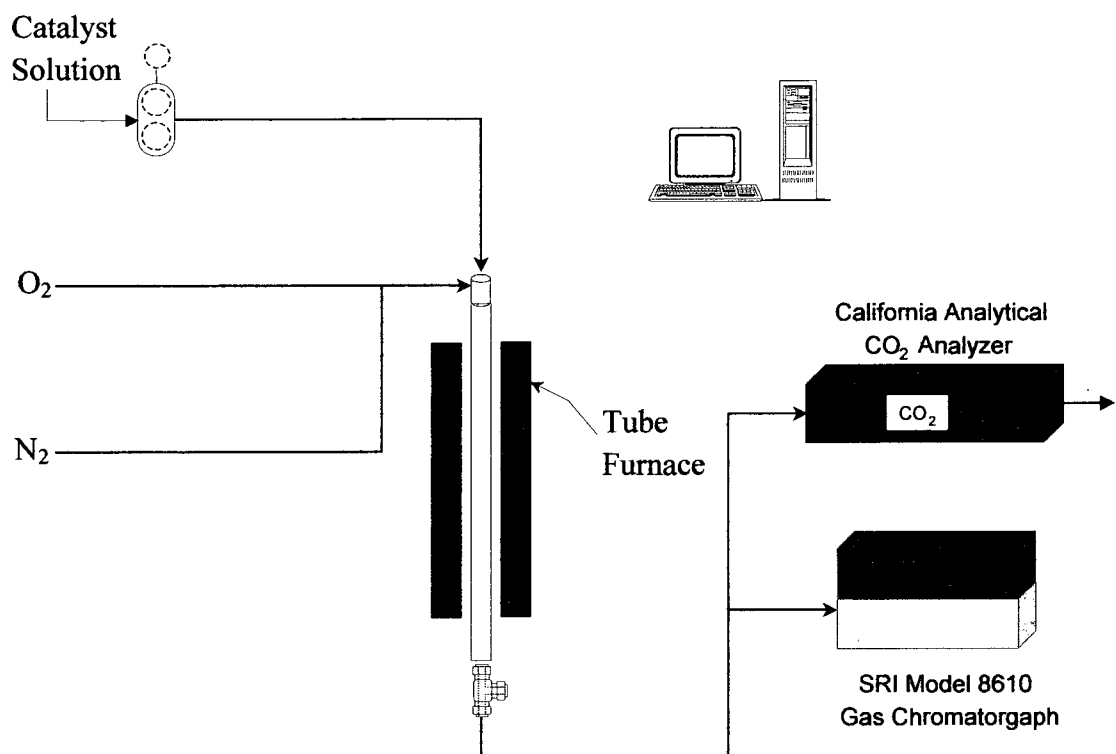
Figure 4.1 Flow tube reactor.

the progress of the reaction. The on-line analyzer is reliable, provides stable measurements and responds rapidly to changes in gas phase concentrations of CO_2.

A JP-7 surrogate was used as the fuel to test the catalysts for oxidation activity. JP-7 contains 65% parrafins, 32% napthenes (or cycloparaffins) and 3% aromatics.[6] Specifically, Norpar-12 was used as the paraffin, decalin as the napthene and tetralin as the aromatic. For combustion measurements, a flow of 33.6 slpm nitrogen and 1.8 slpm oxygen was developed and then the tube was heated to ~300° C. The fuel was injected a rate of 1 cc/min, giving a fuel to air ratio that is approximately stoichiometric. The oven temperature was ramped up at a rate of 10° C per minute, and the production of CO_2 was monitored as a function of temperature. Since this analyzer provides real time data and updates rapidly, a temperature ramp can be used to characterize the level of combustion versus temperature.

4.3.3 Particle sampler

In addition to characterizing the catalysts as prepared, they were also sampled after passage through the reactor using the setup shown in Figure 4.2. In this setup, the exiting gas mixture from the flow reactor is immediately diluted by a cold flow of nitrogen. From here, the particles are carried towards a TSI 3080 scanning mobility particle sizer (SMPS) for particle size distribution estimates. After passing through the SMPS, the particles are collected on a TEM grid using a TSI electrostatic precipitator (TSI 3089) for microscopy and EDX analysis.

For the post reactor particle collection experiments, the Pd-based catalysts were suspended in toluene and injected into the inlet of the reactor with a nitrogen flow. Once in the inlet, the catalyst mixes with a N_2/O_2 flow giving a total flow rate of the
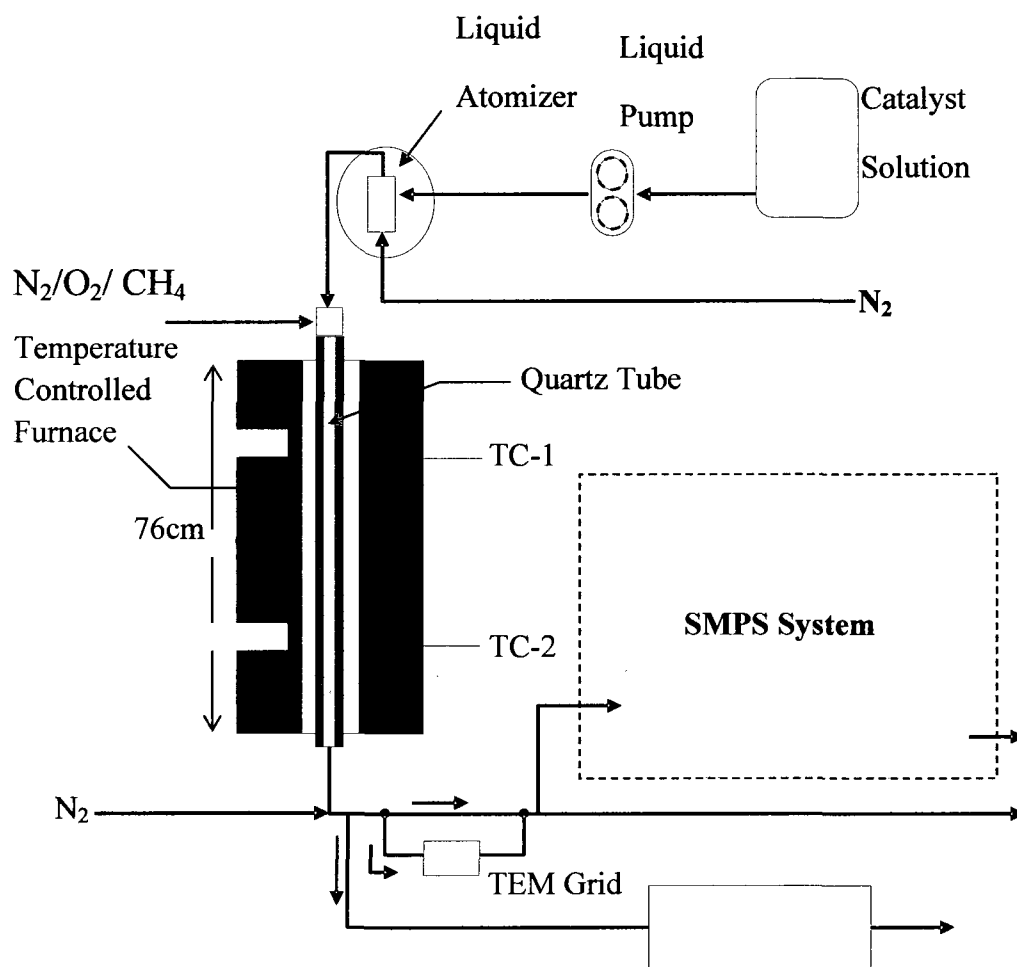
Figure 4.2 Particle sampler.

mixture of 6.75 slpm, which includes a 500 sccm N_2 injector flow, 2.7 slpm N_2 and 3.5 slpm O_2 fuel-line flow, and 0.05 slpm evaporated catalyst solution. At the inlet of the reactor, the flow is laminar and fully developed and the extent of particle coagulation through the reactor is not severe.[4]

4.3.4 Particle characterization (XPS, microscopy/EDX)

X-ray photoelectron spectra were collected using the monochromatized Al K alpha source (1486.7 eV) on a Kratos Axis Ultra DLD instrument with the Al anode set at a potential of 15 kV and a current of 15 mA for all experiments. In order to maintain a reasonable count rate from the detector, the x-ray spot size was kept at 300 x 700 microns for both the low resolution survey scans, as well as the high resolution region scans. For survey scans, the pass energy on the hemispherical analyzer was set to 160 eV, while the corresponding value for the higher resolution region scans was 20 eV.

For XPS analysis, samples were deposited on the sample holder using two methods with similar results. The dry catalyst was pressed into carbon tape, however, this method results in some carbon background from the tape that complicates the estimates of atomic concentrations. The data presented below were obtained by evaporating several drops of the toluene solution of the each catalyst on the sample holder, with enough deposited to completely block any signals from the stainless steel sample holder. Not unexpectedly, all of the samples showed a propensity for charging during XPS, and the instrument's charge neutralizer was set to minimize the width of the resulting peaks. Even so, some shift in the absolute binding energy (BE) scale due to sample charging is likely; thus the scale must be calibrated. As shown below, the spectra of the as-deposited samples are quite broad even with charge neutralization, and

do not provide useful reference peaks for BE scale calibration. To provide a reference peak, a small concentration of argon atoms was implanted into the sample using 1 keV Ar^+. Changes in the spectra induced by this Ar^+ implantation are discussed below. The BE scale was then shifted so that the Ar 2p BE was 241.8 eV. Note that several studies have shown relatively small BE shifts for Ar deposited in a variety of materials, including metals, oxides, graphite, and amorphous carbon;[7-9] thus we believe that our BE scale should be accurate to about ± 0.3 eV.

While our primary interest in the XPS data is using BEs to identify the chemical state of the elements present in the samples, it is also possible to extract approximate elemental composition from the integrated XPS peak intensities. The compositions must be interpreted with caution, however, because XPS detects only electrons from the top few nanometers of the samples. Quantification was performed using the standard equation:[10]

$$C_x = \frac{I_x/S_x}{\sum I_i \, S_i}$$

where C_x is the atomic fraction of a given elemental constituent in a particular sample, I_x is the number of photoelectrons per second in a given spectral peak and S_x is the atomic sensitivity factor for a given peak (provided by the instrument manufacturer, Kratos Inc.). This analysis assumes that the samples are homogeneous over the depth range sampled by XPS, which is clearly not true for these samples. Interpretation of the concentrations will be discussed below.

For transmission electron microscopy (TEM), samples were deposited from solution on ultrathin holey carbon film 400 mesh copper TEM grids, and allowed to dry

before introduction into the microscope vacuum systems. High resolution TEM was performed on an FEI Technai F30 using a beam energy of 300 KeV. Scanning TEM (STEM) analysis was performed on an FEI Technai F20, at a beam energy of 200 keV, using the high angle annular dark field detector (HAADF). Energy dispersive x-ray (EDX) analysis of elemental compositions was also performed on the STEM instrument.

4.4 Results and discussion

4.4.1 Catalyst activity

Figure 4.3 shows the results of catalytic oxidation testing of the exchanged and impregnated catalysts at two different concentrations, 50 and 200 ppm. Here, ppm refers to the concentration of the inorganic portion of the catalyst; the alumina and the metal. For baseline reference, the results obtained with no catalyst are also shown. The figure shows the CO_2 concentration of the gas exiting the reactor plotted as a function of furnace temperature.

Clearly, the results demonstrate that the palladium containing catalysts lower the temperature at which combustion begins, as compared to the baseline. Focusing on the impregnated catalyst at 200 ppm loading, the reaction rate, as measured by CO_2 production, begins to increase at around 650° C, which is around 300° C lower than the non-catalytic case. The rate of increase in CO_2 concentration remains relatively constant until about 725° C. At this point, the rate of increase in CO_2 prodcution slows and the data become noisier. A plausible explanation for this noise is that at this point in the combustion, the exotherm is affecting the mixing temperature, thus affecting the reaction rate. Considering the relatively low flow rates used here, it is likely that some
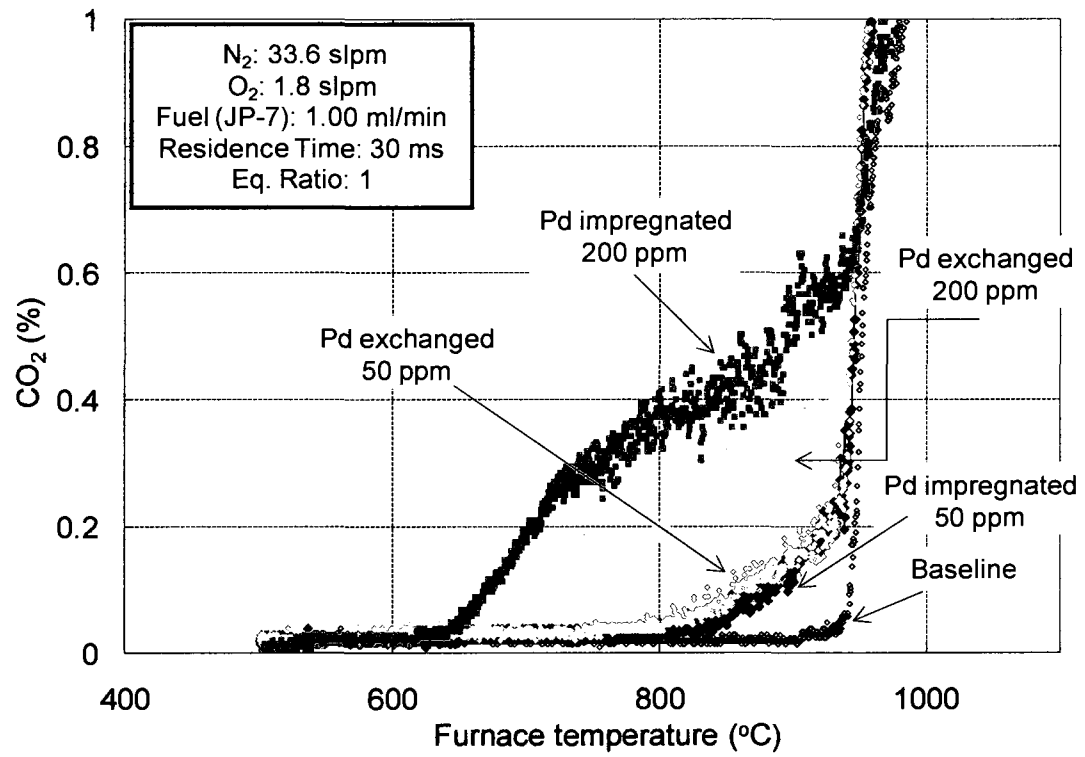
Figure 4.3 Catalytic activity testing, impregnated and exchanged catalysts.

turbulence is introduced into the flow, which may affect the temperature of the mixture. At around 900° C, gas phase combustion becomes dominant, as evidenced by the dramatic increase in the reaction rate.

At 200 ppm loading, the exchanged catalyst appears to much less active than the impregnated. Here, the reaction rate does not start to increase until a reactor temperature of around 725° C; around 100° C than that seen for the impregnated catalyst under similar conditions. Qualitatively, the shape of the CO_2 production curve is comparable to that found for the impregnated sample, suggesting similar mechanisms.

At 50 ppm, the results are very similar for both catalysts, showing little activity compared to either 200 ppm case. Furthermore, no fast initial rate increase is seen here. Instead, the slope of the curve remains more or less constant from the point of ignition to the point at which the fast gas phase chemistry takes over.

Figure 4.4 shows the analogous combustion results obtained using a $Pd(acac)_2$ catalyst. The $Pd(acac)_2$ was loaded at concentration of 22 ppm, which produced equivalent metal concentrations to the 50 ppm concentrations in the impregnated and exchanged samples.

From the figure, it appears that the $Pd(acac)_2$ is initially much more effective as compared even to the higher loading 200 ppm cases for the impregnated and exchanged catalysts. CO_2 production begins to take off at around 450° C, almost 500° C lower than the noncatalytic case and 200° C lower than that seen for the impregnated catalyst at 200 ppm. The combustion rate continues to increase until about 625° C and at this point begins to decline gradually until a temperature of 940° C, where the gas phase
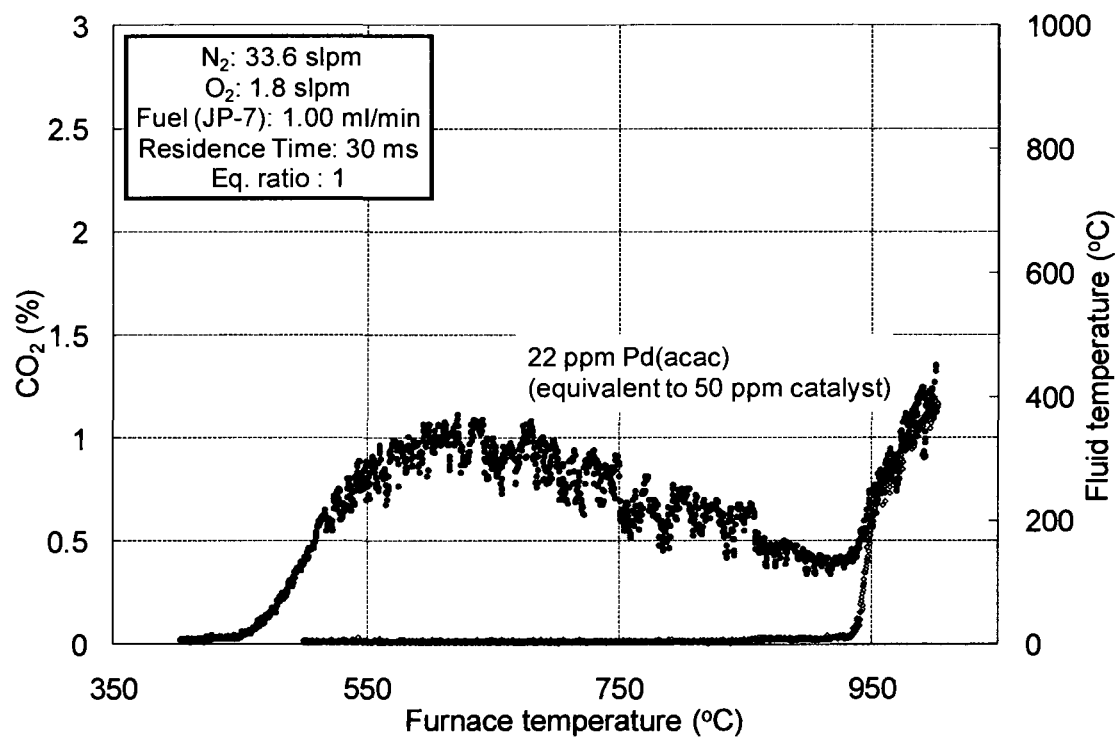
Figure 4.4 Catalytic activity testing, Pd(acac)$_2$.

reaction takes over. This decrease in activity at higher temperatures could possibly be due to a reduction in Pd from Pd^{2+} to metallic Pd, which would be less active towards catalysis. If this is the case, it is unclear at this point why the impregnated and exchanged catalysts do not show this behavior.

Another consideration, applicable to all of the combustion results here, is the possibility of wall catalysis. By directly introducing the particles into the reactor, it is possible that some would radially diffuse through the gas flow and stick to the walls, thus making determinations of catalyst effectiveness based on loading difficult. Thermophoretic forces would tend to favor the particles remaining nearer the centerline of the flow, as the gas temperature has a finite heating rate and tracks behind the temperature of the reactor walls. Nevertheless, it should be noted that wall deposition of particles is still likely; thus results must be interpreted with caution.

4.4.2 Characterization of impregnated catalyst

Figure 4.5 shows three representative TEM images, two from the as-prepared impregnated catalyst sample and one collected after passage through the flow tube at catalytic temperature (690° C). The image on the top shows a large ~230 nm diameter particle containing significant darker areas. TEM contrast increases with atomic number, therefore the obvious interpretation is that this image shows a 230 nm boehmite particle, unevenly covered by a Pd-rich deposit, presumably from the impregnation salt. The middle image shows a smaller ~21 nm diameter particle taken at higher magnification (800 k times). These images are representative of the sample: most of the particles seen were either in the 200-300 nm range or ~20 nm in diameter, with the majority being in the 200-300 range. In the middle image, one can see the
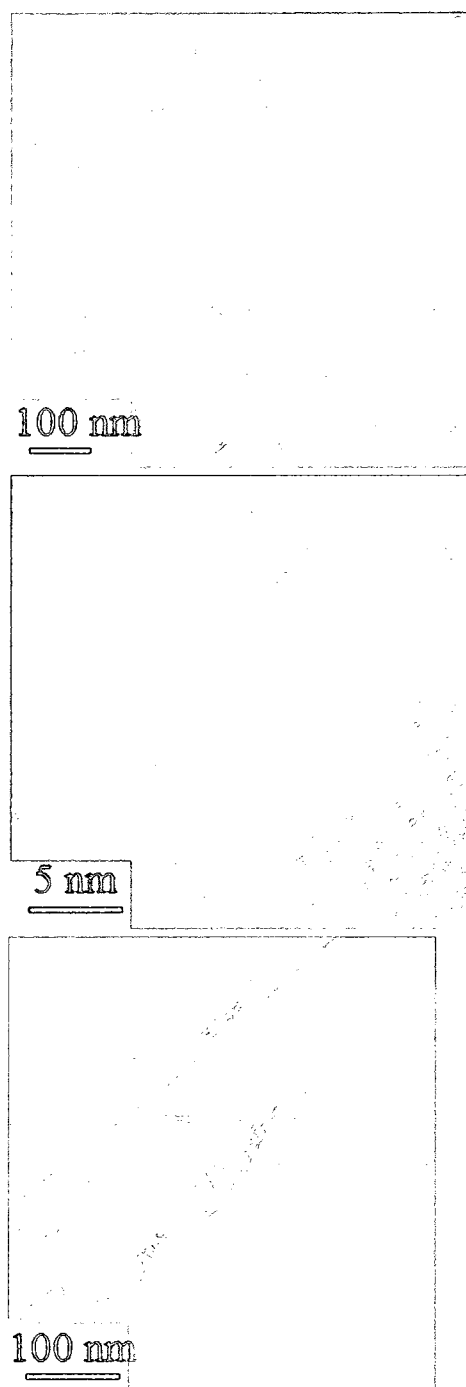
100 nm

5 nm

100 nm

Figure 4.5 TEM images impregnated catalyst.

atomic structure of the particle in the form of lattice fringes visible in the lower left corner of the image, which indicates that the particle is crystalline.

The bottom image is representative of particles seen in the impregnated sample after passage through the reactor. Here an aggregate of large particles is seen attached to a spire from the TEM grid. Notice the same patchy dark areas as in the top image for the as prepared catalyst. The main difference between the post combustion sample and the as prepared, seems to be the lack of any ~20 nm diameter particles. Only particles greater than ~100 nm were seen in the TEM work with this sample, an observation confirmed by the particle sizing data obtained with the TSI electrostatic classifier, which counted no particles under 100 nm. A higher collection of large aggregates, some greater than 500 nm in diameter, was also seen for the post combustion sample, suggesting a tendency for the larger particles to aggregate while passing through the furnace.

The image in Figure 4.6 is a STEM dark field image of one of the larger particles in the impregnated sample. An EDX spectrum was obtained for the region within the red box (on the particle) for chemical analysis. Table 4.1 summarizes the quantification data, obtained from the spectrum by integrating peak intensities and taking into account elemental sensitivity factors, provided by the EDAX™ software supplied with the microscope. The composition is roughly what might be expected for a Pd-impregnated boehmite particle (AlO(OH)) that has been functionalized with organic ligands, and also contains some adventitious carbon. Some of the carbon and all of the copper signals are coming from the underlying TEM grid. EDX data were also collected for a scan region that did not include any particles visible at this magnification, and as
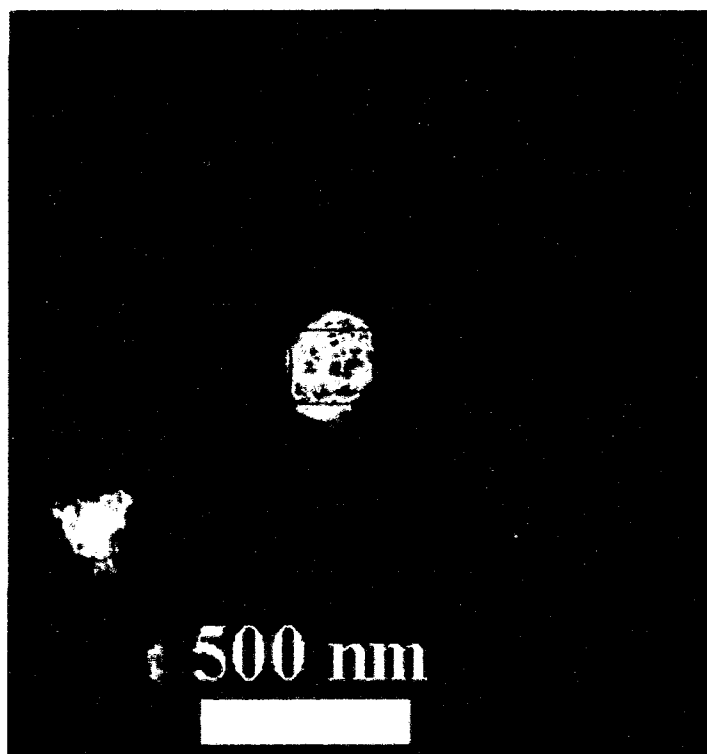
Figure 4.6 STEM image impregnated catalyst.

Table 4.1 EDX results impregnated catalyst.

element	EDX atomic composition atomic %	weight %
C	58.5	34.9
O	25.9	20.6
Al	8.3	11.1
Cu	2.4	7.4
Pd	4.9	25.9

expected, there was negligible (0.1 wt %) Pd signal, and C, O, and Al signals about 5 times smaller than for the particle.

XPS spectra were obtained for the sample both as deposited and after sputter cleaning with Ar^+ ions. Table 4.2 summarizes the results, showing that C, O, Al, Pd and N are present on the surface of the sample. These concentrations were calculated under the assumption that the surface was flat and homogeneous, therefore the results are approximate. The apparent composition of the as-deposited sample is dominated by oxygen and carbon, with small amounts of Pd and Al. Trace amounts of N, presumably from the impregnation salt, are also detected. After sputter cleaning, the carbon signal is substantially reduced, as expected for Pd/bohemite particles covered by a layer of oleic acid ligand. The ligand chain length is ~1.5 nm, and the effective attenuation lengths in hydrocarbon for the photoelectron energies of interest range from ~2.8 to 3.3 nm.[11] Therefore, we would expect the XPS peaks for Al, Pd, and O from the underlying particles to be attenuated by roughly 40%, assuming a 1.5 nm thick hydrocarbon overlayer. The increases in intensities for Pd and Al are roughly consistent with this expected attenuation, although the nature of the sample complicates the analysis (see below). The oxygen concentration and O:Al ratio for the as-deposited sample are higher than expected for oleic acid functionalized alumina. Excess oxygen may indicate that the sample surface, as evaporated from solution, is either air-oxidized or is covered by oxygen-rich species that were present in the solution. For example, if the solution contained excess oleic or propionic acids left over from the catalyst synthesis, these might deposit on the surface during evaporation.

Table 4.2 Surface composition impregnated catalyst.

| Atomic composition			
before sputtering		after sputtering	
element	atomic %	element	atomic %
Pd	1.1	Pd	4.0
Al	6.2	Al	19.9
C	77.5	C	41.0
O	14.5	O	33.5
N	0.8	N	0.8
Ar	-	Ar	0.8

As the surface is sputtered, the carbon intensity decreases by a factor of ~2, and the O, Pd and Al intensities increase, as removal of the carbonaceous layer exposes the Pd-impregnated boehmite. The observation that the Pd and Al signals increase in tandem is consistent with the expectation that the Pd is associated with boehmite surface, rather than simply being co-deposited from solution. Eventually, the atomic concentrations reach steady state, i.e., the rate at which sputtering removes each element becomes equal to rate at which more of that element is exposed by sputtering away overlying material. Analysis is complicated by the fact that the sample is a heterogeneous matrix of Pd-loaded boehmite particles, each coated with a thin carbonaceous ligand layer. Accurately calculating sputtering efficiencies for a sample with such a complex structure is impractical.

Taking into account the nature of the sample, the concentrations determined from XPS are reasonably consistent with expectations. In particular, the Pd concentration measured by XPS is close to the value obtained from STEM/EDX (Table 4.1), which is somewhat surprising given that the two techniques probe different regions of the sample. STEM/EDX probes the entire thickness of a single particle, whereas XPS probes only the top few nanometers of the sample, i.e., the surface as exposed by sputtering. The two measurements probably agree because after sputtering XPS probes an area containing many particles at different stages of sputter erosion, such that the area-averaged composition is similar to the bulk average over a single particle.

High resolution XPS scans were also performed on the Pd 3d region of the spectrum. Figure 4.7 shows a high resolution spectrum, for the as-deposited material after exposure to Ar^+ bombardment. As seen in the figure, the features are quite broad,
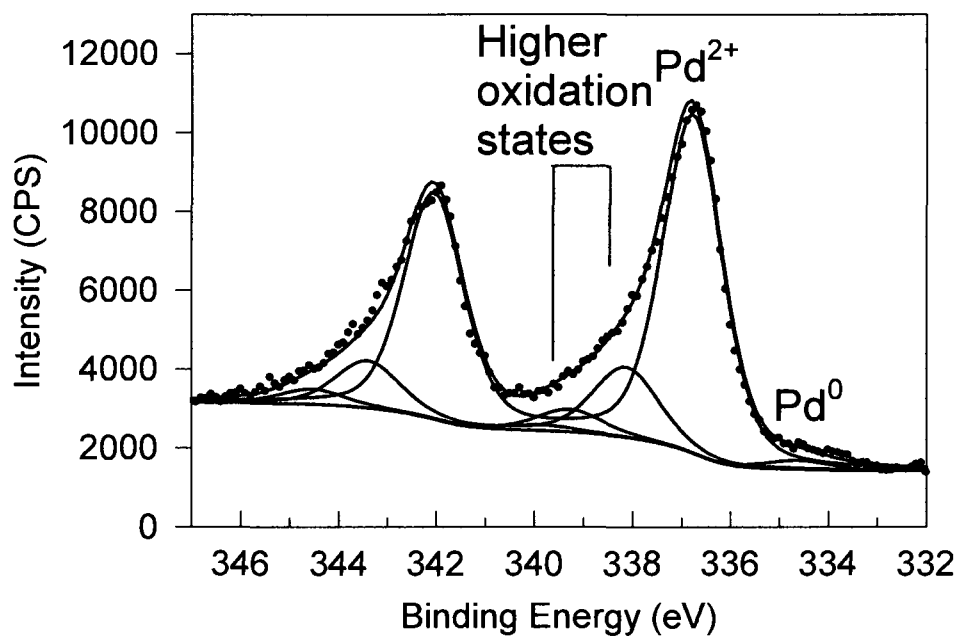
Figure 4.7 Pd 3d XPS spectrum, impregnated catalyst.

indicating substantial differential charging, despite use of the charge neutralizer to minimize the peak width. The implication is that the sample is sufficiently insulating that electrons from the neutralizer are unable to reach positive charges induced by photoemission below the sample surface.

For reference, high resolution XPS scans were also acquired for palladium foil, both with and without an oxide film. The foil was abrasively cleaned, exposed to ambient air for a day, then examined by XPS after sputter cleaning. Fitting of the spectra (using a peak width determined by XPS of gold foil) showed only one peak at 335.1 eV after sputtering cleaning, assigned to metallic Pd, which compares reasonably well with literature (335.7 eV).[12] With this reference value, and taking into account the combined with the fact that the most common oxidation states for palladium are Pd, Pd^{2+}, and Pd^{4+}, the assignment of the three peaks can be completed.

To provide some insight into the Pd chemical states present, the spectrum was fit. Figure 4.7 shows the results, with the raw data plotted as points and the overall fit, the peak components, and the Shirley background shown as solid lines. The component peaks were constrained to have the same shape as was determined from the Pd foil reference sample. Using these conditions, four peaks, along with their corresponding peaks due to spin orbit splitting, produced the best fit. The main peak, corresponding to 76% of the Pd intensity, is centered at 336.8 eV, and assigned to Pd^{2+} as expected given that the catalyst was not reduced, calcined or otherwise modified after impregnation with the $Pd(NH_3)_4(NO_3)_2$. The fit suggests that small concentrations of both Pd^0 (2%) and a two higher Pd oxidation states (22%) are also present; however, the apparent concentrations are small and may simply be an artifact of residual broadening from

differential charging. These two peaks are labeled "higher oxidations states" in the figure.

When considering the relation of the characterization results with the impregnated sample's activity, it is not unreasonable to conclude that the large fraction of palladium in + 2 and higher oxidation states plays a significant role. As has been shown earlier, the oxidation state of palladium has been shown to have significant effects on catalysis of methane combustion.[2,13,14] Of course, this is not the only factor to consider; both the exchanged and Pd(acac)$_2$ catalysts also contain palladium that is largely in electron deficient forms and both show markedly different behavior towards catalysis, as seen in Figures 4.3 and 4.4.

Of critical importance for heterogeneous catalysis is the surface area of the active material available to interact with the fuel. While initially covered by an oleic acid coating in order to make them fuel soluble, it is reasonable to assume that soon after the Pd impregnated bohemite particles enter the flow tube the organic ligands are burned off leaving behind exposed Pd surfaces. The question is what effect does the Pd being impregnated in such relatively large (~200-300 nm structures) have on its activity. Furthermore, it appears from the analysis of the post combustion material that the particles have at least some tendency to agglomerate during their passage through the reactor. This would lead to even less Pd available for interaction with the fuel. It may be more effective to simply introduce the Pd based catalyst in a more highly dispersed form, an idea more fully discussed later.

4.4.3 Characterization of exchanged catalyst

Three TEM images of the exchanged catalyst are shown in Figure 4.8. As for the impregnated sample, the top and middle images are from the as prepared catalyst, with the bottom taken after passage through the reactor. The top image was taken at the same magnification as that in Figure 4.5 and shows that, instead of the expected (100 – 300 nm) boehmite particles, the sample instead contains an abundance of sub-10 nm particles. The high particle/background contrast indicates that the particles are rich in high Z elements, presumably Pd. In addition to the particles, the background in the image appears to be filled with a transparent material with a wrinkled or polycrystalline appearance. This material is not present in the other samples (cf. Figure 4.5), and we will refer to it in the following discussion as the "matrix." Many areas of the sample were imaged with similar results – almost no large particles resembling the boehmite starting material. A higher magnification image of one of the small particles (middle) shows clear lattice fringes indicating that at least some fraction of the particle is crystalline. Low magnification images were analyzed to obtain estimates of the size distribution and most of the particles were found to lie between 6 and 10 nm.

The dramatic difference between the nanostructure of the exchanged and impregnated catalysts is reflected in the micro- and macroscale properties as well. The microscale structure of both catalysts, dried from saturated toluene solutions, was examined by low resolution scanning electron microscopy (SEM), using a Leo Stereoscan 440 i. The impregnated catalyst, as expected, dries to micron scale aggregates with grain structure on the several hundred nanometers scale, i.e., aggregates of the boehmite particles observed in the TEM images. The exchanged
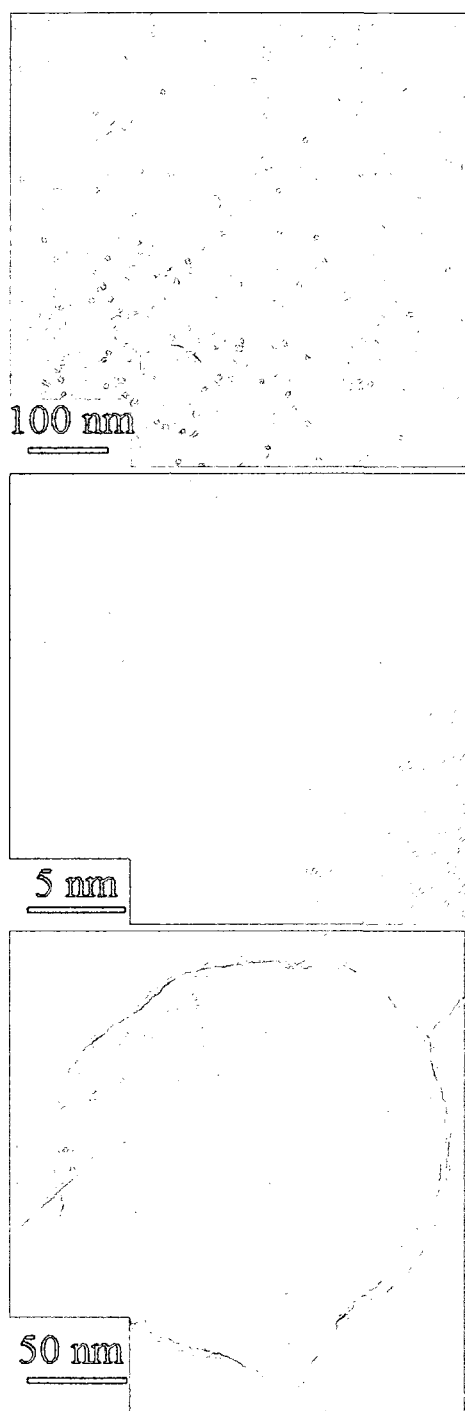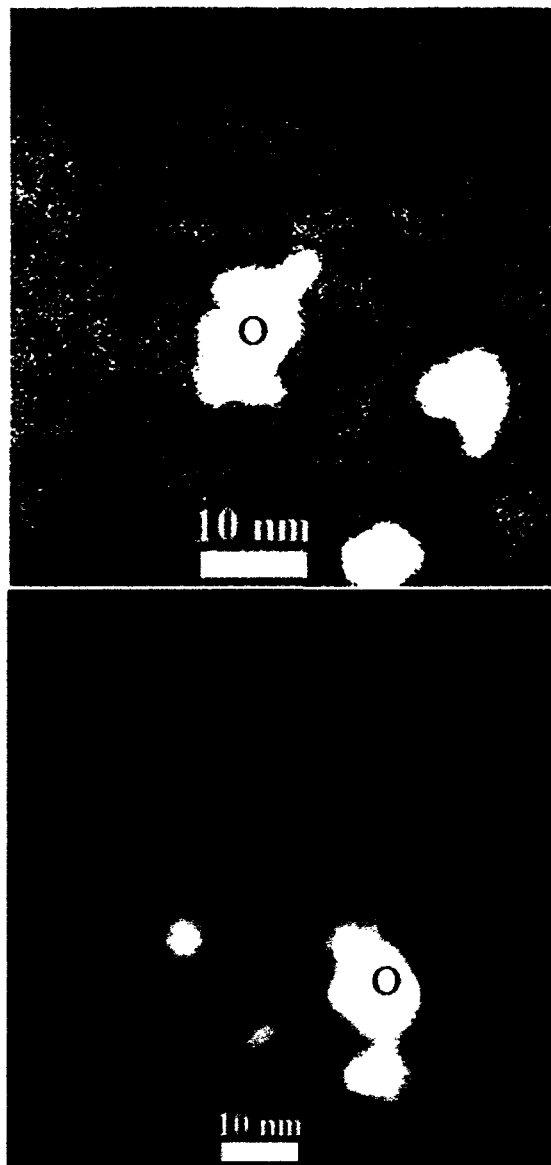
Figure 4.8 TEM images exchanged catalyst.

catalyst dried to a glassy looking deposit with no particulate structure observable at the SEM resolution (~100 nm). Finally, the dried impregnated catalyst is an off-white powder, while the exchanged catalyst dries to a black paste-like material. The paste-like consistency presumably reflects the matrix material, and the black color is attributed to light scattering by the nano-scale, Pd-rich particles.

The bottom image in Figure 4.8 shows a representative image of the exchanged sample collected after reactor passage, showing dramatic changes in structure. The TEM grid was thoroughly surveyed and very few discrete small particles could be found. Instead, the majority of the smaller particles appeared to be imbedded in larger structures on the order of 100 nm in diameter. This conclusion is supported by the particle sizing data collected with the electrostatic precipitator which indicated a mean particle diameter of 150 nm. The image shown is typical of the sample, and the overall concentration of particles was quite low as compared to the impregnated sample. Looking closely at the figure, it appears to be studded with darker particles 5-10 nm in diameter. These are presumably Pd rich, but direct identification of these, as well as that of the larger structures not seen in the as prepared catalysts will be discussed below with the STEM/EDX analysis.

STEM/EDX results for the exchanged catalyst are summarized in Figure 4.9 and Table 4.3. The as deposited catalyst is shown in the upper image. Three typical ~10 nm diameter particles can be seen, and the EDX spectrum was taken with the tightly focused beam passing through the particle nearest the image center. The intensities should reflect the particle composition, but also contributions from the matrix material which presumably coats the particles when the sample dries. The sensitivity-corrected

Figure 4.9 STEM images exchanged catalyst.

Table 4.3 EDX results exchanged catalyst.

EDX results exchanged catalyst					
as prepared			after passage through reactor		
element	at %	wt %	element	at %	wt %
C	79.3	58.9	C	82.1	64.6
O	8.8	8.7	O	9.3	9.8
Al	0.4	0.7	Al	2.2	3.8
Si	8.6	14.9	Si	3.6	6.5
Cu	0.8	3.1	Cu	1.4	6.0
Pd	2.9	13.7	Pd	1.3	9.0

weight and atomic percent compositions are shown in the table. The largest signal is seen for carbon, presumable from the solublizing ligands. Similar analysis was performed on the matrix area which contained no particles. It was found that the matrix is primarily composed of carbon, presumably from the solubilizing ligands as well as adventitious carbon, as well as silicon and oxygen in a roughly 1:2 ratio. The "particle plus matrix" spectrum contains signal for Pd, as well as C, Si, and O, but very little Al signal, in sharp contrast to the impregnated sample results. (The Cu peak is attributed to background from the copper TEM grid). The two surprises here are the absence of significant Al signal for the particles, and the strong Si signal, which seems to be mostly associated with the matrix material. Note that EDX spectra often show an artificial Si peak due to the so called silicon dead zone in the detector; however, the Si artifact peak usually accounts for no more than ~1% of the total signal.[15] The Si peak for the exchanged sample is an order of magnitude larger than what could reasonably be attributed to this artifact, and no such artifact was observed for the impregnated sample, which was examined during the same instrument session. Furthermore, when the analysis was repeated on a fresh TEM grid, spotted with a separately prepared solution of the exchanged catalyst (same catalyst batch), the EDX composition was similar. XPS also found Si contamination of this sample, and those results are discussed below. The source of the Si was eventually traced to impurities in the toluene solution the exchanged catalyst was dissolved in.

The absence of particles in the >50 nm size range, and of significant Al EDX signal, together with the appearance of many 6 – 10 nm crystalline, Pd-rich particles, indicates that the ion exchange procedure used to prepare this sample did not produce

the intended Pd-substituted boehmite particles. Instead, the boehmite was lost from the toluene-soluble product somehow, and replaced by small Pd-rich, soluble particles.

It is interesting to note that Katakura and Yoshihiro have reported that $Al(acac)_3$ can be synthesized simply by reacting bohemite with acetyl acetone (Hacac) in water at low temperatures, with the $Al(acac)_3$ precipitating out.[16] We are not suggesting that this is definitely what is happening. We are merely providing one possibility. It could also be that the $Pd(acac)_2$ did not fully exchange into the sample, leaving behind a mixture of Pd and Al acetylacetonate, as a test of this, XPS was also performed on $Pd(acac)_2$ and the results were compared to those for the exchanged catalyst. These results will be discussed in the section dealing with $Pd(acac)_2$.

The STEM/EDX results obtained on the catalyst after passage through the reactor were similar to the as prepared batch, suggesting that the larger particle structure seen in the bottom image of Figure 4.8 is primarily comprised of carbon. Sampling bias likely explains the slight differences, especially between the amounts of aluminum, but the trends are similar. It is likely that this carbon originates from the functionalizing ligands originally used to coat the bohemite.

XPS analysis was also carried out for the exchanged sample in a similar manner as was done for the impregnated. The near-surface composition is summarized in Table 4.4. Survey scans confirmed that Si was indeed present in the exchanged sample.

The small amount of Si detected via XPS was completely removed after sputter cleaning, indicating that Si was only present on the surface of the sample. This is somewhat contradictory to the EDX results since they suggest such a high level of Si and in light of the fact that EDX samples the bulk of the sample; not just the top 10 nm

Table 4.4 Surface composition exchanged catalyst.

atomic composition exchanged catalyst			
before sputtering		after sputtering	
element	atomic %	element	atomic %
Pd	0.1	Pd	0.3
Al	3.7	Al	2.0
C	82.0	C	92.6
O	13.5	O	4.5
Si	0.7	Si	-
Ar	-	Ar	0.5

or so like XPS, nonetheless the exchanged results still are useful for qualitative comparative purposes and hence their inclusion in this discussion is retained. XPS analysis done on the toluene that the sample was dissolved in revealed that this was the source of the contamination.

As before, sputter cleaning increased the signal coming from the palladium peak with a decrease in oxygen. The amount of carbon actually increased, with a decrease in aluminum. This suggests that the sample does not consist of Pd implanted bohemite particles, as was the case for the impregnated sample. When comparing the survey scans of the two samples, exchanged and impregnated, it is notable that for the exchanged catalyst, the carbon signal dominates the spectra even after sputtering, and the amount of palladium is also much lower as compared to the impregnated catlayst. As seen in Table 4.4, carbon comprises 91 % of the surface composition while palladium makes up less than one percent. From these results, it seems that the impregnated method of introducing palladium into the alumoxane is much more effective than the exchanged.

Figure 4.10 (top) shows the high resolution Pd 3d scan of the exchanged catalyst. As before, the figure contains plots of the raw, fit and overall fit data. Here, two components to the Pd $3d_{5/2}$ peak could be fit to the raw data: one at 336.4 eV and another at 337.8 eV; unlike the impregnated catalyst, four peaks could not be made to fit under the constraints described previously. As was mentioned earlier, there was a possibility that the palladium acetylacetonate used to exchange the palladium into the bohemite particles, was not fully exchanging. To help assign the fit peaks for the exchanged catalyst, XPS analysis was also done on the palladium signal from
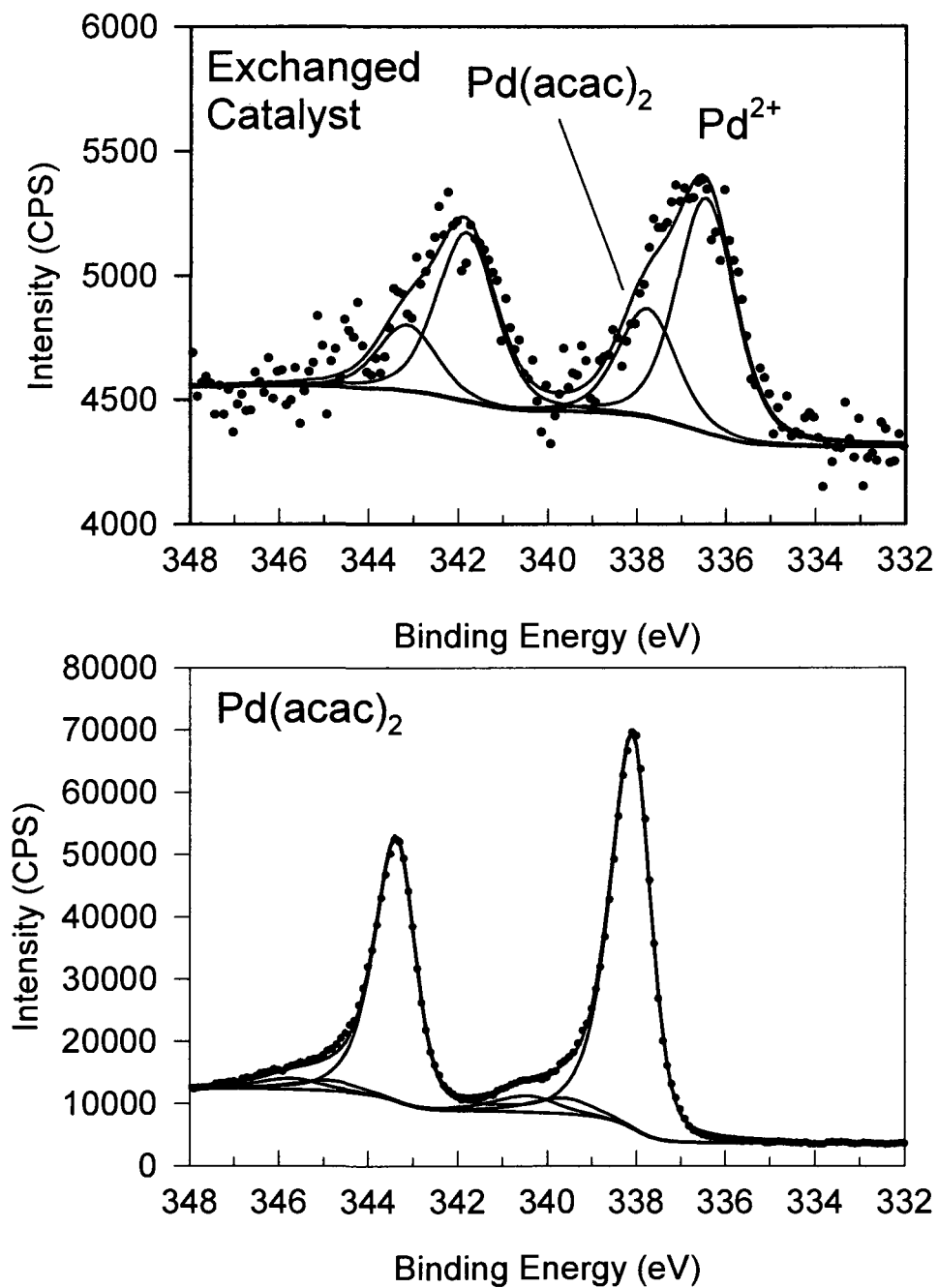
Figure 4.10 XPS spectra. Exchanged catalyst (top), Pd(acac)₂ (bottom).

palladium acetyl acetonate. Three peaks were fit to the Pd 3d signal: one at 338.1 and two other, much smaller, peaks at 340.4 and 339.6, as shown in the bottom part of Figure 4.10. With these values, as well as those obtained from the impregnated sample, we can assign these peaks. The peak at 336.8 eV is within the range of literature values for Pd^{2+}, most likely from PdO. This matches well with the Pd^{2+} in the impregnated sample. The most intense peak coming from the Pd 3d signal from the Pd(acac)$_2$ sample lies at 338.1 eV, fairly close to the position of peak two in the exchanged sample. Taken together with the earlier information which indicated incomplete exchange between the Pd(acac)$_2$ and boehmite particles suggests that Pd(acac)$_2$ is indeed still present in the exchanged sample.

Considering the implications of the data on the activity of the exchanged catalyst, it seems clear that the overall reduced amount of palladium and especially the reduced amount on the surface of the sample play a large role in explaining its relative lack of catalytic efficiency, as compared to the impregnated sample. Furthermore, it seems as if the original intent with the sample, to exchange Pd into the bohemite particles was largely unsuccessful. One advantage here seems to be that the Pd was better dispersed as compared to the impregnated sample. Unfortunately, much less of the Pd was available at the surface.

4.4.4 Pd(acac)$_2$ catalyst

Turning to a well-dispersed catalyst, the Pd(acac)$_2$ sample showed the most activity towards catalyzing combustion of all three samples. This activity prompted the same battery of characterization tests that were run for the exchanged and impregnated samples. As the results were fairly straightforward, they are omitted with the exception

of a brief summary. Microscopy results showed that the particles were highly dispersed, Pd rich and relatively small, with an average diameter around 5 nm. Typical results are shown in Figure 4.11. As discussed above, XPS showed the Pd in the sample to mostly be in a highly electron deficient state.

All of the above data, high surface area and dispersion, extremely active form of the catalytic metal, give reason for its substantial activity. One potential problem with this catalyst is its deactivation at higher temperatures, as seen in Figure 4.4. It is likely that this is due to a reduction of the metal. In this respect, the impregnated and exchanged samples show an advantage over Pd(acac)$_2$ as they remain active at higher temperatures as shown in Figure 4.3. In these cases it is possible that the bohemite support is serving as a source of oxygen to reactivate the metal.

4.5 Conclusions

Of the three catalysts studied, the Pd(acac)$_2$ catalyst was most active towards initializing combustion with onset temperatures reduced by almost 500° C over the noncatalytic case. This was a full 200° C lower than that for the impregnated catalyst and 300° for the exchanged sample, at equivalent Pd loadings. The Pd(acac)$_2$ sample consisted of particles that were highly dispersed, and had a narrow size distribution centered around 5 nm. At higher temperatures, over ~800° C, the impregnated sample was more active.

Particle characterization showed that the impregnated sample consisted of ~200 nm oleic acid functionalized bohemite particles, impregnated with palladium through use of a Pd containing salt. The surface of the particles showed higher amounts of palladium relative to the exchanged sample, and most of it was in highly electron
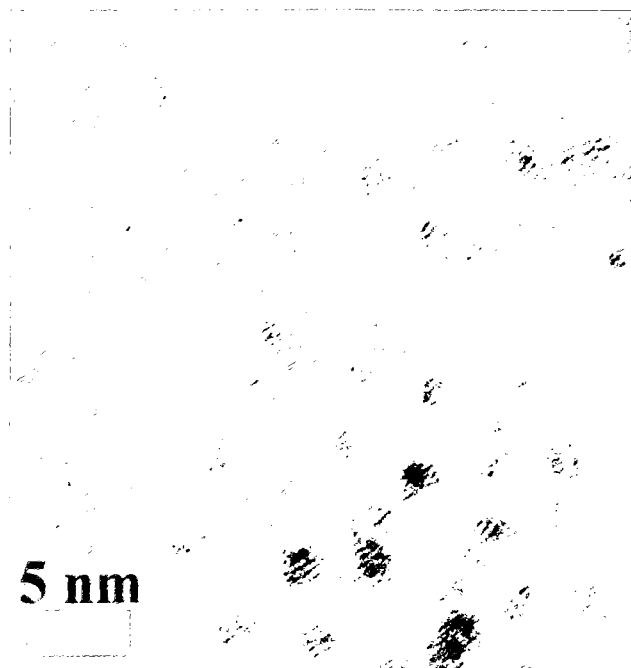
Figure 4.11 Hi-res TEM images, Pd(acac)2 sample; (top) collection of particles,

(bottom) individual particle.

deficient states advantageous for potential catalytic sites. The exchanged sample was seen to consist mainly of a carbonaceous matrix, with silica contamination and much smaller amounts of surface palladium than in the impregnated sample. Post combustor analysis showed a tendency for the particles in the impregnated and exchanged samples to aggregate while passing through the flow tube.

4.6 References

(1) Lewis, M. J. *Journal of Propulsion and Power* **2001**, *17*, 1214.

(2) Ciuparu, D.; Lyubovsky, M. R.; Altman, E.; Pfefferle, L. D.; Datye, A. *Catalysis Reviews - Science and Engineering* **2002**, *44*, 593.

(3) Wang, J. L., Yang; Zhang, Xiangwen; Mi, Zhentao; Wang, Li. *Catalysis Communications* **2009**, *10*, 1518.

(4) Wang, H. S., T.; Wickham, D.; Engel, J.; Nabity, J.;. *Combustion and Flame* In press.

(5) Kareiva, A. H., b C. Jeff; MacQueen, D. Brent; Cook, Ron; Barron, Andrew R. *Chemistry of Materials* **1996**, *8*, 2331.

(6) Edwards, T.; Maurice, L. Q. *J. Propul. Power* **2001**, *17*, 461.

(7) Hughes, A. E.; Sexton, B. A. *Journal of Electron Spectroscopy and Related Phenomena* **1990**, *50*, C15.

(8) Lu, W.; Komvopoulos, K. *Applied Physics Letters* **2000**, *76*, 3206.

(9) Powell, C. J. *Applied Surface Science* **1995**, *89*, 141.

(10) Moulder, J. F.; Stickle, W. F.; Sobol, P. E.; Bomben, K. D.; J. Chastain & R. C. King, J., eds. *Handbook of X-ray Photoelectron Spectroscopy*; Physical Electronics: Eden Prarie, MN, 1995.

(11) Powell, C. J.; Jablonski, A. *NIST Electron Effective Attenuation Length Database Version 1.1*Gaithersburg, MD, 2003.

(12) Hufner, S. W., G.K. *Physical Review B* **1975**, *11*, 678.

(13) McCarty, J. G. *Catalysis Today* **1995**, *26*, 283.

(14) Lyubovsky, M. P., Lisa *Catalysis Today* **1999**, *47*, 29.

(15) Williams, D. B.; Carter, C. B. *Transmission Electron Microscopy-A Textbook for Materials Science*; Plenum Press: New York and London, 1996.

(16) Katakura, R.; Yoshihiro, K. *Chemistry Letters* **2005**, *34*, 1448.

CHAPTER 5

IN SITU GENERATION OF Pd/PdO NANOPARTICLE METHANE COMBUSTION CATALYST FROM A FUEL-SOLUBLE ORGANOMETALLIC PRECURSOR.

The bulk of this chapter contains material from previously published article in The Journal of Physical Chemistry C. It is reproduced, in part, with permission from B. Van Devener, S.L. Anderson, T. Shimizu, H. Wang, J. Nabity, J. Engel, J. Yu, D. Wickham, S. Williams, Journal of Physical Chemistry C, 113, 20632-20639, 2009. Copyright 2009, the American Chemical Society.

While I was responsible for the majority of the work contained within this chapter, nanoparticle generation and methane combustion experiments were performed by Professor Hai Wang, University of Southern California, Department of Aerospace and Mechanical Engineering, and by TDA Inc., Wheat Ridge, CO. A brief discussion of these topics is included for clarity.

5.1 Overview

Decomposition of a fuel-soluble precursor was used for in situ generation of Pd/PdO nanoparticles, which then catalyzed ignition of the methane/O_2/N_2 flow. The composition, structure, and surface chemical state of the particles were determined by a combination of high resolution transmission electron microscopy (HRTEM), electron diffraction, scanning transmission electron microscopy/energy dispersive x-ray spectroscopy (STEM/EDX), and x-ray photoelectron spectroscopy (XPS). The particles were found to be primarily crystalline, metallic Pd, in a narrow size distribution around 8 nm. The ignition temperature was lowered ~150 K by the catalyst, and we present evidence that ignition is correlated with formation of a sub-nanometer oxidized Pd surface layer at higher temperatures.

5.2 Introduction

Supported palladium is used as a catalyst for methane combustion, with the metal being supported in fixed-bed reactors. The complex kinetics of Pd oxidation and its relation to the catalytic activity have been reviewed recently.[1] More recently, Pd-based catalysts have been proposed to improve performance of hypersonic propulsion platforms. Cryogenic methane has been proposed as a viable fuel because of its high density and specific energy content in comparison to hydrogen and jet fuels, and low tendency toward coke formation.[2] Catalysts are needed both to enhance and control endothermic reactions in the fuel system for thermal management,[3] and to enhance ignition and combustion rates in supersonic engines. For the combustion part of the problem, the typical fixed-bed catalytic reactor approach is not possible because of the high flow velocities required. One proposed solution is to use fuel-soluble

catalysts or catalyst precursors, and inject them into the combustor with the fuel, generating a highly dispersed, unsupported catalyst *in situ*.

Here we present results for *in situ* generation of Pd nanoparticles from a fuel-soluble organometallic precursor, and the correlation between particle properties and catalytic ignition of methane in a laminar flow reactor. The questions addressed are the nature of the Pd-containing species produced in the combustion environment, the nanoparticle formation mechanism, and the relation to the observed ignition behavior. One of the main questions is the oxidation state of the Pd, which has been shown to strongly affect activity for methane combustion.[1,4-6]

There have been a number of previous experiments using organometallic precursors in a combustion environment for nanoparticle synthesis. For example Nasibulin et al. have demonstrated nanoparticle synthesis using $Cu(acac)_2$ (copper (II) Acetylacetonate) entrained in a N_2/O_2 flow and passed through a flow tube reactor, whereupon the organic ligands were burned off leaving behind a vapor of Cu, which then condensed to form copper oxide nanoparticles.[7] Similarly, Strobel et al.[8] sprayed a mixture of Pd, La, and Al-containing organometallic precursors into a methane/air flame to generate catalyst particles consisting of < 5nm Pd particles supported on larger La_2O_3/Al_2O_3 nanoparticles. In the previously mentioned work, the catalyst was collected and used in a supported fixed bed configuration. Here we focus on unsupported catalyst nanoparticles formed and used *in situ*. This report focuses on the particle properties and how they correlate with reactor conditions and ignition. The kinetics of the combustion reactions, including both homogeneous chemistry and

catalytic reactions on the particle surfaces, are reported elsewhere, along with further details regarding the flow reactor.[9]

5.3 Experimental

Figure 5.1 shows a schematic of the reactor. Briefly, it consists of a quartz tube (94 cm long, 1.7 cm ID) that passes through a tube furnace that can reach temperatures of 1200° C, monitored by K-type thermocouples mounted on the outside of the quartz tube. Temperatures measured in the gas flow under reacting conditions are typically ~100° C lower than those for the reactor wall. Palladium was introduced as a toluene solution of palladium-2,2,6,6-tetramethyl-3,5-heptanedione ($Pd(THD)_2$), dispersed in N_2 as micron size droplets by a cooled, concentric nozzle atomizer. After passing several impactors, designed to remove large droplets, the droplet stream was mixed with a pre-mixed N_2, O_2 and CH_4 flow and entered the flow tube reactor.

Total reactor pressure was ~ 1 atm, and residence time at the temperatures of interest was ~1 second. Products exiting the reactor were diluted 8:1 in cold nitrogen gas in order to quench the reaction and minimize post reactor changes in the particle size distribution by aggregation. The concentrations of the $Pd(THD)_2$ precursor in toluene were 12000 ppm for all samples, and the catalyst loading in the gas flow was 1672 and 1687 $\mu g/g_{CH4}$ for the 500 and 700° C reactor runs, respectively. The concentrations of CH_4 and CO_2 at the exit of the reactor were continuously monitored using an NDIR gas analyzer (California Analytical Instruments Model 200), which withdraws 2 L/min of the diluted exhaust gas. The size distributions of particles at the exit were measured using a scanning mobility particle sizer (TSI SMPS 3090). The
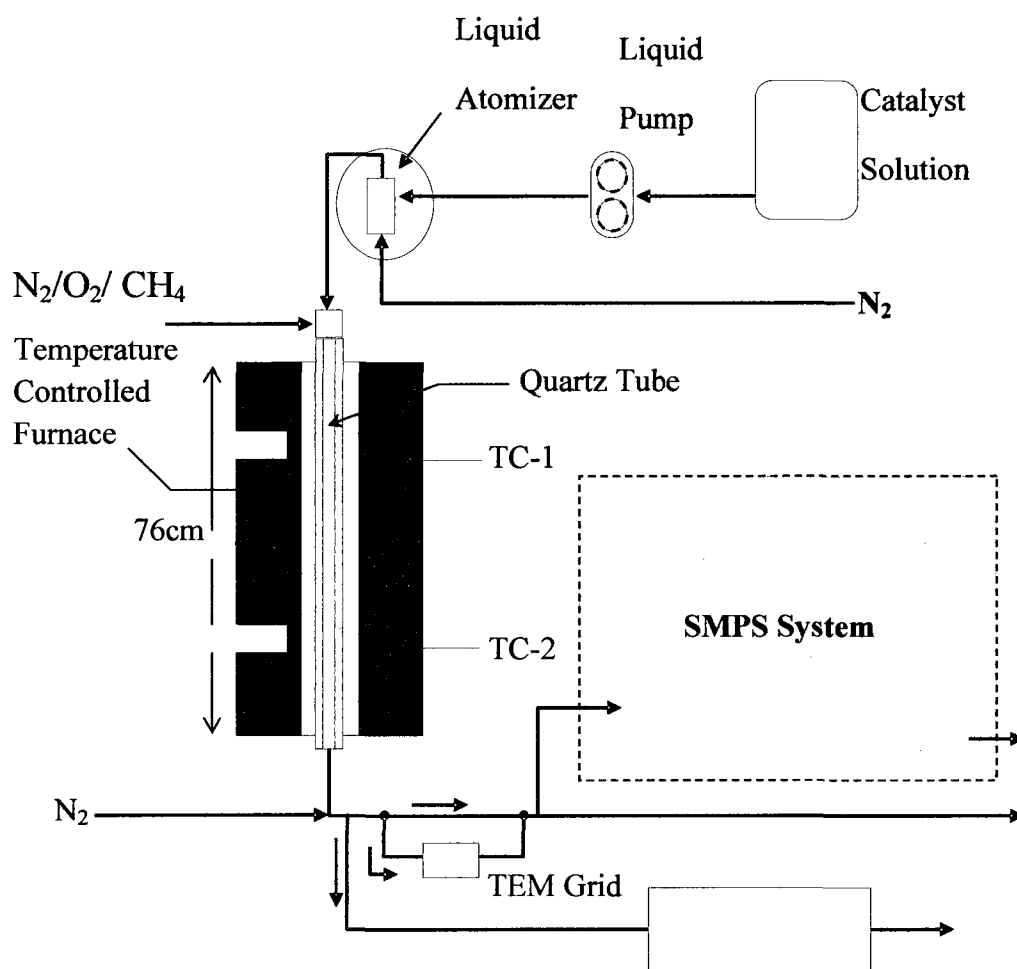
Figure 5.1 Schematic of the furnace reactor.

residence time from the reactor exit to the SMPS inlet was 0.6 sec. The particle size distribution was scanned over the range from 4.53 to 160 nm in diameter.

Particles were also collected on grids (Electron Microscopy Science HC200-CU) by exposing grids to the diluted exhaust flow, flowing parallel to the grid surface. The linear flow rate of the aerosol was 13 m/s over the grid. Under this condition, the flow is turbulent and the principal mechanism of particle collection is diffusion of the particles across the laminar boundary layer near the surface. As will be discussed below, diffusion mediated collection biases against large particles, since the particle diffusivity is inversely proportional to the diameter squared.

High resolution transmission electron microscopy (HRTEM) and selected area electron diffraction (SAED) was done using an FEI Technai F30 at 300 keV beam energy. Scanning transmission electron microscopy (STEM) analysis was performed on an FEI Technai F20 operated at 200 keV, with a high angle annular dark field (HAADF) detector. The STEM was also used for energy dispersive x-ray (EDX) analysis of elemental compositions. Spectra were background subtracted, integrated, and converted to elemental compositions using k-factors supplied by EDAX Inc. X-ray photoelectron spectra (XPS) were collected using the monochromatic Al Kα source (1486.7 eV) on a Kratos Axis Ultra DLD instrument.

5.4 Results and discussion

There are several general points to be made before discussing the particle properties. As the N_2 flow in which the Pd(THD)$_2$/toluene aerosol is entrained mixes with the main $CH_4/O_2/N_2$ flow, and enters the heated section of the reactor, the aerosol droplets are expected to evaporate rapidly (b.p. toluene = 111° C, $T_{sublimation}$ Pd(THD)$_2$

$\approx 150^\circ$ C), releasing the Pd(THD)$_2$ vapor into the flow. Pd(THD)$_2$ is a weakly bound coordination complex, expected to decompose at relatively low temperatures, releasing Pd atoms into the flow. As will be shown below, the Pd atoms nucleate to form nanoparticles, which catalyze ignition of the methane at 600° C gas temperature (700° C wall temperature).

The Pd/toluene precursor solution is introduced into the reactor inlet in the form of a micron sized aerosol carried by a nitrogen gas flow. At the inlet, this flow is mixed with a premixed CH$_4$/O$_2$/N$_2$ stream as indicated in Figure 5.1. Once inside the inlet of the reactor, the aerosol quickly evaporates leaving behind a vapor of the Pd precursor. Heating leads to precursor dissociation, which releases Pd atoms or clusters. When atom or cluster concentrations reach high enough levels, the Pd nucleates into small clusters, which subsequently undergo both size and mass growth due to particle coagulation and surface condensation. At some point in the reactor, the surfaces of the nanoparticles become catalytically active, after which catalytic oxidation of the gas mixture would take place leading to fuel ignition. CH$_4$ and CO$_2$ concentrations are measured to monitor fuel ignition.

One question is whether Pd(THD)$_2$ decomposition is fast enough at the temperatures of interest, so that nanoparticle growth is complete, or nearly so, before the exit of the flow tube. We note that the nanoparticle size distribution is, essentially, independent of reactor temperature from at least $500 - 800^\circ$ C. If the Pd(THD)$_2$ decomposition rate were a significant factor controlling nanoparticle nucleation and growth, we would expect the particle size distribution to change significantly over such a broad temperature range.

When methane ignition occurs, the gas temperature in the flow tube spikes well above the wall temperature. Because we are interested in understanding the formation mechanism of the nanoparticles under known temperature conditions, particle collection was carried out in separate experimental runs, omitting the CH_4 fuel, but otherwise keeping conditions identical to the reactive runs. Particles were collected for two different reactor temperatures, just below and above the temperature where ignition is observed when CH_4 is present.

5.4.1 Catalytic ignition

Catalytic ignition measurements were performed by Professor Hai Wang and his group members at the University of Southern California. A brief summary of their results is presented for clarity and to aid in the interpretation of the work I carried out.

Figure 5.2 shows the variations of CH_4 and CO_2 concentrations exiting the furnace, plotted as a function of the furnace temperature. Three cases are shown. Non-catalytic run 1 shows results obtained under conditions of no Pd particle loading. It can be seen that at the ignition point, the amount of CH_4 drops off rapidly while that of CO_2 rises. Noncatalytic methane ignition occurs at a furnace temperature of around 1100 K, which corresponds to a maximum gas temperature of approximately 950 K along the centerline of the reactor.

Runs 3 and 4 show the results of catalyzed ignition, with the only difference between the runs being catalyst loading; 4.3×10^{-4} and 4.7×10^{-4} moles Pd/mole CH_4 for runs 3 and 4, respectively. The use of the in situ generated catalyst reduces the
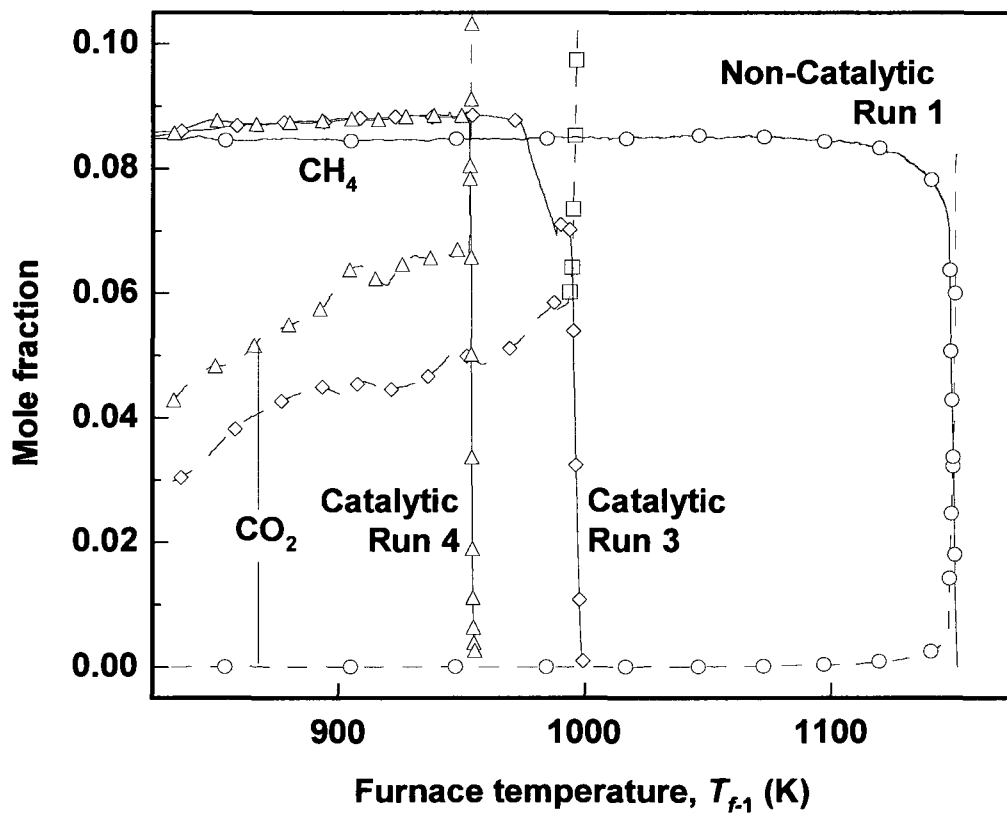
Figure 5.2 CH_4 and CO_2 mole fractions as a function of the furnace temperature of Zone I, $T_{f\text{-}1}$.

Reproduced with permission from T. Shimizu, A.D. Abid, G. Poskrebyshev, H. Wang, J. Nabity, J. Engel, J. Yu, D. Wickham, B. Van Devener, S.L. Anderson, and S. Williams, Combustion and Flame, submitted for publication, 2009. Unpublished work copyright 2009, Elsevier B. V.

ignition temperature by 150 K. In the catalytic case, the rise of the CO_2 mole fraction before ignition is due to toluene oxidation. Tests done under conditions of no catalyst loading but with toluene addition showed that it did not affect methane ignition.
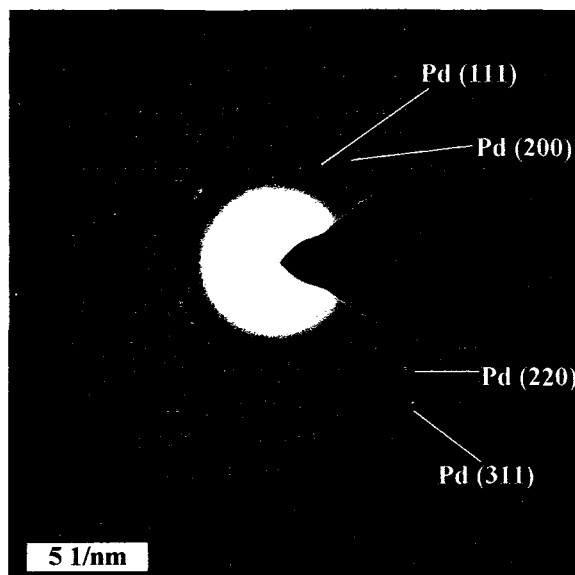
5.4.2 After passage through the reactor at 500° C

The large area TEM image in Figure 5.3 shows particles collected after passage through the flow reactor at 500° C. No ignition was observed at this temperature (i.e., with methane in the flow), at any catalyst concentration examined. Even at low resolution, it can be seen that the larger particles are simply aggregates of smaller primary particles. Aggregates can form both in the gas-phase prior to deposition, and on the surface as particles are deposited. The spatial uniformity of particles collected over the area is indicative of particle deposition by a diffusion mechanism. The lower frame of Figure 5.3 shows the corresponding size distribution of the primary particles, i.e., measurements of the aggregates were done on the individual particles comprising them; within the resolution limit. Most of the particles are between 5 and 10 nm in diameter with an average size of 8.3 nm. The size distribution extracted from the TEM image is shifted to smaller sizes, compared to the distribution obtained via SMPS, here the mean mobility particle diameter was 24 nm. There are two contributors to the difference. SMPS samples the entire particle distribution, whereas for TEM analysis, particles were collected via diffusion to the grid, which introduces a bias against the larger particles. Furthermore, in the TEM distribution we separately measured the individual particles making up aggregates, whereas in SMPS such aggregates are counted as a single particle.
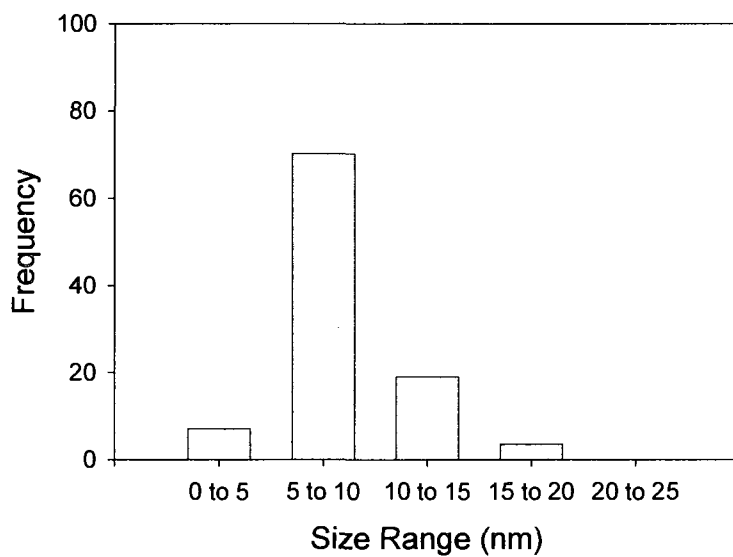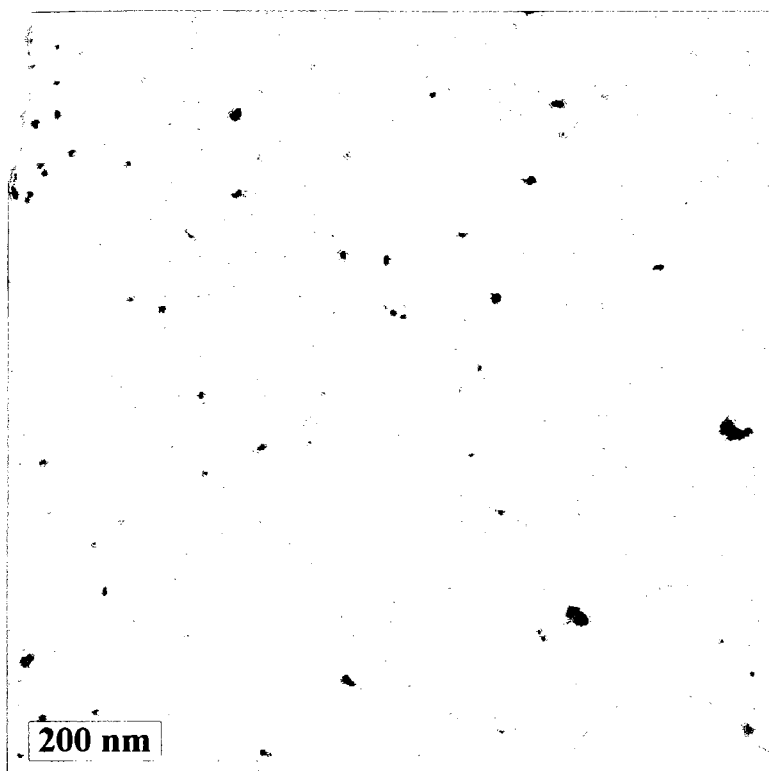
Figure 5.3 (Top) Low magnification TEM image of Pd(THD)₂ catalyst after passage

through reactor at 500° C; (Bottom) corresponding size distribution.

The selected area electron diffraction (SAED) pattern measured for this sample is shown in Figure 5.4. The brightest diffraction ring is closest to the center, typical of fcc materials.[10] Assigning the rings to particular lattice vectors must be done with caution because nano-scale particles can have significantly different lattice parameters than bulk material, due to the large fraction of atoms at surfaces and grain boundaries. Fortunately, a study by Penner *et al.* on 5 to 10 nm Pd and PdO nanoparticles showed no significant changes in lattice parameters compared to the bulk materials.[11] Table 5.1 summarizes the distances extracted from the SAED, together with assignments and reference values from the literature.[11,12] The experimental values represent the average of several measurements, all which had a variance of less than 1 %. Note the close match (< 0.5% deviation) between most of the experimental distances and lattice parameters for Pd metal. The two short distances (1.120 and 0.893 Å) correspond to the very faint and diffuse outer rings, and we have not been able to assign them. Under the conditions of particle formation (500° C, oxidizing conditions), PdO is thermodynamically favorable[13]; thus we looked carefully for evidence of PdO. The table also gives the PdO lattice distances that best match the experimental distances, and it can be seen that overall pattern is much better matched by metallic Pd.

Typical high resolution images, shown in Figure 5.5 a and b, indicate a more complicated particle structure than that suggested by electron diffraction. Figure 5.5 a shows a typical primary particle, roughly ~10nm in diameter with well developed lattice fringes. The 2.28 Å lattice spacing clearly corresponds to the spacing between Pd (111) planes (Table 5.1). This same spacing is seen in high resolution images of most particles examined. The slight discrepancy in the distance measured from the

Figure 5.4 SAED pattern for Pd(THD)$_2$ catalyst after passage through reactor at
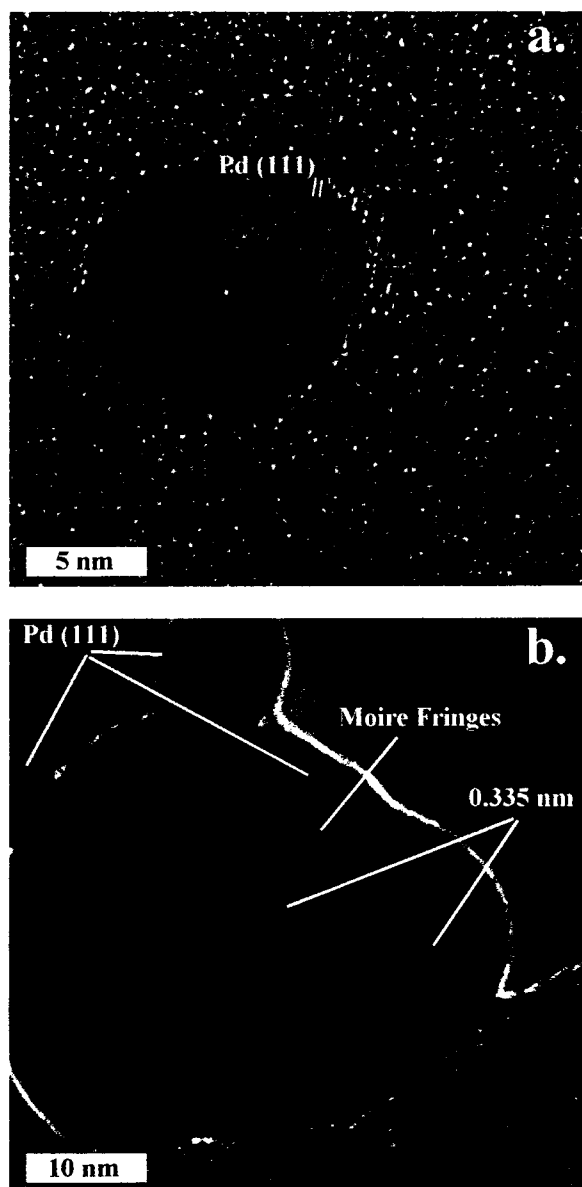
500° C.

Table 5.1 Comparison of SAED results with literature.

exptl. data and assignments			Pd^a		PdO^a		SiO$_2$^{b}			
d(Å) 500°	d(Å) 700°	lattice plane	d(Å)	lattice plane	d(Å)	lattice plane	d(Å)	lattice plane	d(Å)	lattice plane
2.234	2.245	Pd(111)	2.246	(111)	3.046	(100)	4.257	(010)	3.350	(002)
1.943	1.957	Pd(200)	1.945	(200)	2.667	(002)	3.342	(011)	1.675	(102)
1.369	1.370	Pd(220)	1.375	(220)	2.644	(101)	1.818	(112)	1.541	(103)
1.173	1.170	Pd(311)	1.173	(311)	2.153	(110)				
1.120	-	-			1.674	(112)				
0.893	-	-			1.536	(103)				
					1.522	(200)				
					1.335	(004)				
					1.332	(202)				

^{a} Values of d and assignments for Pd and PdO taken from Penner *et al.* (**11**)

^{b} Values of d and assignments for SiO$_2$ and graphite from Roberts *et al.* (**12**)

Figure 5.5 HRTEM images of Pd(THD)$_2$ catalyst after passage through reactor at 500°

C. (a) Small particle with Pd(111) lattice fringes; (b) group of particles with Moiré

interference.

images is simply measurement error. The spacing was measured by averaging the distances between successive peaks in the contrast profile taken along a line perpendicular to the fringes. Pixelation at the 800 k magnification used in the image results in some error in this measurement. Nevertheless, the discrepancy is small and the assignment is clear. A similar small discrepancy is seen when comparing other distances from the images with the SAED results.

Figure 5.5 b shows a ~30 nm particle with more complex structure. In addition to the two attached ~10 nm particles, both indexed to Pd(111), the main body of the larger particle shows two different sets of fringes: one with d-spacings of 2.28 Å and another with d-spacings of 3.35 Å. 2.28 Å is just Pd(111) appearing again, but 3.35 Å is not a good fit to any Pd or PdO index. The most likely assignment is to either graphite or SiO_2 (see below), as indicated in Table 5.1.

Moiré fringes are also apparent in the upper-right region of the main particle, indicating interference from two different sets of overlapping fringes. The obvious assignment would be to relate Moiré fringes to interference between the 2.28 Å and 3.35 Å spacings, however, observations made by Datye et al.[14] suggested that we should consider an alternative. They observed Moiré patterns resulting from interference between PdO(110) and Pd(200) planes in their study of Pd nanoparticles on alumina supports. Given that PdO is thermodynamically favored under conditions of this experiment,[15] such interferences might provide evidence that the particles are at least partly oxidized, despite lack of direct evidence in the SAED or HRTEM images. A general expression[10] for Moiré fringes caused by a combination of translational and

rotational displacements of two overlapping lattices, was used to calculate the range of possible Moiré spacings that could result from Pd and PdO lattices:

$$d_{gm} = \frac{d_1 d_2}{\sqrt{(d_1 - d_2)^2 + d_1 d_2 \beta^2}}$$

Here, d_{gm} is the spacing of the Moiré fringes, d_1 and d_2 are the spacing of the two interfering planes, and β is the angle between the planes. We examined all possible permutations of low index lattice planes from all species present or possibly present in the samples (Pd, PdO, graphite, SiO_2), and Table 5.2 summarizes only the best few fits to the observed spacing (16.5 Å). The best match (3% error) is an interference between Pd(200) with SiO_2(112). The best match for Pd/PdO is the Pd(200)/PdO(110) overlap identified by Datye et al., however, the error is significantly worse (7.5%). We also used this approach to see how well we could fit the Moiré fringe spacing observed by Datye et al. (estimated by us from figure 10 of the Datye paper[14]) to an interference between PdO(110) and Pd(200). As indicated in Table 5.2, the best fit differs from the estimated experimental spacing by ~13%.

SAED and TEM fringes confirm the presence of metallic, crystalline Pd nanoparticles. STEM measurements using a HAADF detector coupled with small spot EDX were made to look for other constituents of the sample. Figure 5.6 shows three STEM images with corresponding atomic composition data for the indicated analysis areas summarized in Table 5.3. Image A shows a cluster of particles. With the HAADF detector, bright areas correspond to regions that are either thicker, or contain higher concentrations of high Z elements, or both. Note that there are three distinct brightness levels present in the image. There appears to be a very diffuse material that extends over much of the image, well outside the EDX analysis area indicated by the

Table 5.2 Moiré fringe measurements.

possible interfering planes	this work d_{gm} measured 16.5 d_{gm} (Å) calculated	Datye et al.[a] d_{gm} measured 23.3 d_{gm} (Å) calculated
Pd(200)/SiO2	17.0	-
Pd(200)/PdO(110)	15.3	20.1
Pd(111)/Pd(101)	13.2	-
Pd(111)/PdO(200)	12.4	-

[a] Measured and calculated values are based on figure 10 from Datye et al. (**14**)
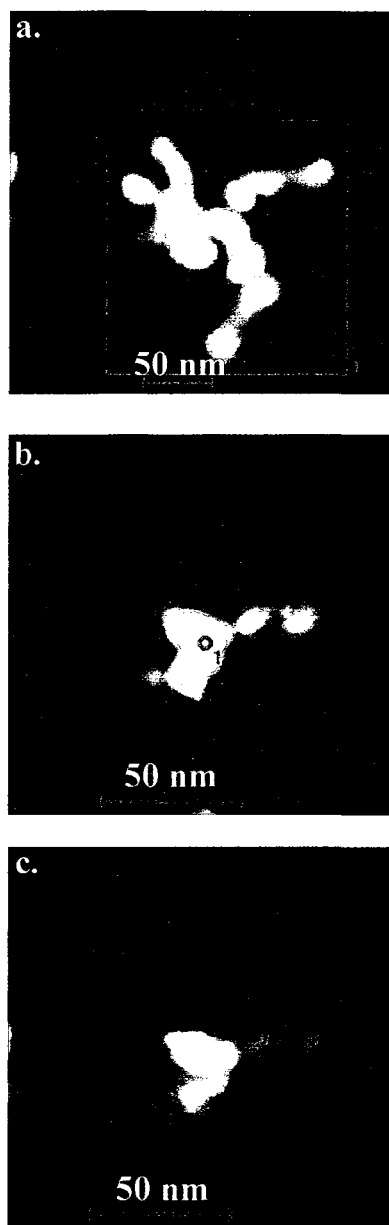
Figure 5.6 STEM/HAADF images of (THD)₂ catalyst after passage through reactor at 500° C. (a) Lower magnification overview of a cluster of particles, corresponding atomic composition taken from area within box shown below; (b) higher magnification image of another group of particles, spectrum taken on center of particle; (c) same group of particles as in (b), spectrum from edge of particles.

Table 5.3 XEDS results.

XEDS atomic composition					
image A		image B		image C	
element	atomic %	element	atomic %	element	atomic %
Pd(K)	2.4	Pd(K)	21.2	Pd(K)	-
O(K)	13.2	O(K)	6.9	O(K)	17.0
C(K)	70.6	C(K)	58.4	C(K)	56.6
Si(K)	12.4	Si(K)	7.1	Si(K)	25.3
Cu(K)	1.5	Cu(K)	6.3	Cu(K)	1.0

rectangular border. Inside the border, there is a collection of higher brightness areas, indicating an aggregate of particles. Note, however, that even with the grouping of particles, there are two distinct brightness levels. The highest contrast areas range from ~5 nm to ~20 nm in size, and these appear to be superimposed on larger 20 - 30 nm particles of intermediate brightness. Spectral analysis of the area inside the border, which includes areas with all three brightness levels, shows a large concentration of carbon and a small amount of Cu, both presumably from the Cu-supported holey carbon TEM grid. Pd and O are present, as expected, but there is also a substantial signal for Si, and much more O than could be accounted for even if the particles were solid PdO.

Image B shows a higher magnification image of another group of particles, with the EDX spectrum taken from a small spot in the center of the brightest particle, as indicated by the red circle. Other than C and Cu from the TEM grid, this spot is composed of mostly Pd, with O and Si both present at about $1/3^{rd}$ the Pd concentration. Image C shows the same particle aggregate as in B, but with the EDX analysis area chosen to sample one of the intermediate contrast regions near the edge of the aggregate. Lower contrast could indicate a part of the aggregate that is simply thinner, or a part where the concentration of high Z elements is lower. The EDX spectra show that the latter interpretation is correct. This region is Pd-free, and aside from C and Cu from the grid, is composed entirely of Si and O in a 1 to 1.5 ratio. To minimize sampling bias with the STEM/EDX work, analysis of several other particles and particle aggregates was carried out, with similar results.

The surprise in these images was the presence of Si-rich regions. The amount of Si in the spectra is far too high to be attributed to internal fluorescence from the dead layer of the detector,[10] and the O concentration seems to vary with the concentration of Si rather than Pd. Taken together with the HRTEM imagery, the conclusion is that the material exiting the reactor includes Pd-rich primary particles that are mostly crystalline, metallic Pd, some of which are aggregated with, or perhaps encapsulated by partially oxidized silicon.

We suspected that the source of the Si contamination was the toluene solvent used to dissolve the $Pd(THD)_2$ precursor. To confirm this, two control experiments were conducted with flow conditions identical to those above, and with TEM grids positioned to collect any nanoparticulate products. In one experiment, N_2 was flowed through a clean atomizer, then into the normal flow mixture in the reactor. In the second, pure toluene (J.T. Baker 99.7 % purity) was atomized in the N_2 entering the reactor. STEM/EDX analysis showed that with no toluene in the atomizer, essentially no particles deposited on the TEM grid, but with toluene in the atomizer, Si-rich material was deposited on the grid. It is unclear if the Si is a contaminant of the toluene or if toluene is dissolving Si from the glass atomizer. Experiments to examine the possible effects of this SiO_x contaminant on activity of the catalyst particles are planned.

5.4.3 After passage through the reactor at 700° C

Similar particle collection/analysis experiments were carried out for material produced in methane-free flows at a 700° C reactor temperature. This temperature is just above the point where catalytic ignition is observed in methane-containing flows,

thus comparison with the particles collected at 500° C is of interest in understanding the factors controlling ignition. At 700° C, it was further observed that there was a threshold concentration of Pd required for ignition, of ~4.5 x 10^{-4} Pd/CH$_4$. Figure 5.7 shows a large area TEM image of these particles with accompanying size distribution. As comparison with Figure 5.4 shows, both the appearance of the particles in the image and the extracted size distribution are nearly identical to the 500° C results.

Figure 5.8 a shows a characteristic SAED pattern for the 700° C sample, and 5.8 b shows a high resolution image of a typical small ~10 nm particle with lattice fringes. Both the diffraction spacings (Table 5.1) and the collection of images of particles formed at 700° C are similar to the analogous results for the 500° sample. In both cases, the crystalline portion of the samples is dominated by metallic Pd. STEM/EDX data were also collected for the 700° C sample, but since they are virtually identical to those obtained from the 500° C sample, representative data are included in Appendix B.

5.3.4 Summary of microscopy results

The microscopy data show that the size distribution of primary nanoparticles and the composition of the particles are similar for reactor temperatures above and below the ignition point. In all samples, the primary particles are primarily metallic Pd with a size distribution peaking at ~8 nm, some of which are aggregated with SiO$_x$ material. The dominance of Pd, rather than PdO, is somewhat surprising considering that PdO is the thermodynamically favored phase under the low temperatures and oxidizing conditions where the particles were formed. Given that PdO is also the more
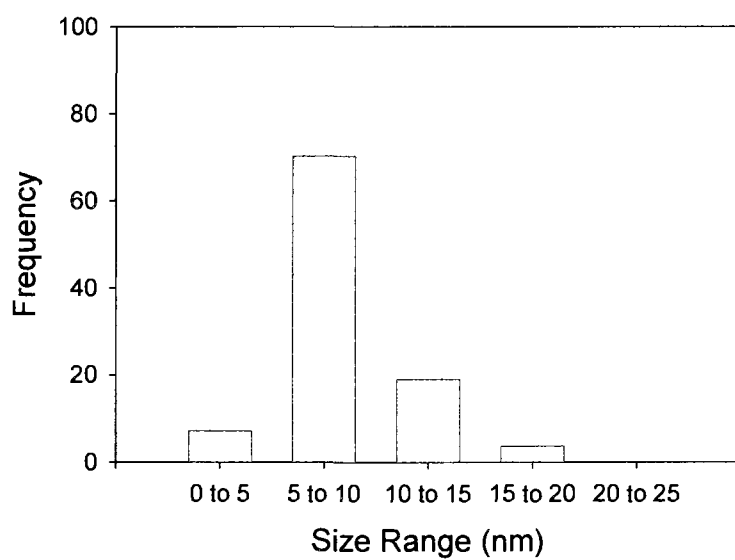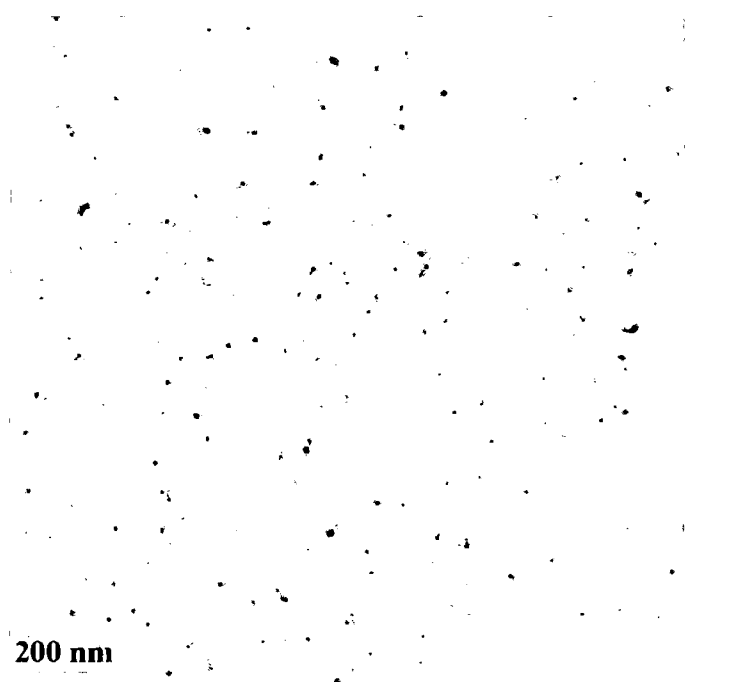
Figure 5.7 (Top) Low magnification TEM image of Pd(THD)$_2$ catalyst after passage

through reactor at 700° C; (Bottom) corresponding size distribution.
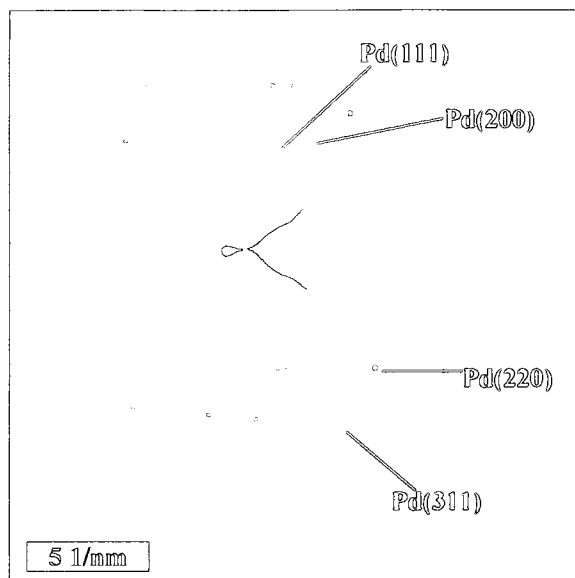
Figure 5.8 Top, SAED pattern for Pd(THD)$_2$ catalyst after passage through reactor at 700° C; bottom, typical small particle with Pd(111) fringes visible.

catalytically active state for methane combustion,[5] it seems worthwhile to examine the surface chemistry of the particles to see if it differs significantly from the bulk.

5.3.4 X-ray photoelectron spectroscopy

XPS is sensitive to the top few nanometers of the sample surface, providing a means to look for chemical modification of the particle surfaces. Figure 5.9 shows XPS spectra collected for both the 500° and 700° C samples. The samples were collected on TEM grids in the same manner as was done for the microscopy experiments, with the only difference being higher particle density, to obtain better signal-to-noise ratio to aid chemical state identification. The spectra were analyzed by subtracting a Shirley background, then fitting with Gaussian/Lorentzian functions.

In the 700° C spectrum, each fine structure component has three peaks, at 335.9, 337.4 and 338.7 eV for the main $3d_{5/2}$ component. The largest peak (335.9 eV) is in reasonable agreement with the literature binding energy $(335.7)^{[16]}$ for metallic Pd, and will be denoted Pd^0. Given the microscopy results, above, the obvious conclusion is that this Pd^0 signal represents the interior of the particles. The small shift from the literature value may result from sample charging, or possibly is a final state effect due to less efficient core hole screening in the nanoparticles as compared to bulk Pd. This phenomenon has been previously observed in a XPS study of small Pt and Pd clusters.[17] The smaller peak shifted 1.5 eV to higher binding energy is clearly from some oxidized Pd species, which we will denote Pd^{ox}. The shift of the Pd^{ox} peak is intermediate between the shifts expected for PdO $(336.9 \text{ eV})^{[18]}$ and PdO_2 $(337.7 \text{ eV}).^{[19]}$ The high binding energy region of the experimental peak is asymmetrically broadened, which was fit by adding a small peak at 338.7 eV. The origin of this high energy
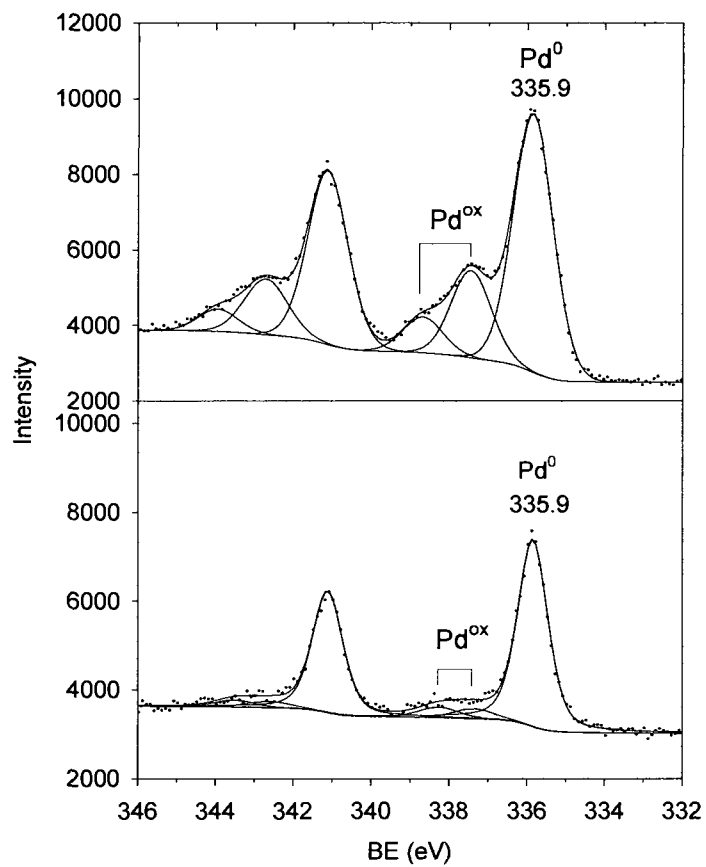
Figure 5.9 Pd 3d photoelectron spectra for particles passing through reactor at 700°
(top) and 500° (bottom).

broadening is not clear. Photoemission spectra of metal oxides often have shake-up features shifted to higher binding energies from the main peaks, and Militello *et al.* reported a shake-up satellite in their study of PdO powder.[20] However, they found the peak position of this satellite to be 339.8 eV – well above the energy of our high energy tail. It is also possible that the high energy peak results from a higher oxidation state of Pd, however, the energy extends well above the range expected for PdO_2. For the purposes of quantitating the amount of oxidized Pd present, we simply consider all intensity outside the metallic Pd peak to be oxidized Pd – Pd^{ox}.

Taking the XPS and TEM results together, it is clear that while the bulk of the nanoparticles formed at 700° C is metallic Pd, there is an oxidized surface layer. For the 500° C sample, the Pd^{ox} signal is barely detectable, indicating formation of much less surface oxide. It is possible to estimate the thickness of the oxide layer by modeling the ratio of Pd^{ox} to Pd^0 signals. The particles are small enough that the x-rays fully penetrate the sample, thus the detection sensitivity of material in different regions of the sample is determined by the electron detection probability. The effective attenuation length (EAL) of Pd photoelectrons in Pd (1.34 nm) and PdO (1.41 nm) can be estimated using the NIST Electron Effective Attenuation Length database program.[21] Electrons generated in different locations within a particle are detected with efficiency that decays exponentially with the path length (d) required to escape in the direction of the detector: exp(-d/EAL). We modeled the XPS intensities expected for a single spherical particle, and also for a randomly packed group of spherical particles. In each case, the particles were assumed to have ~8 nm diameter, and the thickness of the oxide layer was varied to fit observed ratio of the Pd^{ox}/Pd^0

XPS intensities. For either model, the Pd^{ox}/Pd^0 ratio is predicted to be ~2.4 times greater than it would be for a flat oxide-covered Pd surface. This enhanced sensitivity to the surface oxide results partly from the curvature of the particles, and partly from the fact that some signal from the far side of the particles penetrates through the bulk to be detected.

Based on the observed intensity ratios, the oxide layer is estimated to be ~0.36 nm thick for the 700° C sample, and 0.09 nm thick for the 500° C sample, assuming a uniform oxide layer over the particle surfaces. 0.36 nm corresponds to essentially one monolayer of oxidized Pd on the particle surfaces at 700° C, and partial monolayer coverage at 500° C. These oxidized Pd layers are too thin to observe in the TEM images, and are probably not ordered well enough to contribute to structure in the electron diffraction patterns.

5.5 Conclusions: catalyst particle formation and activation

Particles collected at the two different reactor temperatures had similar size distributions and particle morphologies with one important exception; those collected at catalytic temperatures showed a much greater extent of oxidation in XPS. Therefore, it seems reasonable to associate formation of the oxide with activation of the catalyst. Furthermore, the results suggest that the kinetics of Pd oxidation may play an important role in the time required to activate the catalyst formed by decomposition of precursors in the fuel. These results appear consistent with those of Datye *et al.*, where in their study of Pd/PdO particles on alumina supports prepared by calcination in air, they found that once a surface layer of PdO forms, it inhibits oxidation of the particle bulk.[14]

5.6   References

(1)   Ciuparu, D.; Lyubovsky, M. R.; Altman, E.; Pfefferle, L. D.; Datye, A. *Catalysis Reviews - Science and Engineering* 2002, *44*, 593.

(2)   Lewis, M. J. *Journal of Propulsion and Power* 2001, *17*, 1214.

(3)   Edwards, T. *Combust. Sci. Tech.* 2006, *178*, 307.

(4)   Farrauto, R. J.; Hobson, M. C.; Kennelly, T.; Waterman, E. M. *Applied Catalysis, A: General* 1992, *81*, 227.

(5)   McCarty, J. G. *Catalysis Today* 1995, *26*, 283.

(6)   Lyubovsky, M.; Pfefferle, L. *Catalysis Today* 1999, *47*, 29.

(7)   Nasibulin, A. G.; Richard, O.; Kauppinen, E. I.; Brown, D. P.; Jokiniemi, J. K.; Altman, I. S. *Aerosol Science and Technology* 2002, *36*, 899.

(8)   Strobel, R.; Pratsinis, S. E.; Baiker, A. *J. Materials Chem.* 2005, *15*, 605.

(9)   Shimizu, T.; Wang, H.; Nabity, J.; Engel, J.; Yu, J.; Wickham, D.; VanDevener, B.; Anderson, S. L.; Williams, S. *Combustion and Flame* Submitted.

(10)   Williams, D. B.; Carter, C. B. *Transmission Electron Microscopy-A Textbook for Materials Science*; Plenum Press: New York and London, 1996.

(11)   Penner, S.; Wang, D.; Jenewein, B.; Gabasch, H.; Klotzer, B.; Knop-Gericke, A.; Schlogl, R.; Hayek, K. *Journal of Chemical Physics* 2006, *125*, 094703/1.

(12)   Roberts, W. L.; Campbell, T. J.; Rapp, G. R. *Encyclopedia of minerals* 2nd ed.; Van Nostrand Reinhold: New York, 1990.

(13)   Rao, Y. K. *Stoichiometry and Thermodynamics of Metallurgical Processes*; Cambridge University Press: Cambridge, UK, 1985.

(14)   Datye, A. K.; Bravo, J.; Nelson, T. R.; Atanasova, P.; Lyubovsky, M.; Pfefferle, L. *Applied Catalysis, A: General* 2000, *198*, 179.

(15)   Bayer, G.; Wiedemann, H. G. *Thermochimica Acta* 1975, *11*, 79.

(16)   Hufner, S.; Wertheim, G. K. *Physical Review B* 1975, *11*, 678.

(17)   Cheung, T. T. P. *Surface Science* 1984, *140*, 151.

(18)   Barr, T. L. *J. Vac. Sci. Technol. A* 1991, *9*, 1793.

(19)   Briggs, D.; Seah, M. P. *Practical Surface Analysis*, second ed.; John Willey & Sons, 1993; Vol. 1.

(20)   Militello, M. C.; Simko, S. J. *Surface Science Spectra* 1997, *3*, 395.

(21)   Powell, C. J.; Jablonski, A. *NIST Electron Effective Attenuation Length Database Version 1.1*Gaithersburg, MD, 2003.

APPENDIX A

ADDITIONAL DATA FOR CHAPTER 3

A.1 Size distributions and surface analysis of ceria coated, oleic acid functionalized boron nanoparticles.

DLS and XPS measurements were also performed on ceria coated boron nanoparticles that had been functionalized with oleic acid. Figure A.1 shows the size distribution of the particles as obtained with DLS. As can be seen by comparison with the size of the particles for the sample milled without ceria in Figure 3.3, the size distributions are similar.

Figure A.2 shows the B 1s spectrum for boron milled with ceria and oleic acid. Data was analyzed as described in Chapter 3. Comparison with Figure 3.5, which shows the analogous spectrum for boron milled with ceria but without oleic acid, shows that the overall signal for the oleic acid coated sample is significantly attenuated, as would be expected. Furthermore, the relative amount of oxidized boron, as shown by the two higher binding energy peaks, is reduced in the case of the sample milled in the presence of oleic acid. This observation is consistent with the organic oleic acid layer serving to protect against oxidation. Presumably, the small amount of oxidation that is present occurs from the interaction of boron with CeO_2 prior to that with oleic acid.

Another example of STEM data of ceria coated boron nanoparticles is shown in Figure A.3, with EDX results summarized in Table A.1. The data were taken from one of several particles to avoid sampling bias and, as can be seen by comparison with Figure 3.6 and Table 3.3 in Chapter 3, the results are similar.
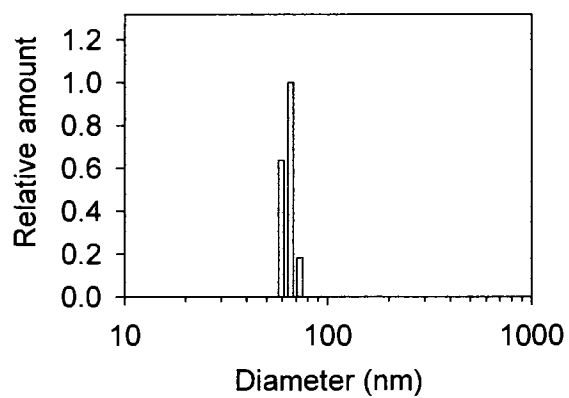
Figure A.1 DLS size distribution of ceria coated boron functionalized with oleic acid (peaked at 66 nm).
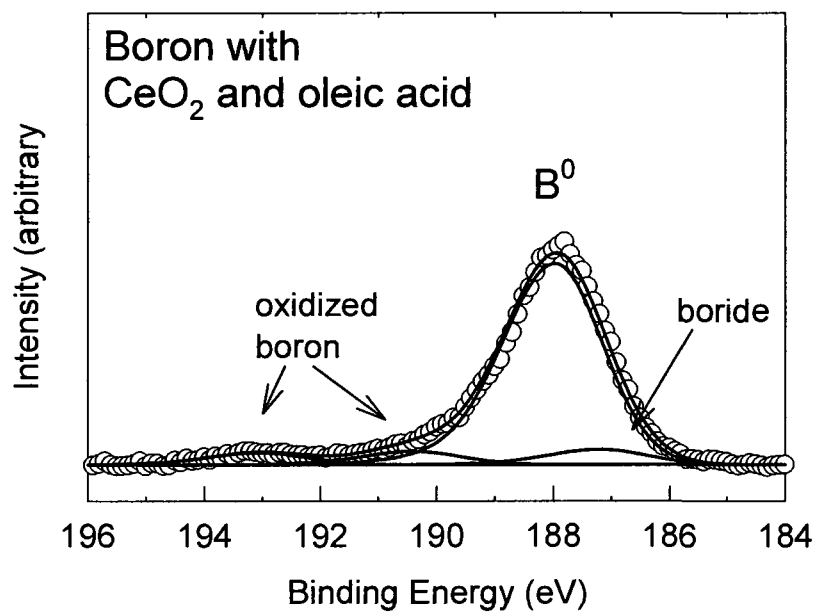
Figure A.2 B 1s XPS spectrum for boron milled with ceria and oleic acid.
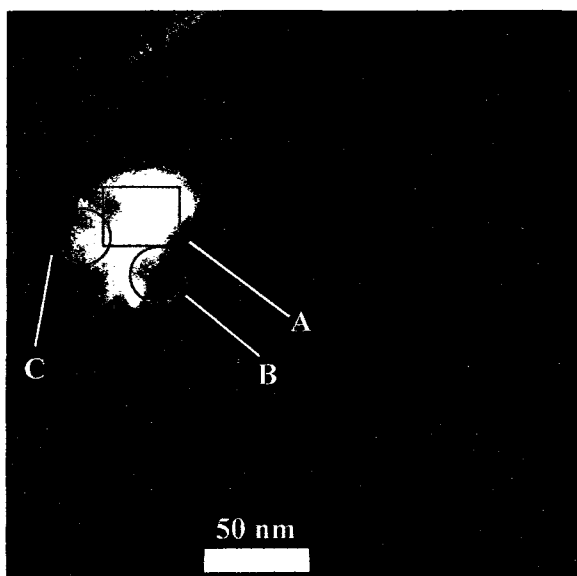
Figure A.3 Additional STEM/HAADF image of ceria coated boron particles.

Table A.1 EDX results for Figure A.3.

EDX atomic composition								
area A			area B			area C		
element	at %	wt %	element	at %	wt %	element	at %	wt %
B	26.8	21.2	B	34.6	29.1	B	32.3	26.2
Ce	0.4	3.6	Ce	0.1	1.3	Ce	0.4	3.9
O	5.4	6.3	O	2.7	3.3	O	5.7	6.9
C	64.9	57.1	C	60.7	56.8	C	59.7	53.8
Cu	2.5	11.8	Cu	1.9	9.4	Cu	2.0	9.3

A.2 XPS quantitation models

A.2.1 Flat layered model

The flat layered model used to calculate the oxide overlayer thickness of the planar boron samples, and used as a first approximation for the overlayer thickness on the boron nanoparticles, consists of the following. The samples were assumed to consist of a flat metallic boron substrate covered by a uniform layer of B_2O_3. The sample was represented by a series of thin layers, starting at an initial depth much greater than the escape depth of B 1s photoelectrons. B 1s photoelectrons are generated in each layer with intensities proportional to the atomic density of B in that layer. These electrons are added to electrons coming from the layer below, and passed to the layer above with the appropriate attenuation factor: $\exp(-L_{thick}/EAL)$, where L_{thick} is the layer thickness, and EAL is the effective attenuation length for B 1s photoelectrons in either B or B_2O_3, depending on the composition of that layer. boride and oxide layers are varied until the calculated and experimental ratios are in agreement. EAL values for the B 1s photoelectrons (KE = 1298 eV) in boron, and boron oxide were calculated using the NIST Electron Effective Attenuation Length database program and are 2.90, and 3.14 nm, respectively.[1] The process is repeated until the surface of the model sample is reached, at which point the ratio of electrons from B and B_2O_3 can be calculated. The assumed thickness of the oxide layer is varied until the calculated and experimental ratios are in agreement.

A.2.2 Random packed spheres model

For this model, the boron surfaces were represented as 50 nm diameter randomly packed spheres made up of a core of pure boron surrounded by thin, uniform shell of

B_2O_3. As before, a layered model was used with B 1s photoelectrons generated with intensities proportional to the atomic density of B in that layer. The detected intensity of photoelectrons is given by $I=I_0exp(-t/cos(\Theta)$ EAL), with Θ being the take off angle of the photoelectrons. The thickness of the oxide shell for the spheres is varied until a match is obtained between the model and the experimentally determined B^0/B^{3+} intensity ratio.

A.3 Reference

(1)   Powell, C. J.; Jablonski, A. *NIST Electron Effective Attenuation Length Database Version 1.1*Gaithersburg, MD, 2003.

APPENDIX B

ADDITIONAL DATA FOR CHAPTER 5

STEM/HAADF images with accompanying EDX data were also obtained for particles that had passed through the reactor at 700° C. Figure B.1 and Table B.1 show a typical cluster of particles. Direct comparison with Figure 5.7 and Table 5.3 in Chapter 5 shows that the composition of the particles is similar. As before, several different areas of the sample grid were looked at to avoid sample bias, with no appreciable differences noticed. Two images are shown in Figure B.1; the topmost shows the image with EDS data collected from the center of one of the particles, in the bottom one, EDS data were collected from the diffuse edge of one of the particles. Table B.1 summarizes the results.
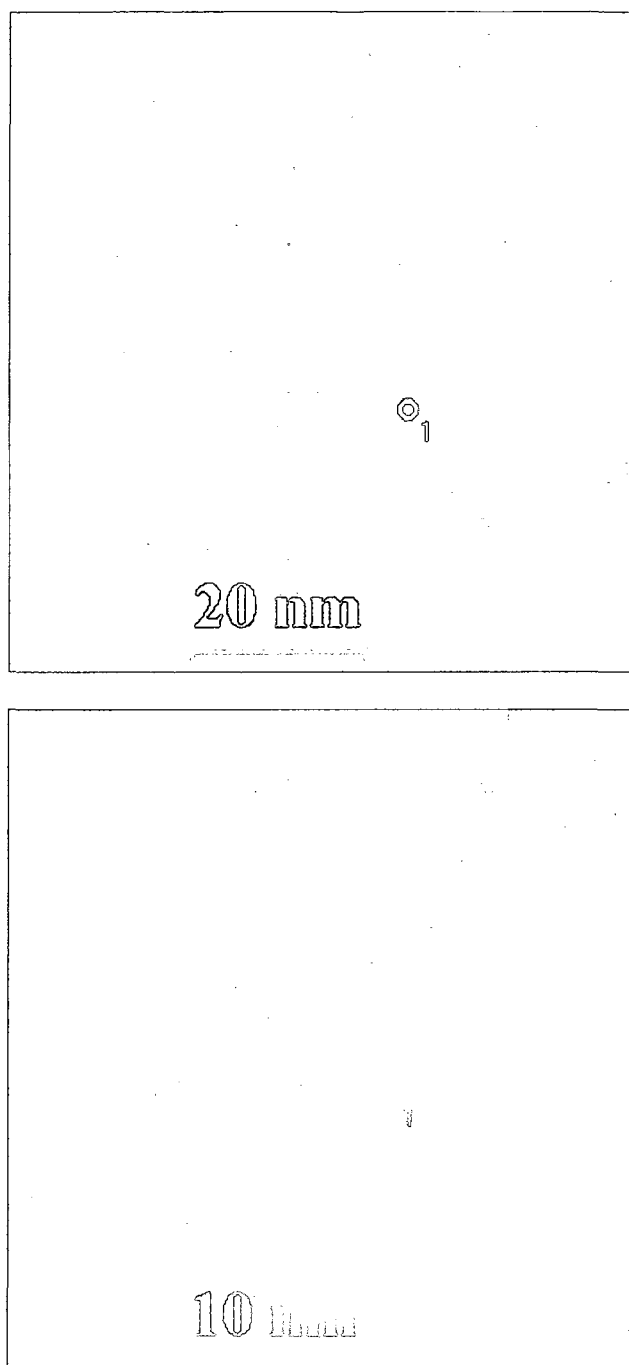
Figure B.1 STEM/HAADF images of (THD)$_2$ catalyst after passage through reactor at 700° C.

Table B.1 EDX results from Figure B.1.

XEDS atomic composition			
top image		bottom image	
element	atomic %	element	atomic %
Pd(K)	20.4	Pd(K)	17.5
O(K)	4.7	O(K)	-
C(K)	66.1	C(K)	77.9
Cu(K)	8.7	Cu(K)	4.5